An Integrated Polymer Based Polymerase Chain Reaction And Capillary Electrophoresis System For Genetic Diagnosis

by

Tianchi Ma

A thesis
presented to the University of Waterloo
in fulfillment of the
thesis requirement for the degree of
Master of Applied Science
in
Electrical and Computer Engineering

Waterloo, Ontario, Canada, 2014

I hereby declare that I am the sole author of this thesis. This is a true copy of the thesis, including any required final revisions, as accepted by my examiners.

I understand that my thesis may be made electronically available to the public.

Abstract

Micro-Total-Analysis-Systems (μTAS) for genetic diagnosis have a great potential to revolutionize the future of health care. However the lack of μTAS, which is fully integrated, mass-producible and application oriented, has delayed μTAS development in real life application. In this work, I developed designs, protocols and supporting infrastructures for a polymer-based, fully integrable genetic diagnosis system capable of the Polymerase Chain Reaction (PCR) and Capillary Electrophoresis (CE). Each individual module could be integrated through a novel valve/pumping design and is fully capable of hand-free operation.

These modules have been demonstrated to have a separation similar to our previous generation glass-based chips, which have previously proved the capability of genetic diagnosis. The integrated PCR module has demonstrated the concept of a CMOS compatible PCR system that is capable of mass-production. These discrete PCR modules are rapid prototypes. Using laser-based and milling machine-based rapid prototyping methods, the fabrication processes and module designs were developed. During this, the designs were studied through simulations and back-of-the-envelope (BOE) calculations. At the time of writing, the valving, PCR and CE modules have been successfully tested (with publications in print, in press and underway). In addition, a valving and CE combination has also been successfully demonstrated for a restriction fragment length polymorphism (RFLP) diagnostic and submitted for publication.

All of these designs were intended to be developed in a manner that could be implemented in a PMMA chip, or on a future CMOS chip for greater cost reduction. This work has developed some of the key technologies for PCR-CE in a way that is scalable to such a CMOS system, notably with valves that can be used in a hybrid PMMA/CMOS system, and in testing a silicon based and robust temperature control system that could be implemented on CMOS.

Acknowledgements

I want to thank my supervisor Dr. Christopher J. Backhouse for his support and guidance through my graduate study. Without his help and advice, I would not be able to complete my degree. Special thanks to Dr. D. Moira Glerum and Dr. Duncan G. Elliott for sharing their expertise in molecular biology and CMOS technology. Their comments are fruitful and valuable.

I would like to acknowledge my fellow students, who were involved in this project: Gordon Hall, Victor Shadbolt, Madeline Couse, Nemanja Kliska, Jose Martinez-Quijada and David Sloan. They have been great colleagues and collaborators during my graduate study. I want to specially thank Gordon, Victor and Madeline for their support through the project and being such nice friends.

I also want to acknowledge the financial support of Teledyne DALSA Semiconductor, the Natural Sciences and Engineering Research Council of Canada and the University of Waterloo.

Dedication

To my great parents and my wife.

Table of Contents

List of Tables xi

List of Figures xiii

Abbreviations xxi

1 Introduction 1

1.1 Objective . . . 2

1.2 Thesis overview . . . 3

2 Laser Fabricated Polymer Chip For Capillary Electrophoresis 5

2.1 Background . . . 6

2.2 Introduction . . . 6

2.3 Basics of Capillary Electrophoresis . . . 8

2.3.1 Principle . . . 8

2.3.2 Resolution . . . 9

2.4 PMMA . . . 11

2.5 Laser Fabrication, Characterization and Development . . . 12

2.5.1 Laser System . . . 12

2.5.2 Chip Design For Laser Machining . . . 13

2.5.3 Laser Engraving Protocol . . . 16

2.5.4 Channel Characterization: The Cracking Technique 18
2.6 PMMA Bonding And Development 19
2.6.1 130 °C Surface Treatment And Annealing 20
2.6.2 Solvent Bonding 21
2.7 Capillary Electrophoresis Characterization 21
2.7.1 Capillary Electrophoresis: Hydroxypropyl cellulose (HPC) 22
2.7.2 Agarose Capillary Electrophoresis: Old Material With A New Application 26
2.8 Discussion 29
2.8.1 Resolutions 29
2.8.2 Surface Roughness Vs. Resolution 29
2.9 Summary 33

3 Integration For Hands-Free Operation **34**
3.1 Introduction 35
3.2 Laser Rapid Prototyping Valve Module 36
3.2.1 Novel Mono-layer Valve Design 36
3.2.2 Standard Manifold Footprint 37
3.2.3 Valve Deflection 37
3.2.4 Materials And Fabrication 39
3.2.5 Results 39
3.3 SP-CE Integration For Auto-RFLP 41
3.4 Summary 44

4 CMOS Compatible Thermal PCR Module **45**
4.1 Introduction 46
4.2 Why CMOS? 47
4.3 PCR-CE Integrated CMOS Plan: A Helper Chip System 47

4.4 CMOS PCR Module Design . . . 47
4.5 Thermal Robustness . . . 51
4.6 Initial Specification Of The Si Heater . . . 52
4.7 Methods And Material . . . 54
4.7.1 Determination Of Chamber Temperature From TCR . . . 54
4.7.2 TCR Measurements . . . 55
4.7.3 Heater Control . . . 56
4.7.4 Determination of Temperature From Temperature-dependent Fluorescence . . . 56
4.7.5 Optical Determination Of Chamber Temperature . . . 58
4.8 Results . . . 59
4.8.1 Heater TCR Verification . . . 59
4.8.2 Si Heater Specification Verification . . . 59
4.8.3 Optical And Electrical Temperature Measurements . . . 64
4.8.4 Determination Of Temperature Uniformity From Optical Temperature Measurement . . . 66
4.8.5 Limitation Of The Current Taped Chamber Si Heater Chip . . . 66
4.9 Conclusion . . . 69

5 PCR-CE Platform With Discrete PCR Heater Module Plan: Tape Based Thin Chips 72

5.1 Introduction . . . 73
5.2 Discrete Heater System Design . . . 74
5.2.1 Materials And Equipments . . . 74
5.2.2 Discrete Heater System: Cross-section And Top-view . . . 75
5.2.3 Basic Design Requirements . . . 79
5.2.4 An Analytic Model . . . 79
5.2.5 Time Constant . . . 84
5.2.6 Boundary Conditions . . . 85

5.2.7 Maximum Chamber Depth . . . 86
5.3 Requested 3D Simulation For Discrete Heater System . . . 87
5.3.1 Boundary Conditions And Assumptions . . . 87
5.4 Experiments . . . 89
5.5 Results . . . 89
5.5.1 Time-domain 3D Simulation . . . 89
5.5.2 Preliminary Heater System Test Result . . . 94
5.6 Summary . . . 96

6 PCR-CE Platform With Discrete PCR Heater Module Plan: PMMA Based 1.5 mm Chips 97

6.1 Introduction . . . 98
6.2 PMMA Based Chip Design . . . 98
6.3 1D Resistive Model For PMMA Based Chip . . . 99
6.3.1 Vertical Heat Flow For Chamber . . . 100
6.3.2 Vertical Heat Flow For Manifold . . . 103
6.3.3 Vertical Heat Flow For Insulation Region . . . 103
6.4 Simple 2D Model . . . 104
6.5 Requested 3D Time-domain Simulation . . . 107
6.5.1 Boundary Conditions And Assumptions . . . 107
6.5.2 Requested Measurements . . . 108
6.6 Experimental Results . . . 109
6.7 Future Chip Designs . . . 112
6.7.1 PCR-RFLP Chip . . . 112
6.8 Conclusion . . . 112

7 Conclusion And Future Directions 114

7.1 Conclusion And Future Directions . . . 115

APPENDICES **116**

A The Si Heater **117**

A.1 Amscope Camera Setting For Image Acquisition 118

A.2 Sample Python Script 118

A.2.1 Heater Control Program 118

References **127**

List of Tables

2.1 Laser driver settings for laser ablation. 17

2.2 Resolution and separation range vs. channel roughness. The channel roughness is defined as the bump height at the bottom of the channel. Resolutions for all chips are calculated for the 200-300 bp region. The separation range is determined by the maximum DNA species length that could be resolved. 31

3.1 Polypropylene materials properties 38

3.2 Laser ablation setting for microfluidic chips with integrated valves. The low power multiple passes cutting parameter is the key for generating small vias through 1.5 mm PMMA sheet. These cutting parameters have been optimized for best valving performance and reproducibility. 39

4.1 Thermal resistances for a 1550 μm heater operating at 95 °C. 52

4.2 Summary of different Si heater batches. The number of chips is only for the U1550 type chips, since other heater design were not used for this project. Batch #2 was shipped to us in two shipments. The first three batches were not useable due to malfunctioning microfluidics and delamination. The 4th batch was the only good batch, but it still has the moisture problem of the 2nd batch and did not meet the sizing requirements. 61

5.1 List of all the layers in Fig. 5.2b 78

5.2 List of temperatures and thermal resistances labeled in Fig. 5.3a, and the corresponding layers in Fig. 5.3b. 82

5.3 Thermal conductivity and resistivity for a 5 mm diameter chamber 83

5.4 List of the thermal time constants 85

6.1 Design dimensions for PMMA based Heater System 98
6.2 Thermal conductivity and resistivity for a 5 mm diameter chamber in vertical direction 101
6.3 Modified PCR thermal cycling program for on chip PCR. The program was modified from the original protocol (shown in brackets) used for HFE exon 2.110

List of Figures

2.1 Demonstration of microchip CE: a) Annotated drawing of the CE chip: Channels are filled with sieving matrix; Sample well is loaded with DNA sample, while the rest of wells are loaded with CE running buffer. b) Injection step: DNA strands are moved towards the positively-charged electrode, c) Separation step: After injection, the electric field is applied across the separation channel. DNA samples in the intersection (a sample plug) are pulled towards the buffer waste well. Then the plug is separated into discrete bands of DNA, based on their length. 9

2.2 A sample electropherogram generated from HV1 CE using HPC as sieving matrix. The CE conditions are the same as described in Section 2.7.1. A electric field of 280 V/cm is applied across the separation channel. 10

2.3 Composite design of 3 small electrophoretic separation chips, each containing two intersecting channels that link 4 wells of approximately 6 μL in volume. The chips are held in a larger assembly 10 cm x 2.7 cm in size, and contain 2 alignment holes. The left plate is the channel plate which contains the channel and wells. The well at the top left of each is the buffer waste (BW), that on the top right is the sample well (S), that on the bottom left is the sample waste (SW) and that on the bottom right is the buffer (B) well. . . 14

2.4 Chip design for laser ablated PMMA chips. The double layer channels and double -T intersection are formed by overlay A, B, C and D channels shown around the chip. The four channels were created in the order from A to D. 14

2.5 Images of the intersections with and without a narrow region: a) Intersection ablated by the original design file; b) Intersection ablated by the modified design file. There is no narrower region along the separation channel (the horizontal channel). The images were taken at different zoom factors. Both channels had similar channel width. (Note: All the images were taken with the stereo microscope used in Section 2.5.4.) 15

2.6 Images of the well-channel interfaces generated using two different approaches: a) The channel was ablated before the well; b) The channel was ablated after the well. If the channel is ablated before the well, the heat generated by the well cut can cause reflow of the PMMA around the well and lead to closed channels. 16

2.7 Images of the debris generated by different laser ablation settings: a) Debris along the well cutting line; b) Debris along the ablated channel. The well-cut lines generated much more debris along the path than the channel ablation. In order to minimize the amount of debris on the channel surface, the channel is ablated on the other side. 17

2.8 Design of the PMMA coupon for the cracking test. The bottom right section will be cracked off in order to show the side view of the blue ablation line. In order to show the effect of the CE channel, the same channel engraving parameters are used for the blue line. 18

2.9 Cross-section of CE chip channel: from the images, the width of the channel is 106±5 μm, and the depth is 144±24 μm. The large uncertainty of the depth is caused by the bumps at the channel bottom. In order to show the bottom smoothness, the channel was ablated as per fabrication protocol, except the laser beam was set to be in focus. 19

2.10 HPC CE electropherogram at 280 V/cm at 11 mm using β2M and HV1 products: a resolution of 20.9 bp was demonstrated. This resolution is the same as the resolution with the glass chip at similar separation distance, and is sufficient for sizing common diagnostic PCR products. 24

2.11 Electropherograms of HPC CE with B2M PCR products. From bottom up, the 5 groups of electropherograms were CE results of chips fabricated on 2012-08-13, 2012-08-20, 2012-08-28, 2012-09-04 and 2012-09-26. Each group consists of the 3rd, 4th and 5th injection of the 1st load for each chip. In order to generate the plot, the 1st peak of each electropherogram was aligned to the 20 s mark. Then, in each group a half second offset was introduced for each run in order to show clear peaks. The 2nd group from the top had a resolution 3 times worse than others, and it is likely caused by a 5-day delay prior to bonding due to unexpected oven failure. 25

2.12 CE separation in 2 % agarose using β2M product on a laser ablated CE PMMA chip: the product and the primer are well separated. An electric field of 100 V/cm was applied for both injection and separation. The detection point was set at 11 mm. Comparing to HPC-β2M separation, the $\frac{FWHM}{(t2-t1)}$ for agarose and HPC are 0.188 and 0.042 respectively. Thus, the CE resolution of 2% agarose is about 3 times worse than HPC and estimated to be 90 bp. This experiment was performed by Victoria Northup. The CE chip was fabricated by Tianchi following the initial protocol by Dr. Backhouse. . . . 27

2.13 0.65% agarose CE using the 100 bp ladder with a separation field of 25 V/cm at 11 mm after the intersection. The size standard was a 100 bp ladder with DNA fragment lengths of 100, 200, 300, 400, 500, 517, 600, 700, 800, 900, 1000, 1200 and 1517 bp. The resolution was about 50 bp in the 200-300 bp range. All 12 expected peaks are apparent, with the 500 bp and 517 bp bands run together. This experiment was performed by Victoria Northup. The chip was fabricated by Tianchi following the initial protocol provided by Dr. Backhouse. 28

2.14 Channel roughness vs chip performance: a) Collage showing depths of each channel, the channel roughness increases from the top to bottom; number of peaks resolved using 100 bp ladder for each chip is: 12, 5, 4, 3 and 2 respectively; b) Representative electropherograms for the 1st, 3rd and 5th chips. 30

2.15 Channel roughness vs laser focus: a) Laser beam focused on the top of the PMMA surface and the bump depth is 24.5 $\pm$3 μm. The channel is 106$\pm$5 μm wide and 144$\pm$25 μm wide. b) Laser beam was out of focus by 800 μm into the substrate, and the bump depth was 12.5 $\pm$3 μm. The channel is 128$\pm$5 μm wide and 120$\pm$12 μm deep. By defocusing the laser, the channel roughness was reduced by near 50 %. 31

2.16 Plot of channel characterization vs. laser focus: a) Plot of channel depth (blue diamond), channel width (red square) and bump height (green triangle) vs. laser focus. b) Plot of the bump height to channel depth ratio vs. laser focus: Laser beam focus was adjusted from 2.4 mm to -0.8 mm relative to the substrate surface in 0.2 mm increments while a test chip was ablated at each setting. The bump height to channel depth ratio is plotted as a function of the focus distance (z-axis). From the plot, the ratio decreases as the laser focal point moves into the substrates. The ratio is relatively constant when laser focal point moves in the other direction. 32

3.1 A schematic for the vertical membrane valve: Laser engraved trenches and applied tape form the channels at the bottom. Two channels are connected through laser drilled vias when the membrane is pulled up by vacuum. The valve is closed when positive air pressure is applied. 37

3.2 Choreography for the auto-RFLP process: the implementation of pumping realizes the complete hand-free operation of RFLP. a) A sample chip is first stored with buffer in the buffer waste (BW), sample waste (SW), buffer (B) and sample (S) wells. b) The S well buffer is then replaced with sample. The system automatically pumps water c) and buffer d) in to the sample well through peristaltic action using three valves. After mixing an inject-separate is done. e) The enzyme is mixed with the sample. After 10 minutes of digestion a second run is done. 42

3.3 Demonstration of auto-RFLP on a commercial confocal system: The bottom is the electropherogram of the undigested PCR product; The top is the product after 10 minutes on-chip enzyme digestion at room temperature. An injection field of 43 V/cm and a separation field of 40 V/cm were applied. The detection point was 11 mm away from the intersection. After one inject and separation, the enzyme was pumped to the sample well and waited for 10 minutes at room temperature before the next injection and separation. It is clear to conclude that the micro valves and pumps have successfully mixed the enzyme with the sample. 43

4.1 A schematic diagram of the intelligent packaging showing functions of: valving, thermal control and interface. Valving is done by deforming a membrane through external pneumatic control modules. The thermal circuit is connected through pogo-pins on exposed Al pad. The HV module is connected by inserting Ni electrodes into the open reservoirs, which is connected to the CE parts of the University of Alberta (UofA) chip. The Cu plate at the bottom is a heat-sink for rapid cooling of the chamber. 48

4.2 A zoom in cross-section view of the PMMA-Si helper chip design above the heater chip region. (The drawing is not to scale.) 49

4.3 Drawing for the UofA Si heater chip: A. Cross-section drawing for the heater stack of CMOS heater atop the Si substrate; B. Top-view drawing of the proposed CMOS stack heater design showing the PCR chamber (center well). The wells, channels and vias are parts of the fluidic system that is intended to fill the chamber and to perform capillary electrophoresis. The fluidic parts are the same ones covered in Chapter 3 50

4.4 A thermally resistive divider presentation of the stack heater: the heater flow is dominant in the vertical direction 53

4.5 Rhodamine-B (RhB) calibration curve: relative fluorescence vs temperature. By fitting a third order polynomial, the characteristic equation was found to be $T = 132 - 250I + 220I^2 - 79I^3$. This calibration was performed by Gordon Hall in October 2012. 57

4.6 Amscope Camera Image of the Si heater chip during the chip inspection. The channel, via and wells are clearly shown in the picture. The light colored area has Al layer under the KMPR. In order to take this image, a 2X magnification lens was attached. 62

4.7 SEM images of the UofA heater chip: a) the channel is open; b) The top KMPR layer collapsed and bonded in front of the channel; c)The edge of the via collapsed and bonded to the channel bottom layer. From the University of Waterloo (UofW) testing, the statistics shows a rough 60 % failure rate for each channel. Thus, due to the limited number of the available chips, it was not feasible to continue with the helper chip approach unless this problem is fixed by the UofA. The SEM image was provided by Matthew Reynolds on 18 June 2013. 63

4.8 Heater temperature measurement at constant input power. For t < 80 s, the control program increased the input current in steps to reach 250 mA. While for 80 s<t<280 s, the heater input current was held at 250 mA as programed. The slope of the lines in the latter period is attributed to the heat sink warming up by an estimated 3 °C. The divergence between the two traces for t<25 s is due to the electrical noise introduced by the current source at low current region and that for t>280 s is due to the difference of the cooling rates. Optical (green line) and electrical (blue line) temperatures compared as heat sink warms up showing that even as external parameter change (primarily the heat sink temperature), the two temperatures tracked each other within 0.3 °C. 65

4.9 Optical demonstration of the chamber temperature uniformity: a) A fluorescence image of the chamber at room temperature to show the nonuniform illumination profile; b) A fluorescence image of the chamber at 43 °C; c) The result of subtracting the 43 °C chamber fluorescence from the scaled room temperature with markup of the central undistorted region. d) Counts vs distance (μm) from the chamber top edge plot for the room temperature (blue +) and the 43 °C (red ×) chamber images. Both sets of data follow the same general behavior due to the illumination. The shaded regions indicate excluded data where signal distortion occurred due to the low signal intensity. 67

4.10 Image of bubble expanding: a) fluorescent image at room temperature; b) Image of the chamber at 350 mA input current (or 55 °C equivalent). At higher current, the air bubble area was significant in the chamber. This caused the chamber to deform outward in order to compensate for volume increase, which in turn increased the optical depth. 69

4.11 Measured chamber temperature vs time plot with the input current steps up to 350 mA: TCR measurement agrees with optical measurement at low input current; As chamber temperature increases with the input, the agreement was interrupted. By tracing the collected images, which have time stamps, the interruption occurred during the formation of air bubbles. After 350 s, significant air bubble formation appeared as shown in the right half of Fig. 4.10. 70

4.12 Heater failure after heating under water: a) Image of a chip after optical temperature detection. From the image, corrosion appeared on most traces. b) Image of a Si heater chip from the same fabrication batch before water test. c) Image of chip shown in b) after water bath heating. The chip was immersed in water and heated at 95 °C for 30 minutes. There is a significant amount of delamination and corrosion-like damage to the Al trace. Both chips were selected from the batch #2. The stereo microscope with the Amscope camera was used to take the images. Similar results were observed at the UofA with on chips selected from the batch # 4 under similar conditions. 71

5.1 A top-down view of the discrete heater system is presented. A PMMA manifold is directly atop the membrane. The heater layer and the insulation layers are laminated to a 0.25 inch Cu plate. The chip layer is sandwiched between the membrane and the heater. As stated in Section 5.2, a rectangular heater is used due to availability. Two slice points are labeled which indicate the direction of the cross-section views which are shown in Fig. 5.2a and 5.2b. 76

5.2 Cross-section views of the discrete heater system: a)Longitudinal cross section: a drawn to scale view along the slice point A; b)Lateral cross section: A zoomed-in view of the dotted section along slice point B with detailed labeling. The lateral view is not to scale in order to provide more details on the microfluidic region. 77

5.3 Resistive divider network of the thin chip and the Omega Heater system: a) Circuit representation of the heater analytic model; b) Heater cross-section with thermal resistance labeled. 81

5.4 Cross-section view of the heater system with boundary conditions labeled. 88

5.5 Cross-section view of the heater system with modified boundary conditions. 90

5.6 Plot of temperature variation of the system versus time. The blue line shows the maximum temperature difference within the PCR chamber. The green line is the result of the average chamber temperature minus the average heater temperature. 92

5.7 Radial temperature distribution of the top heater surface. The blue line is the original design which showed a significant temperature change across the heater surface. The green line (flat line) is the distribution of the modified design. 93

5.8 Mockup PCR by using one tape-sealed PCR chamber on 2 different days: Solid line is TCR determination of temperature; dashed line is temperature from RhB fluorescence. Significant run-to-run variation and difference between TCR and RhB value have been observed. 95

6.1 PMMA chip cross section: the dimensions are as labeled. The cross-section is perpendicular to the long side and only half is shown due to symmetry. . 99

6.2 LTspice simulation of vertical heat flow for section A. This demonstrates that the chamber takes 40 s to reach the linear region (or steady state). In addition, the steady state temperature for each step is within ±1 °C of the target temperature as indicated by the light colored bands. 102

6.3 Simple 2D LTspice model 105

6.4 Further simplified 2D LTspice schematic 106

6.5 The requested boundary conditions of the 3D simulation. 108

6.6 Electropherogram of the PCR products in agarose CE chips (Maddie Couse). The CE condition used was the same as the 2 % agarose CE described in Chapter 2. The blue line is the CE results of the conventional PCR; the red line is the 2nd test on milled chip; the green line is the PCR product from a laser fabricated chip. All three products showed successful PCR amplification. For the red line, all peaks shifted to the left comparing to the conventional product. This could be caused by changes in the buffer concentration due to the recovery process. However, the distance between the product and primer peak is the same as the blue line. The 2nd peak on the red line is the primer dimer which likely indicated the chamber temperature was slightly less than 65 °C.The green is comparable although this analysis was complicated by apparent fracture in the loaded agarose and interrupted PCR. 111

6.7 Top down of the PCR-RFLP chip 112

Abbreviations

μTAS Micro-total-analysis system

BOE back-of-the-envelope

CE capillary electrophoresis

EOF electro-osmotic flow

HFE hereditary haemochromatosis

HPC hydroxypropyl cellulose

LOC lab-on-chip

PMMA Poly(methyl methacrylate)

POC point-of-care

qPCR quantitative polymerase chain reaction

RFLP restriction fragment length polymorphism

RhB Rhodamine-B

SOP standard operating procedure

TCR temperature coefficient of electrical resistance

UofA University of Alberta

UofW University of Waterloo

Chapter 1

Introduction

Micro-total-analysis systems (μTASs) have tremendous potential to revolutionize the future of health care. [1] If several or all related bio-chemical processes can be integrated into one compact portable system, there will be no need to build centralized clinical labs. By decentralizing the analyzing process, the process time per sample will be significantly reduced as well as the cost associated such as sample transportation, manpower and storage. Computer controlled automatic process will also free the highly trained technicians from the routine tasks. However, the lack of a μTAS, which is cost-effective, fully integrated, automatic and providing sample-to-result solution, is still preventing these technologies from real world application. [2] This makes the current μTAS uncompetitive compared to current solutions. In this thesis, the work presented is one attempt to reduce the gap by developing low-cost polymer based modular μTAS. Each module performs one task of the diagnosis process and integrated through on-chip valve/pumping. In addition, the designs of the system have the potential to be scaled down and mass-producible for even lower cost. In future, all of these modules can be implemented on a CMOS platform for greater integration and cost reduction.

1.1 Objective

Micro-total-analysis system (μTAS), sometimes called lab-on-chip (LOC), as indicated by its name, is the miniaturization of processes in an integrated device, starting with a raw sample and performing a series of manipulations that produce a final result from which a decision can be made. [3] μTAS has great potential to revolutionize personal healthcare by providing fast, automated, portable and inexpensive diagnosis solutions for clinical applications such as point-of-care (POC). [1] In a review by Chin et al. [2], the global impact of μTAS is presented with potential applications, especially for developing countries. However, the development towards a true μTAS remains elusive, even after 25 years.

Since the first introduction of the concept by Manz et al. [4] in 1990s, researchers have invested tremendous effort into the realization of μTAS and fascinating systems have been demonstrated as shown in various reviews. [2, 5, 6] In the most recent reviews by Kovarik et al. [6] and Nge et al. [7], they concluded that the lack of μTAS developments is due to an absence of a fully integrated mass-manufactured solution.

My research is intended to close the gap by developing a μTAS rapid prototyping platform that is cost effective, modular but fully integrable, and capable of mass production. In order to achieve this, I narrowed down my interest and focused on genetic diagnostics. μTAS, based on the bio-marker utilized for detection, is classified into two streams: protein analysis and DNA analysis. As reviewed by Njoroge et al. [8] and Foudeh et al. [9], DNA based detections have the advantages of higher sensitivity and specificity than protein based processes, and are capable of rapid diagnosis. The rapid diagnosis capability is critically important for infectious pathogen detection.

In terms of material, polymer based microfluidic chips have gained most attention since they are relatively inexpensive and amenable to mass production. [7] Hot embossing and mold-injection are techniques readily available for small scale and large scale fabrication. These give polymer based capillary electrophoresis (CE) chips great potential over conventional glass based LOC technology. However, both hot embossing and mold-injection, have a relatively long turnaround time for new designs in small scale fabrication since each design requires a custom made mold. Laser ablation is then selected for small scale fabrication as its capability of rapid prototyping. For system functions, Lee and Hsing [5] have a detailed review on DNA based μTAS and classified three main functions for such a system: sample preparation, DNA amplification and target detection. Sample preparation involves the processes that extract and purify the DNA from raw samples such as blood. Then the DNA sample is amplified to a higher concentration through the PCR process. After amplification, the product is checked for the presence of target DNA at the final

step, which provides the decision making information. In this work, I started my research from detection to amplification with automatic integration in-mind, and since the sample preparation is direct implementation of the clinical protocols onto micro systems, it is more related to fluid handling and system integration. As a result, the integration related work would greatly benefit the future development of sample preparation.

There are many different detection methods such as quantitative polymerase chain reaction (qPCR), CE and various DNA sequencing technologies. qPCR based systems are among the most popular for compactness and ease of realization, as the amplification is also the detection process. For details, please refer to reviews by Ahmad and Hashsham [10] and Almassian et al. [11]. However, as Bustin et al. [12] concluded from their review, PCR based detection results alone are not sufficient for decision making. Further validation of the amplicons is needed via methods such as CE and sequencing. For sequencing, the cost and waiting-time per sample have reduced dramatically, due to the development of the so-called next generation sequencing technology. But as mentioned by Katsanis and Katsanis [13] in a Nature review, CE and PCR based technologies still remain the most cost effective.

As a result of all these considerations, this thesis is focused upon the development of an integrated PCR-CE system for genetic diagnosis. Each of the two individual modules (PCR and CE) could be integrated through a novel valve/pumping module for hands-free operation. In the following chapters, I will present my contribution to the development of each module (detection, integration and amplification) and the important results.

1.2 Thesis overview

In chapter 2, I present the development towards producing a polymer based CE chip using laser ablation and solvent-assist bonding. Starting with the initial fabrication protocol developed by Dr. Chris Backhouse, based on the literature, I modified the protocol in order to achieve a more uniform surface and smooth channels. By using this protocol, the chips achieved 20 bp resolution which is comparable to the glass chip developed in our lab previously. In addition, my polymer CE chips were used in the exploration of utilizing the solid phase sieving matrix, agarose, for on-chip CE. Through the development, my colleagues found the CE resolution was erratic, especially for the higher base pair DNA strands. By using my cracking technique for examining the channel laterally, we found that the CE resolutions for the higher base pair DNA strands were better in the channels with a smooth bottom. This new finding was published in Proceedings of SPIE 2012. [14]

Chapter 3 presents my solution for solving the integration problem for a low cost PCR-CE system. A novel valve design is presented for fluid handling: valving and pumping. The novelty of the valve is its ease of reconfiguration and fast design-test cycle. By utilizing this valve, I designed an integrated restriction fragment length polymorphism (RFLP) CE chip that is capable of hands-free operation. By using the chip, my colleagues and I demonstrated an RFLP analysis of the C282Y mutation in the hereditary haemochromatosis (HFE) gene. This work has been presented at IEEE Nano 2014.

In chapter 4, I present my contribution to a collaborative project for a CMOS-based PCR heater module. I designed the polymer-CMOS helper chip packaging technique for testing CMOS-based silicon heater system. I have demonstrated the use of the heating element as a temperature sensor during the heating process. This proves the concept of a CMOS-compatible heater system that does not require device level calibration. This is the key for future mass-production of low cost μTAS and implementation on a CMOS platform. This work is about to be submitted to the Journal of Micromechanics and Microengineering.

Chapter 5 and 6 present the development of PCR heater modules using commercially available heaters with two different chip designs: thin tape chip and 1.5 mm Poly(methyl methacrylate) (PMMA) chip. I performed a preliminary back-of-the-envelope (BOE) calculation for each of the heater designs. In addition, I have performed preliminary experimental tests on the infrastructure and the thin tape chip system. Combined with the numerical simulation done by my colleague, we decide to focus on the 1.5 mm PMMA chip design. At the end of Chapter 6, a potential design of a fully integrated PCR-CE system is presented.

Chapter 7 presents the conclusions and possible future directions for this project.

Chapter 2

Laser Fabricated Polymer Chip For Capillary Electrophoresis

In this chapter, a fabrication protocol of a laser ablated PMMA-based chip was developed. The CE chips fabricated by this protocol have been shown to be similarly capable of diagnosis as the glass chips previously demonstrated by Dr. Backhouse's Group [15]. Building upon our previous knowledge of glass-based CE chips, our group transferred to polymer-based chips for ease of fabrication, low cost and speed of the design-build cycle. However, as suggested by Jensen et al. [16] and Pfleging et al. [17], different grades and manufactures of the PMMA substrates would have significantly different results after processing. Thus, a reliable fabrication protocol that is customized for our lab is essential for future development. Based on available literature findings and an initial fabrication protocol by Dr. Backhouse, I developed an improved fabrication protocol and a unique characterization technique for the PMMA CE chips.

The PMMA CE chip performance was tested by running CE, using hydroxypropyl cellulose (HPC) as the sieving matrix. The PMMA-based CE chip demonstrated a 20 bp resolution, equivalent to our glass CE chip with similar dimensions. In addition, the PMMA CE chips were used in the demonstration of agarose as a solid-phase alternative to liquid-based sieving matrices for on-chip CE. My colleague found the CE performance was erratic from chip to chip. By using my 'cracking' technique as defined in Section 2.5.4, I could inspect the channel profile both horizontally (as in almost all other literature) and laterally. Thus, by characterizing the CE chips after the agarose CE experiments, I found that the better resolutions were demonstrated on chips with smooth channels, especially for longer DNA strands, which suggested that the CE resolution is correlated to the channel smoothness. [14]

2.1 Background

Capillary electrophoresis (CE) is a very powerful tool for clinical genetic diagnostics which has been demonstrated for various applications as reviewed by Dorfman [18]. The commercially available systems such as ABI 3130 Genetic Analyzer have long been on the market and used by clinicians and researchers. By having long capillaries (50 cm or more), these systems have demonstrated resolution down to the 1 bp level. With advanced and complicated mechanical valving and pumping accessories, some systems are fully automatic except for loading of the sample. However, this advancement of the commercial system comes at the expense of system size and extremely high cost per unit. By combining the development of Lab-on-a-chip (LOC) technology, short capillaries/channels etched in Si and glass have been demonstrated for CE by adapting micro-fabrication technology from the semiconductor industry. As laser-induced fluorescence (LIF) is the gold standard for DNA detection, the glass based chips are more popular than Si-based chips. Successful DNA separations on glass chips have been demonstrated in many applications as reviewed in Lewis et al. [19] and Ou et al. [20]. In terms of commercial systems, there are a few table-top automatic CE systems such as the Bio-Rad Experion and the Agilent Bioanalyser that are readily available. In our lab, we have demonstrated CE separation down to 2 mm channels in our previous publications. [15] However, the non-recurring engineering (NRE) cost, along with new chip design, and the slow cycle of micro-fabrication in academic labs, were preventing us from rapidly implementing new designs and led to having limited numbers of chips for testing. Thus, there is great need for a new approach, which allows rapid prototyping and is cost effective for different scales of fabrication. The polymer based chips are the most popular alternative due to their low cost, ease of fabrication and similar optical properties. However, the chip performance is highly dependent on the substrates as suggested by the literature. [16, 17] Therefore, a reliable fabrication protocol is needed for further development.

2.2 Introduction

CO_2 laser engraving is the most popular rapid prototyping method for polymer-based CE chips. Compared to other techniques (e.g., hot embossing and inject molding), laser engraving requires no mask or mold, which enhances an extreme short turn-around time for new prototypes and the low product volume is not an issue for an academic setting, which in fact prefers low volume. CNC micro-milling is another popular alternative to the use of the laser. However, milled channels are generally limited to a channel width of

200 μm or above due to the physical size of the mill bits. The fragile nature of the bit requires slow mill speed and a shallow cut per pass. In general, it takes an hour or more to fabricate a chip and constant machining, where a computer-controlled laser engraving machine could finish in seconds. Therefore, CO_2 laser engraving is the best approach for rapid prototyping of polymer chips, with dimensions similar to glass chips, in which the channel width is usually about 100 μm.

The work of Klank et al. [21] effectively introduced the use of CO_2 laser systems for the rapid prototyping of microfluidic systems. Since that time, these laser systems have been applied to a wide variety of applications, particularly with PMMA. Considerable early development was done on PMMA-based electrophoretic devices for DNA analysis, notably by Dubrow [22]. For CO_2 laser fabricated devices, demonstrations have ranged from PCR systems [23] to cell culture. Zhang and Xing [24] had published a good review on these devices. However, in term of laser-built microfluidics for DNA analysis, there has been surprisingly little development. The work of Sun et al. [25] is one of the few exceptions.

In the literature, it has been suggested that the ablation process leaves a surface with a surface charge that is less uniform than that of the pristine surface [26], leading to variations in the zeta potential and the electro-osmotic flow (EOF). This variation could strongly and reproducibly affect the resolution of the system, which determines how well the system can detect genetic variants. It is likely that this is a major barrier to the effective use of CO_2-laser-built microfluidics for DNA analysis applications. Thus, a 130 °C surface treatment is introduced to the bonding process, as suggested by the work of Cheng et al. [27] and Sun et al. [25].

In this chapter, I describe my development for a reliable laser protocol for polymer chip fabrication by a commercial laser engraving system from Universal Laser System Inc. Significant effort was spend on refining the laser fabrication parameter to achieve glass chip-like channels. A PMMA compatible sieving matrix, HPC, was used to replace POP-7, which is typically used in glass chips. Four out of five different batches of chips, which were tested under the same conditions, demonstrated similar chip performance. The other batch had resolutions three times worse, but this batch had experienced a long delay during the bonding process. In addition, the PMMA CE chips were used by my colleagues to explore the use of a solid-phase sieving matrix, agarose. From the CE electropherograms, a CE resolution about 20 bp was demonstrated for both matrices with PCR products less than 400 bp in length, which is similar performance to our glass CE chips. For kilobasepair DNA fragments, a 50 bp resolution was achieved at lower agarose concentrations. Furthermore, by using my lateral characterization technique, I found the correlation between the surface roughness of the channel bottom and the resolution of long base-pair DNA stand. My cracking technique is the key to identifying this correlation and has been published in the

SPIE Photonic North 2012 proceedings. [14]

2.3 Basics of Capillary Electrophoresis

2.3.1 Principle

CE is a separation technique utilizing the electrical force experienced by charged particles in aqueous solution. By applying a uniform electric field across the capillary, the electrical force experienced by the charged particles moves them towards oppositely charged electrodes. The moving speeds of the particles are different based on the particles' size, charge and shape. In order to enhance the differences, the aqueous solutions are, in general, high viscosity polymer solutions, referred to as sieving matrices. The concentration of the polymer chains, functional groups on the chain and the average length determine pore sizes, which are correlated to the moving speed of DNA fragments through the matrix. Thus, the DNA molecules of different sizes are separated into different bands, which could be imaged with fluorescence-based detection methods. A fluorescence detector is placed downstream in the capillary and records the level of fluorescent signal. An electropherogram is then plotted with fluorescence versus time. We can determine the size of each DNA band by comparing its arrival time at the detector to those of known size samples, often referred to as DNA ladders.

For microchip CE, the long capillary is replaced by micro-channels on the chip. A cross chip design is used to form a well-defined band in the channel for detection. Fig. 2.1 is a demonstration of the CE inject and separate process. After loading the chip, an electric field is applied across the injection channel with the sample waste well being positive. Negatively charged DNA molecules are thus pulled into the injection channel. Even though the sieving effect happens during the injection step, the continuous injection of the DNA samples of different sizes from the sample well does not allow (complete) separation. The result is a stream of DNA with short chain molecules dominating at the front, while the rest is a mixture of long and short DNA molecules. After the front of the stream passes the intersection, we switch to the separation step, in which the electrical field is applied across the separation channel. The DNA molecules in the intersection are pulled towards the buffer waste well. Since the intersection is well defined, and with no additional supply from the sample well, the mixture of DNA is separated into discrete bands according to size. The fluorescent labels on the DNA molecules are then detected by a photo detector at a known distance from the intersection. The fluorescent signal is plotted vs. time in an electropherogram as shown in Fig. 2.2. The shorter DNA fragments

(primers and primer-dimers) move faster and appear early in the graph, while the longer fragments (DNA products) arrive later on the sensor and appear by the end (the 3rd peak). By analyzing the locations of the peaks on the plot, we can determine the genotype of the sample.

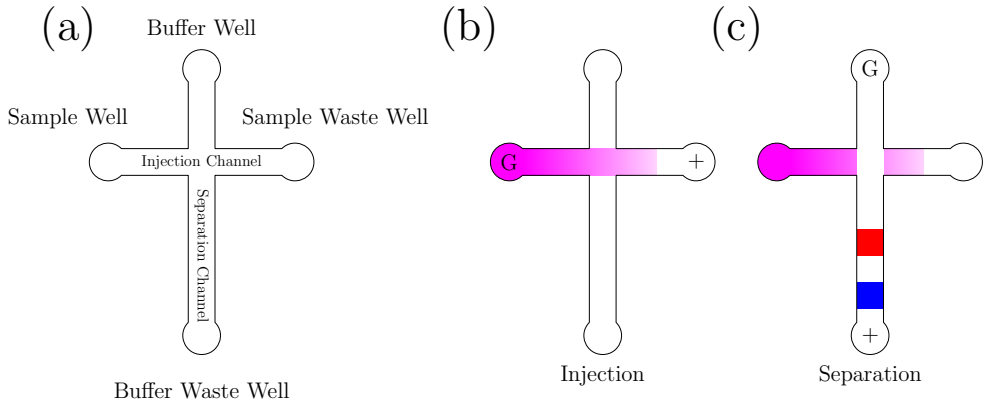

Figure 2.1: Demonstration of microchip CE: a) Annotated drawing of the CE chip: Channels are filled with sieving matrix; Sample well is loaded with DNA sample, while the rest of wells are loaded with CE running buffer. b) Injection step: DNA strands are moved towards the positively-charged electrode, c) Separation step: After injection, the electric field is applied across the separation channel. DNA samples in the intersection (a sample plug) are pulled towards the buffer waste well. Then the plug is separated into discrete bands of DNA, based on their length.

2.3.2 Resolution

An important criterion in DNA analysis by CE is the resolution. It is a quantitative measure of how well each band is separated or how well we can distinguish the bands of different sizes. There are many different ways of defining the resolution. For this thesis, the resolution, Res, is estimated by using Eq. 2.1. The number of base pairs (L) for the DNA strand is known either from the specification sheet if we are using a ladder or from the design of the PCR protocol, which should yield a DNA product of known size. The full width at half maximum of peak height (w) is used to represent the width of the band. The time difference ($t_1 - t_2$) represents the separation distance of both peaks. The fraction of width over time represents how many additional peaks could fit between the two peaks. Thus, the result from Eq. 2.1 represents the increment of DNA base pairs for each

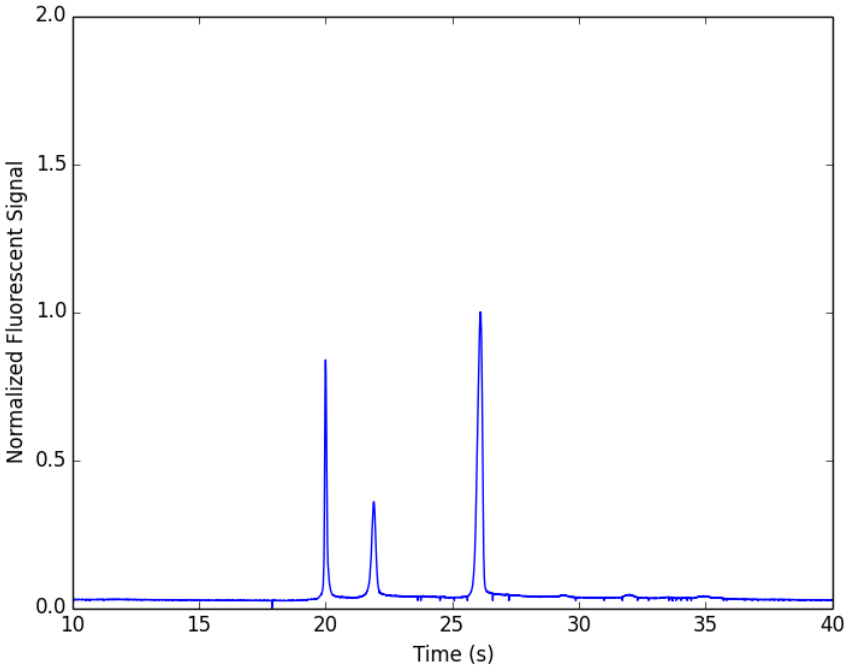

Figure 2.2: A sample electropherogram generated from HV1 CE using HPC as sieving matrix. The CE conditions are the same as described in Section 2.7.1. A electric field of 280 V/cm is applied across the separation channel.

additional peak with half maximum separation. Therefore, the result is a good indication of how well we can distinguish DNA strands of different sizes.

$$Res = (L_2 - L_1)\frac{w_1 + w_2}{t_2 - t_1} \tag{2.1}$$

where 1 and 2 represented the 1st and 2nd peak on the plot; L is the number of base pairs for the DNA strand in each band; w is full width of each peak at the half maximum level; t is the arrival time at the detection point for each peak.

2.4 PMMA

As stated in the introduction section of this chapter, PMMA-based electrophoretic devices have been studied considerably by others. (e.g., Dubrow [22]) However, the CE performance clearly depends on the nature of the substrates as shown by Pfleging et al. [17]. Therefore, it is important to choose the well-studied PMMA as the starting point.

PMMA Grade: Cast And Extruded

PMMA, based on its fabrication process, is classified into two grades: extruded and cast. As indicated by the name, the cast PMMA is made by pouring molten PMMA into a cast to solidify; extruded PMMA is continuously extracted from molten PMMA to form a thin layer. The extruded PMMA has more built-in stress compared to the cast PMMA type, which is seen as heat affected zone after laser ablation as shown by Cheng et al. [27]. In addition, we have observed that extruded PMMA tends to shrink by about 2 % as seen after 130 °C heat treatment prior to bonding. In terms of the laser-ablated surface, Pfleging et al. [17] have demonstrated that cast PMMA has a more porous surface than the extruded PMMA, which has less or no pores on the laser ablated surface. Therefore, extruded PMMA is selected due to its smooth side wall of the channel.

PMMA Substrate The PMMA substrate used in this work is extruded Acrylite-FF, ordered from Evonik Industry. It is the North American equivalent of the Plexiglas XT used in Europe and Asia, as provided by Evonik Industry. This substrate is the same material used in the publications by Pfleging et al. [17].

2.5 Laser Fabrication, Characterization and Development

As stated in the introduction section, the laser ablated channels could be significantly different based on the PMMA property and the laser system. Thus, an initial laser ablation protocol was developed in our lab by Dr. Backhouse. However, in this original protocol the debris generated during the ablation process was not considered. Further, the channel smoothness was not considered as important as the channel width and depth. As suggested by the literature, I modified the protocol to minimize the amount of debris by fabricating on both sides of the substrates and characterized the channel smoothness by using my cracking technique. In this section, I focused on my modifications to the laser fabrication protocol.

2.5.1 Laser System

The Universal Laser system model VLS2.3 is a bench-top CO_2 laser engraving machine. A 30 W 10.6 μm CO_2 laser module is used to generate the high power laser beam and is directed though computer-controlled stage. According to the manufacturer's specification, the maximum speed is 32 inches/second. The laser operates in pulse mode with a maximum pulse density of 1000 pulses per inch. Through a 2 inch focusing lens, the laser beam is focused into a 25 μm spot as per manual.

The auto-z function is used as the default focusing method. According to the laser operating manual, the laser should be focused on the top of the substrates in order to achieve the finest features. There are two methods of focusing: manually focusing using the laser focus tool for each substrate or using the auto-z function. The auto-z function automatically adjusts the laser table z-axis based on the material thickness set by the operator. For example, if the material thickness is set to 1.5 mm, the cutting table will adjust to 1.5 mm below the calibrated position before engraving. The auto-z function is chosen for its simplicity.

However, for the auto-z to work correctly, the laser cutting table needs to be calibrated such that the laser is focused on the top of the cutting table surface when the material thickness is set to zero as stated in the maintenance section. As stated in the manual, the laser should be calibrated if either the laser module or the lens was adjusted. (e.g., laser module replacement and lens cleaning) Thus, it is always important to verify the laser focus using the focusing tool before any focus sensitive fabrication as described in the cutting table section of the laser manual. However, in order to maintain fabrication consistency

between users, no calibration to the laser table should be performed until it is discussed with all other users as stated in the protocol. If calibration is determined necessary, the operator should follow the procedures on Page 86 of the laser operation manual.

2.5.2 Chip Design For Laser Machining

The CE-cross chip design is a standard design used for CE, as demonstrated by others and in our previous publications. [15, 28, 29]. The specific design presented in Fig.2.4, which originated from our glass chip design [15], was modified to accommodate the laser ablation. The design files for the PMMA chips were created with Asymptote (a graphics language) [30] and output as postscript files. After generating the postscript files,the files are imported into CorelDraw X5 and printed through a Windows driver from Universal Laser Systems. (Universal Control Panel, Version number 5.31.54.5)

Based on the glass 4-port-mini chip design, an initial design file, BCSv4.eps, was developed by Dr. Backhouse. In this initial design, the reservoir location and chip size are the same as the glass chip. The separation and injection channels are approximately 19.6 mm and 16.7 mm in length respectively. However, sharp corners are used to replace the curved corners. The intersection is redesigned into a double-T shape. The intersection defines the plug size and has great impact on resolution and reproducibility of the CE chip. Since the laser engraves each line one after the other, the standard cross chip design will have the intersection ablated twice, which leads to double the depth. Air bubbles tend to be trapped in the recessed volume and leave the intersection more hydrophobic than the rest of the channel. Thus, in order to have uniform channel depth, the chip was designed with a double T intersection and had each channel engraved twice as shown in Fig.2.4. Further, the interfaces between channels and the well (intersections of the blue and red lines) are enforced with 3 short blue lines drawn atop. The laser control program cuts every line drawn in the picture. As a result the joints of the well and channel were cut by the laser three times more, which led to deeper and wider interfaces. These extra cuts made more reliable electrical connections between running buffer in the well and the sieving matrix. In addition, alignment marks were added for optical detection.

In order to optimize the CE operation, the design file was further modified as shown in Fig. 2.3. In the original design file, there were eight alignment marks placed to mark the distance from the intersection, which ranges from 5 mm to 12 mm with 1 mm increments. Only one out of eight alignment marks was kept at 11 mm and placed beside the channel. The original alignment marks were hard to distinguish under the μTK optics, and there was a high possibility of aligning to the wrong position. In addition, the alignment marks

and the channels were placed on different plates, which required high accuracy alignment. Thus, by placing the alignment mark and channels on one PMMA plate, the required alignment accuracy is reduced. Since there is no feature on the sealing plate, the user can align two plates easily without using a specialized alignment jig. Further, the code was modified so that the four channels were created from A to D as shown in Fig. 2.4. By doing this, the channel between buffer and buffer waste well was ablated last. Thus, there was no narrow region in the separation channel (the center of the horizontal channel) as shown in Fig. 2.5.

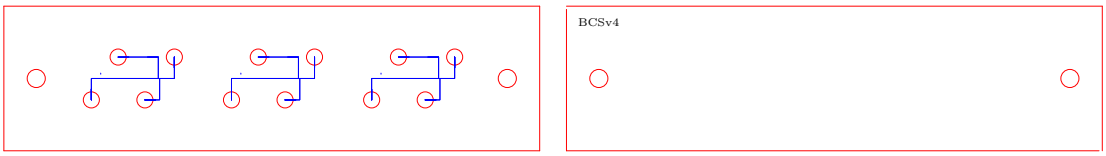

Figure 2.3: Composite design of 3 small electrophoretic separation chips, each containing two intersecting channels that link 4 wells of approximately 6 μL in volume. The chips are held in a larger assembly 10 cm x 2.7 cm in size, and contain 2 alignment holes. The left plate is the channel plate which contains the channel and wells. The well at the top left of each is the buffer waste (BW), that on the top right is the sample well (S), that on the bottom left is the sample waste (SW) and that on the bottom right is the buffer (B) well.

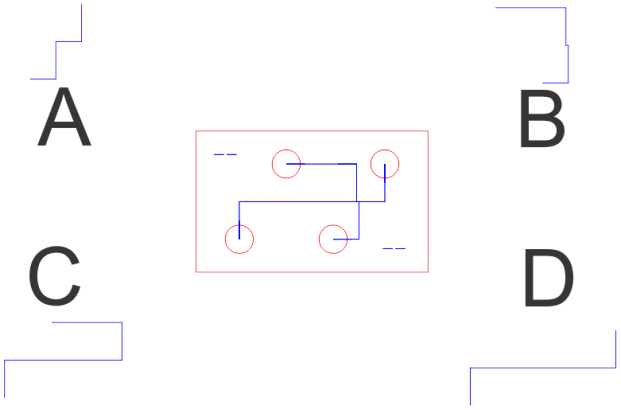

Figure 2.4: Chip design for laser ablated PMMA chips. The double layer channels and double -T intersection are formed by overlay A, B, C and D channels shown around the chip. The four channels were created in the order from A to D.

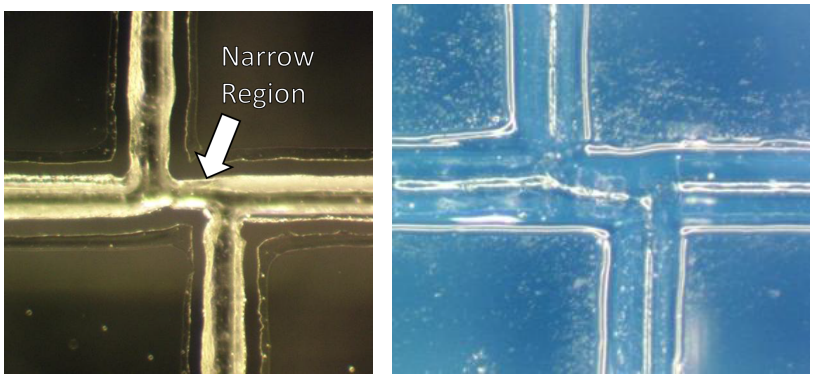

(a) (b)

Figure 2.5: Images of the intersections with and without a narrow region: a) Intersection ablated by the original design file; b) Intersection ablated by the modified design file. There is no narrower region along the separation channel (the horizontal channel). The images were taken at different zoom factors. Both channels had similar channel width. (Note: All the images were taken with the stereo microscope used in Section 2.5.4.)

2.5.3 Laser Engraving Protocol

Instead of printing the design files directly as in the initial protocol, the engraving protocol was modified to ensure higher channel cleanness. In this section, each modification is explained.

First, the PMMA substrate was placed in front of the exhaust of the laser table by a taped down alignment frame. By doing this, the strong air flow carried most of the ablated PMMA away and left a cleaner surface.

Second, the laser vector cutting and the channel engraving were performed on different sides of the PMMA plates. After printing to the Universal Control Panel, the design file was laser ablated in two steps. The black raster and red vector cut were printed first. Two plates were cut out from the PMMA sheet. Each plate was approximately 10 cm long and contained two alignment holes as shown in Fig. 2.3. The channel plate, the plate with wells, was flipped upside down before engraving the blue channels. This modification solved two problems with the initial protocol. First, by ablating the channel after the well, the PMMA re-flow caused by the well cut is eliminated. Thus, the well-channel interface is kept open as shown in Fig. 2.6. Second, the amount of debris deposited around the channel region is significantly reduced. Since the amount of debris generated is proportional to the amount of PMMA removed by laser ablation, the well-cut generates much more debris than the channel engraving as shown in Fig. 2.7.

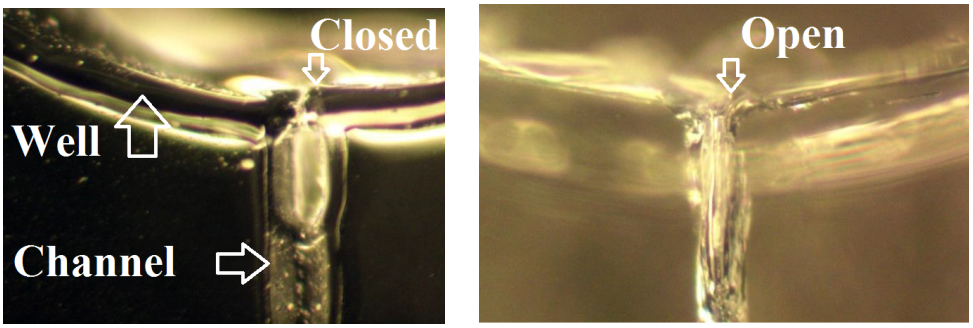

(a) (b)

Figure 2.6: Images of the well-channel interfaces generated using two different approaches: a) The channel was ablated before the well; b) The channel was ablated after the well. If the channel is ablated before the well, the heat generated by the well cut can cause reflow of the PMMA around the well and lead to closed channels.

Third, different z-axis settings were used for different features. As described in Section

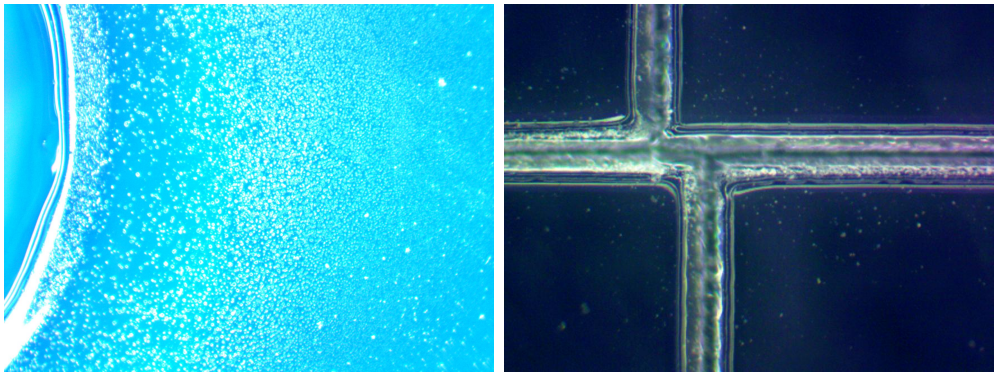

(a) (b)

Figure 2.7: Images of the debris generated by different laser ablation settings: a) Debris along the well cutting line; b) Debris along the ablated channel. The well-cut lines generated much more debris along the path than the channel ablation. In order to minimize the amount of debris on the channel surface, the channel is ablated on the other side.

2.5.1, the laser focus is adjusted by the z-axis setting. Thus, the laser beam is in focus when the Z-axis is set to 1.5 mm (e.g., black raster). However, the blue channel lines were 0.7 mm out of focus in order to achieve a smooth channel bottom. More details are explained later in Section 2.8.2. Further, the well-cut lines were out of focus by 1.5 mm. This was intended to ensure smooth well edges, which is crucial for a leak-free seal between the pipette tip and the well during the chip cleaning procedure of the CE protocol.

Distinct laser settings were assigned to different colors at each stage to distinguish the difference between the shallow engraved channel and the deep through cut. Table 2.1 summarizes the laser settings for each color.

Mode	Color	Power (%)	Speed (%)	PPI (%)	Z-axis (mm)
Rastering of text	Black	36	100	500	1.5
Vector cut of frames	Red	20	3	1000	3.0
Engraving of channels	Blue	0.8	3	1000	0.8
Vector cut of individual chips	Red	100	8.6	1000	0.0

Table 2.1: Laser driver settings for laser ablation.

2.5.4 Channel Characterization: The Cracking Technique

In contrast to approaches described in the literature, the laser ablated channels were characterized laterally. In the literature, it was most common to show the cross-section view of the channel. However, the v-shaped cross-section does not provide information about the lateral direction along the channel. The lateral information could be critically important as presented in Section 2.8.2. Thus, instead of the v-shaped images the top and lateral cross-section images of the channels were used to determine the channel characteristics.

In order to obtain the lateral cross-section information, a technique referred as cracking technique was used to show the side view of the channel. As shown in Fig. 2.8, PMMA coupons are laser ablated at different focus setting with the same channel engraving parameters as listed in Table. 2.1. In the design, two blue lines were drawn on each other to simulate the CE channels which ablated twice for the double-T intersection. After ablation, the bottom right section of each coupon is cracked off by used two pairs of flat-head pliers alone the engraved line.

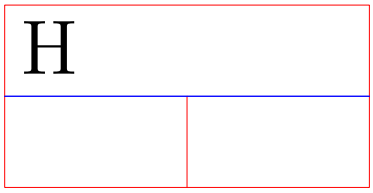

Figure 2.8: Design of the PMMA coupon for the cracking test. The bottom right section will be cracked off in order to show the side view of the blue ablation line. In order to show the effect of the CE channel, the same channel engraving parameters are used for the blue line.

The top and side-view images of each coupon were taken to characterize the channel. A stereo microscope with a camera (model zm-4tw3-for-9m, from AmScope, California, U.S.A.) was used to take images of the channels. A top view image was taken for the left half of the channel in order to measure the channel width. Then, the coupon was inserted into a binder clip and placed with the channel side up in order to take the lateral cross-section images of the channel. Fig. 2.9 shows the top and lateral cross-section images of the engrave channel with laser setting in Table 2.1 except the z-axis was set to 1.5 mm (in focus cut). The laser beam was set in focus to show the rough channel bottom. The width and depth were 106±5 μm and 144±16 μm respectively. The higher uncertainty of the channel depth was a result of the bumps at the bottom, which were results of the pulse mode laser. It is clear that by examining the chip laterally, not only the width and

depth of the channel but also the channel smoothness were obtained. For quality control, a sample chip of each batch was cracked along the separation channel to verify the channel smoothness.

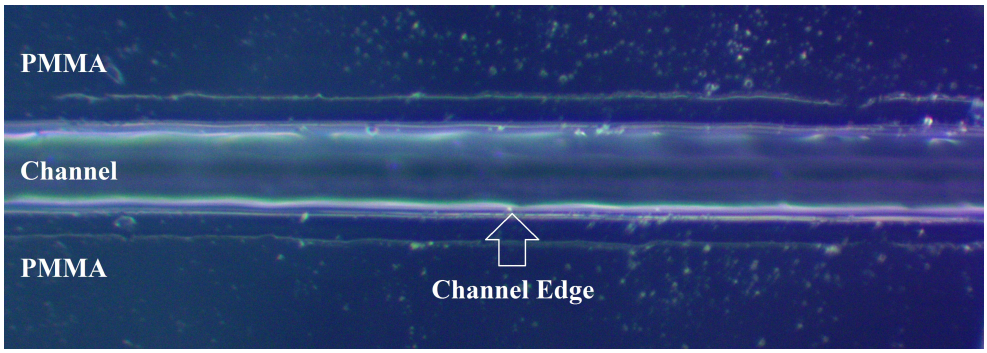

(a) Top View

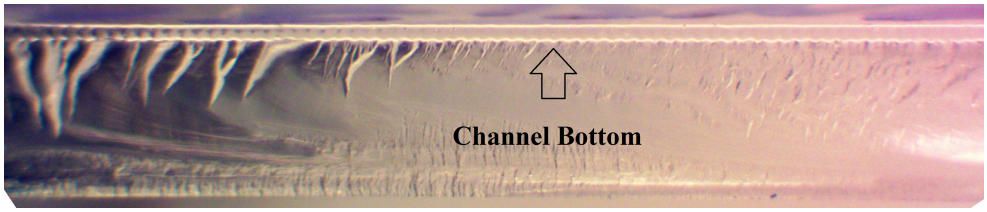

(b) Lateral Cross-section View

Figure 2.9: Cross-section of CE chip channel: from the images, the width of the channel is 106±5 μm, and the depth is 144±24 μm. The large uncertainty of the depth is caused by the bumps at the channel bottom. In order to show the bottom smoothness, the channel was ablated as per fabrication protocol, except the laser beam was set to be in focus.

2.6 PMMA Bonding And Development

An improved PMMA bonding protocol was developed to ensure reproducibility of the PMMA CE chips. In order to form microfluidic channels, the bonding process is crucial to the fabrication of the PMMA microfluidic chips. As reviewed by Chen et al. [31] and Tsao and DeVoe [32], there are a variety of bonding techniques available, such as thermal bonding, solvent bonding and others. Thermal bonding usually requires heating the assembled substrates to above the glass transition temperature, T_g, of PMMA, and a positive pressure in the region of 130-150 KPa is applied during the bonding process. [33, 34]

However, the pressure and the relatively high temperature could cause micro channel deformation, which might lead to clogged channels and affect the reproducibility. There are variants of either low temperature (95 °C)/high pressure (1 MPa) [35] or high temperature (165 °C)/low pressure (20 KPa) [25] that have been demonstrated, but they face the same problem in that the PMMA is soft and may deform during the process. Solvent bonding of PMMA has been demonstrated at temperatures much lower than T_g or even at room temperature [36–38], but the deformation of the channel is still a challenge depending on the type of solvent and the exact condition used. In addition, the exposure of the channel to the solvents could lead to unwanted surface modification or filled channels with softened PMMA. In order to solve this, Kelly et al. [39] used a phase-changing sacrificial layer to fill the channels before solvent bonding in order to prevent the exposure. Despite the protected channel, this is a much more complex process than regular solvent bonding. Other bonding techniques, such as adhesive tape bonding and microwave bonding, are usually involved with introducing other materials between the PMMA layers. As a result, it breaks the surface homogeneity of the channel. Utilizing the advantages of both the thermal and the solvent bonding process, Klank et al. [21] had demonstrated the solvent-assist thermal bonding of PMMA by immersing the PMMA layers in ethanol for 10 minutes before lower temperature thermal bonding. The ethanol rinse softens the PMMA surface and assists thermal diffusive bonding of PMMA. The required temperature and pressure are significantly lower than either single technique alone. Due to the relatively low solubility of PMMA in ethanol, there is no significant channel deformation caused by this immersion process. Therefore, ethanol assisted thermal bonding was chosen.

Based on an initial bonding protocol developed by Dr. Backhouse, an improved protocol was developed with precise cleaning/rinsing steps and surface heat treatment (130 °C for 10 minutes). These modifications are intend to minimize the surface effect and improve reproducibility of CE as suggested by the literature. [25, 27]. A significant amount of effort was spent on the development of the bonding process to optimize the chip performance. By following the steps documented below, the chip performance from batch to batch was shown to be consistent as in Section 2.7.1

2.6.1 130 °C Surface Treatment And Annealing

A 130 °C surface treatment was added based on some suggestions that it can improve the uniformity and reproducibility of the channel surface. The work by Cheng et al. [27] has shown that 170 °C treatment for 30 minutes can reduce the surface roughness from microns to nanometers. Further, Sun et al. [25] suggested that the PMMA monomer and broken polymer chain generated by the laser beam could be removed or reconnected by near-180

°C baking. By bonding their chip at 165 °C, the EOF of their chip was comparable to the native PMMA. However, it clearly relies on the properties of the PMMA substrates. After baking at 160 °C for 10 minutes, the Acrylite-FF substrates was completely melted and unable to retain any features.

In addition, the PMMA vapor generated by the ablation can readily condense near the region of ablation to form a liquid on the surface (referred to as sweat). The monomers can be absorbed into the bulk PMMA or evaporate, while the less- completely degraded polymer is left as a particulate residue on the surface. In an effort to minimize this effect, the laser engraver system is forcefully vented (at about 150 cfm). However, there is still noticeable amount PMMA residue deposited around the ablation area.

As suggested, in order to achieve a uniform channel surface, the laser patterned PMMA strips are placed in a forced-air oven (Model No. 6916, Fisher Sci.) at 130 °C for 10 minutes. Then, the PMMA strips are gradually cooled down to 80 °C and kept for 1 hour for additional annealing. 130 °C is the maximum temperate before the Acrylite-FF loses its laser ablated feature.

2.6.2 Solvent Bonding

After 130 °C heat treatment, the laser patterned PMMA strips were rinsed in nominally 99.9 % ethanol for 30 s, then blown dry for 15 s by blowing dry clean air. The assembly was sandwiched between two microscope stacks and clamped with standard stationary Bulldog paper clip (Staples, Canada) and placed again in the oven for an hour at 110 °C, and then allowed to cool to room temperature. The assembly now contains three bonded microfluidic chips that are cut free using the detachment power settings (for PMMA that is now 3 mm thick). The chips are then annealed again for an hour at 80 °C. At various stages in their fabrication, the chips were inspected with a stereo microscope and camera.

2.7 Capillary Electrophoresis Characterization

In this section, the CE performance of the PMMA chips was evaluated using two different sieving matrices, HPC and agarose. Sample electropherograms are presented for clear demonstration. As mentioned above, there have been significant developments in laser rapid prototyping microfluidic devices. However, there are few published articles about laser ablated channels being used for DNA separation. One of the few exceptions is the work by Sun et al. [25] and their work is still the best representation of the laser ablated

channels for CE in the field. In contrast, PMMA micro channels fabricated by other techniques, such as wire imprinting [40] and injection molding [41], have been presented in various publications. The surprisingly little work with the laser ablated channels could be related to the depolymerization of PMMA, which is described by Sun et al. [25]. The redeposited debris on the surface could lead to uneven EOF inside the channel, which affects the resolution of DNA separation. As suggested by the literature, the channel surface was reconditioned to its original state by reducing the amount debris generated and the 130 °C high temperature treatment. This is most likely the main reason for the successful demonstration presented in this work. Since this section is focused on the CE performance, I only present representative results for each sieving matrix.

In terms of criteria for DNA mutation detection following a PCR, Ugaz et al. [42] estimated that a resolution of 20 bp (adjusted based on 2.1) was the minimum requirement for effective sizing of DNA less than 1 Kbp. So this criterion is used to evaluate the CE performance for both sieving matrices.

2.7.1 Capillary Electrophoresis: Hydroxypropyl cellulose (HPC)

I started with the glass chip CE protocol developed in our lab, and so commercially available sieving matrix, POP7, was used. However, the PMMA chips delaminated shortly after being exposed to POP7 polymer. The exposure time before delamination occurred varies from chip to chip, but five out of five test chips exposed to POP7 were delaminated after testing. Prior to the testing, all chips were optically inspected and cleaned with pressurized water. No sign of leakage was observed during the inspection. For comparison, a chip from the same batch was loaded with HPC and stored overnight with no sign of delamination. The ammonia content in the POP7 matrix is the most likely cause for the delamination due to its strong basicity. HPC was chosen as the alternative due to its performance and EOF control as demonstrated on glass chips by Sanders et al. [43]. For using the new sieving matrix, a protocol for HPC was updated from the original glass POP7 protocol. The CE electropherogram presented is performed as described in the protocol with the HPC made by Dr. Glerum, following a protocol based on the work of Sanders et al. [43].

Reagents And Sample Loading

The 3.5% HPC polymer solutions was prepared by dissolving the polymer in an appropriate amount of 5x TBE buffer. The solution was stirred overnight and then diluted to final concentration with Mill-Q water. The diluted solution was then stirred to allow for

sufficient mixing. The final solution was degassed and filtered through a syringe filter with 5 μm pore size. 1x TBE buffer and 0.1x TBE buffer were diluted from the 5x stock solution prior to sample loading. The channel was first filled with the sieving matrix. Then, 2 μL DNA samples (usually PCR products) were diluted with 8 μL 0.1x TBE buffer and loaded in the sample reservoir. 10 μL of 1x TBE buffer was loaded in each of the other three reservoirs.

CE Resolution

The filled chip then placed in the μTK system for CE. The detection module was placed 11 mm away from the intersection and an equivalent of a 280 V/cm electric field was applied during the CE process. A sample HPC CE electropherogram is shown in Fig. 2.10. Two PCR product samples, $\beta 2M$ (236 bp) and HV1 (364 bp), were loaded and separated. The calculated resolution is 20.9 bp for the run shown in Fig. 2.10. This resolution is comparable with our prior work with glass chips [15] in that our resolution ranged from 20 bp to 40 bp, depending on the separation distance. According to Ugaz et al. [42], this resolution meets the minimum requirements for effective sizing of DNA in the 100 - 1,000 bp range.

Reproducibility

In order to demonstrate the reproducibility of the improved fabrication protocol, five batches of the CE chips were fabricated over the course of two months, following the same fabrication protocol. A test chip was selected randomly from each batch and tested by performing HPC CE with the β2M PCR product following the HPC CE protocol. Four out of five batches of chips demonstrated similar CE performance with HPC, as shown in Fig. 2.11. The other batch had a resolution 3 times worse than others, but it is likely caused by a 5-day delay during the bonding process. The bonding was performed 4 days after the 130 °C treatment due to a unexpected oven failure.

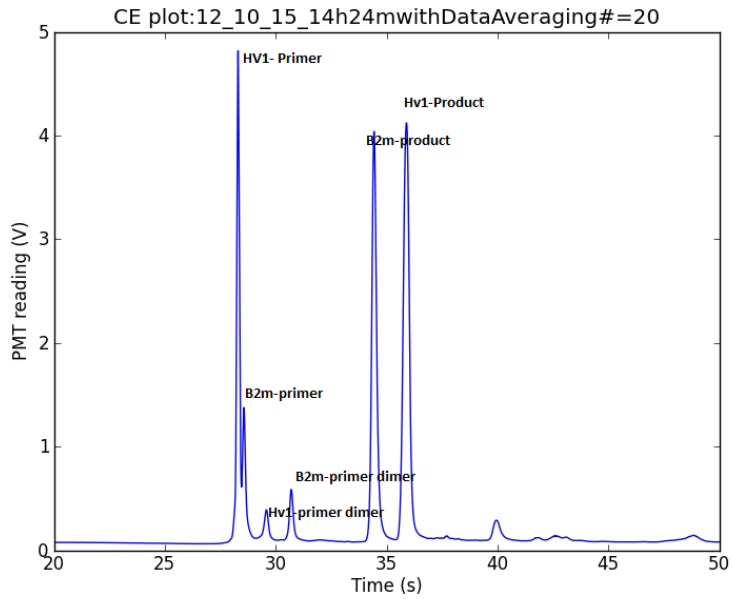

Figure 2.10: HPC CE electropherogram at 280 V/cm at 11 mm using β2M and HV1 products: a resolution of 20.9 bp was demonstrated. This resolution is the same as the resolution with the glass chip at similar separation distance [15] and is sufficient for sizing common diagnosis PCR products according to the work by Ugaz et al. [42].

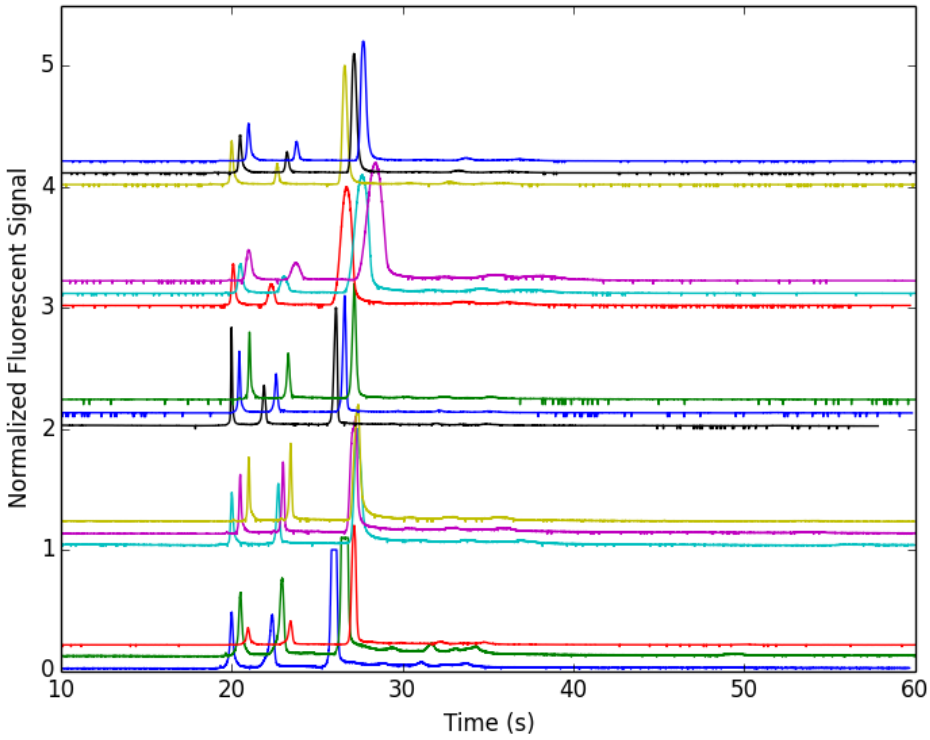

Figure 2.11: Electropherograms of HPC CE with B2M PCR products. From bottom up, the 5 groups of electropherograms were CE results of chips fabricated on 2012-08-13, 2012-08-20, 2012-08-28, 2012-09-04 and 2012-09-26. Each group consists of the 3rd, 4th and 5th injection of the 1st load for each chip. In order to generate the plot, the 1st peak of each electropherogram was aligned to the 20 s mark. Then, in each group a half second offset was introduced for each run in order to show clear peaks. The 2nd group from the top had a resolution 3 times worse than others, and it is likely caused by a 5-day delay prior to bonding due to unexpected oven failure.

2.7.2 Agarose Capillary Electrophoresis: Old Material With A New Application

Inspired by the conventional agarose slab gel technique, agarose was used in the polymer chip as a solid (or semi-solid) sieving matrix for CE. Hong et al. [44] in their earlier work had demonstrated the use of agarose on a PDMS/PMMA microchip. An electric field of 71.4 V/cm was applied across the 400 μm wide channel filled with 2 % agarose. The achieved resolution is about 100 bp in the 200 to 300 bp range, at a separation distance of 8 mm. Similarly, Ugaz et al. [45] demonstrated similar 70 bp resolution at a 10 mm separation distance on a glass/silicon chip. An agarose concentration of 1% was used to fill the channel, and a 30 V/cm electrical field was applied across the separation channel, which is 40 μm deep and 400 μm wide. The lower concentration of agarose was intended to ease the replacement of agarose matrix after use. Later, Zhao et al. [46] demonstrated a resolution of about 30 bp on a PDMS/glass microchip filled with 2 % agarose. The imprinted channel was 65 μm deep and 17 μm wide. The separation distance was 35 mm with an applied electrical field of 110 V/cm. Improved resolutions are expected from the longer separation distance. Interestingly, Zhao et al. [46] got around the agarose refilling problem by demonstrating durability of the agarose matrix. After 34 runs of a single fill, the agarose matrix was still capable of sufficient separation.

As suggested by these earlier work, agarose might not be able to provide sufficient separation for post-amplification analysis of DNA and comparable resolution as other commercial CE systems. (e.g., 5 bp as specified by the Bio-Rad Experion System Manual) However, the high durability and solid nature of agarose presents an interesting future for off-the-shelf operation. By pre-filling the microchip with agarose, the end user could avoid the complex filling process and be ready to perform CE in seconds. Since agarose is a solid in the channel, it is much easier to store in a sealed package. Further, the agarose is less susceptible to EOF, which is a flow of fluid by electric field due to surface interaction. Since the polymer matrix is solidified in the micro channel, EOF of fluid is largely suppressed compared to the liquid based sieving matrices. In addition, the work by Zhao et al. [46] suggested that a better resolution could be achieved in longer channels. Thus, if a small chip size is not critical, a better resolution is likely to be achieved.

In our lab, my colleague, Victoria Northup, and I jointly demonstrated CE with agarose using the PMMA CE chips. The CE runs were performed by Victoria Northup. The chip fabrication and the post-experiment channel inspection were performed by Tianchi. It is important to mention that these chips were from the earlier batches, fabricated with a focused laser beam and different from the chips used for HPC.

For demonstration purpose, the CE results for $\beta 2M$ PCR product separation in 2 %

agarose are shown and the separation of 100 bp ladders in a 0.65 % gel (separation of the 100 bp ladder up to 1.5 Kbp) are shown in Fig. 2.12 and Fig. 2.13 respectively.

Unfortunately only the $\beta 2M$ product was loaded to run CE by Victoria. An electric field of 100 V/cm was applied, and the detection point was 11 mm away from the intersection. I cannot calculate the real resolution of Fig. 2.12 as there is only one peak for double-stranded DNA, so I estimated the CE performance by calculating the fraction of product peak width (w) over the time difference between the product peak and the primer peak, $\frac{FWHM}{(t2-t1)}$. However, this is a crude approximation compared to the real resolution value. The calculated values in agarose and HPC are 0.188 and 0.042 respectively. Thus, the resolution for the agarose is estimated to be 4.5 times worse, about 90 base pairs. Nevertheless, this estimated resolution is similar to that of the work demonstrated by Hong et al. [44].

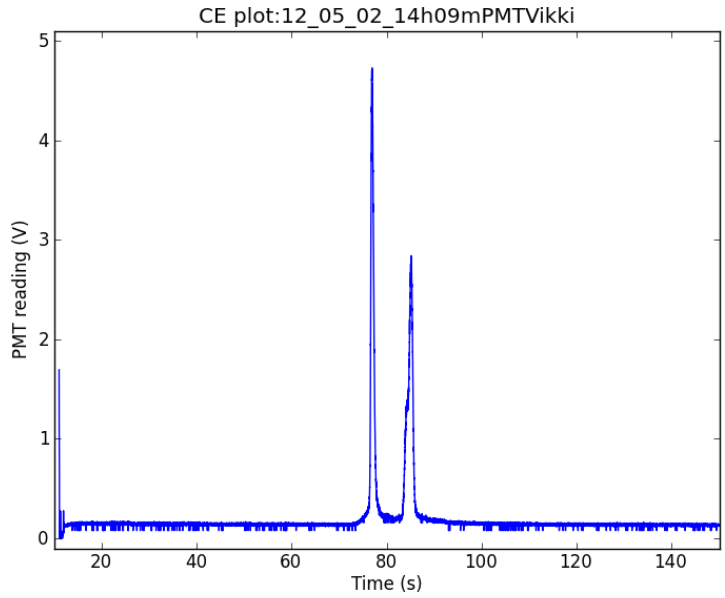

Figure 2.12: CE separation in 2 % agarose using β2M product on a laser ablated CE PMMA chip: the product and the primer are well separated. An electric field of 100 V/cm was applied for both injection and separation. The detection point was set at 11 mm. Comparing to HPC-β2M separation, the $\frac{FWHM}{(t2-t1)}$ for agarose and HPC are 0.188 and 0.042 respectively. Thus, the CE resolution of 2% agarose is about 3 times worse than HPC and estimated to be 90 bp. This experiment was performed by Victoria Northup. The CE chip was fabricated by Tianchi following the initial protocol by Dr. Backhouse.

For the kilo-bp DNA ladder, 0.65 % agarose was used with an injection field of 42 V/cm and a separation field of 25 V/cm. The detection point was 11 mm away from the intersection. The size standard was a 100 bp ladder (from New England Biolabs, NEB) with lengths of 100, 200, 300, 400, 500, 517, 600, 700, 800, 900, 1000, 1200 and 1517 bp. With the resolution of our chip, the 500 and 517 bands will run together, giving a total of 12 discernible peaks. All peaks are double-stranded DNA fragments. Thus, the real resolution was about 50 bp in the 200-300 bp range. From the electropherogram, it is clear that all 12 different sizes of DNA fragments were well separated.

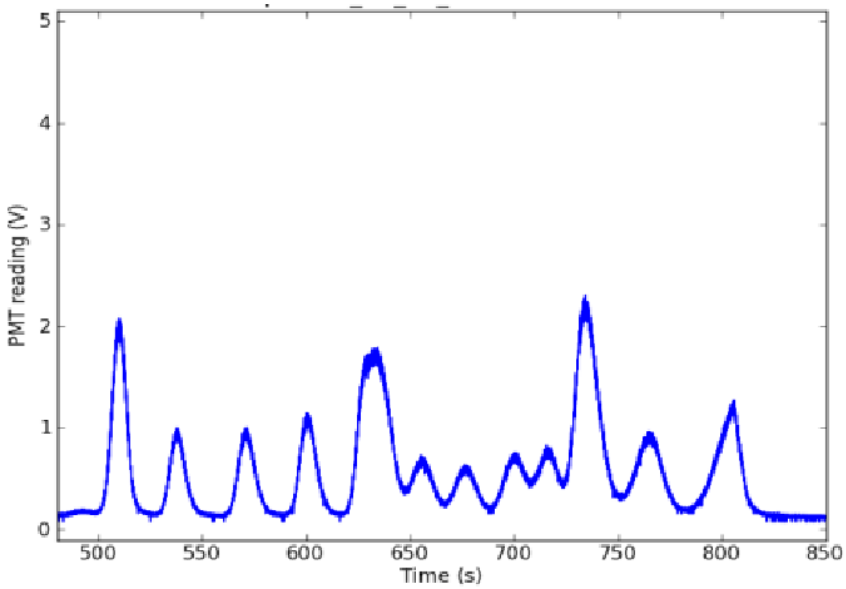

Figure 2.13: 0.65% agarose CE using the 100 bp ladder with a separation field of 25 V/cm at 11 mm after the intersection. The size standard was a 100 bp ladder with DNA fragment lengths of 100, 200, 300, 400, 500, 517, 600, 700, 800, 900, 1000, 1200 and 1517 bp. The resolution was about 50 bp in the 200-300 bp range. All 12 expected peaks are apparent, with the 500 bp and 517 bp bands run together. This experiment was performed by Victoria Northup. The chip was fabricated by Tianchi following the initial protocol provided by Dr. Backhouse.

2.8 Discussion

2.8.1 Resolutions

One of the key characteristics for CE is the resolution. For consistency, the separation distance for both sieving matrices was 11 mm. HPC, as a replacement for POP7, showed 20 bp resolution at 11 mm separation distance on a PMMA chip. This resolution meets the requirement for post-amplification analysis of DNA as suggested by Ugaz et al. [42] which was 40 bp (after adopting the same resolution definition). Agarose demonstrated similar or better resolutions as compared to the literature. Under similar conditions (100 V/cm and 11 mm distance), 2 % agarose had a resolution estimated to be 90 bp, which is the same as the work by Hong et al. [44] and Zhao et al. [46]. At lower concentration, 0.65 % agarose sieving matrix showed a 50 bp resolution with an applied electric field of 28 V/cm as used by Ugaz et al. [45]. Even at low concentration, the agarose resolution in the 200-300 bp range is still about 2 times worse than the HPC matrix. However, as mentioned earlier, the capability of off-the-shelf operation by filling the chip with agarose is a great advantage over the liquid phase sieving matrices. Further, it seems to suggest that agarose separation performs better at lower concentration and electrical field. Future work will be needed to optimize these parameters.

2.8.2 Surface Roughness Vs. Resolution

Since refilling a CE chip with agarose is difficult as described in the literature, the chips used for agarose CE were single use. As mentioned by Hong et al. [44], the filling of agarose could be a challenge due to its high viscosity at 2 % concentration. By reducing the agarose concentration, Ugaz et al. [45] claimed the agarose could be loaded reproducibly. Even though the 1 % agarose could be removed from the device, which allows multiple loads on the same chip, the solid agarose residue could deposit on the channel wall (which was either glass or silicon). For the PMMA chip, agarose had stronger binding to the wall which led to single agarose load of each chip. Even at 0.6 % concentration, it was found to be difficult to completely remove the agarose from previous fills during our CE test. As a result, a large number of chips were consumed during the experiments. Importantly, these chips were fabricated in different batches before the defocused laser beam was used. Thus, the laser focus was not well controlled as the updated protocol provided. As a result, during the testing process, a large variation was observed from chip to chip in terms of resolution for long base pair DNA strands.

By using the cracking technique explained in Section 2.5.4, representative PMMA chips based on resolution were examined laterally and photographed. A collage was assembled from the images, showing the last 3 mm section of the separation channel as shown in Fig. 2.14. Three electropherograms are presented, on the right side, for the 1st, 3rd and 5th chips, respectively. From Fig. 2.14, it is clear that the surface roughness has a strong correlation with the CE resolution. The resolution, separation range and channel roughness for all five chips are listed in Table. 2.2.

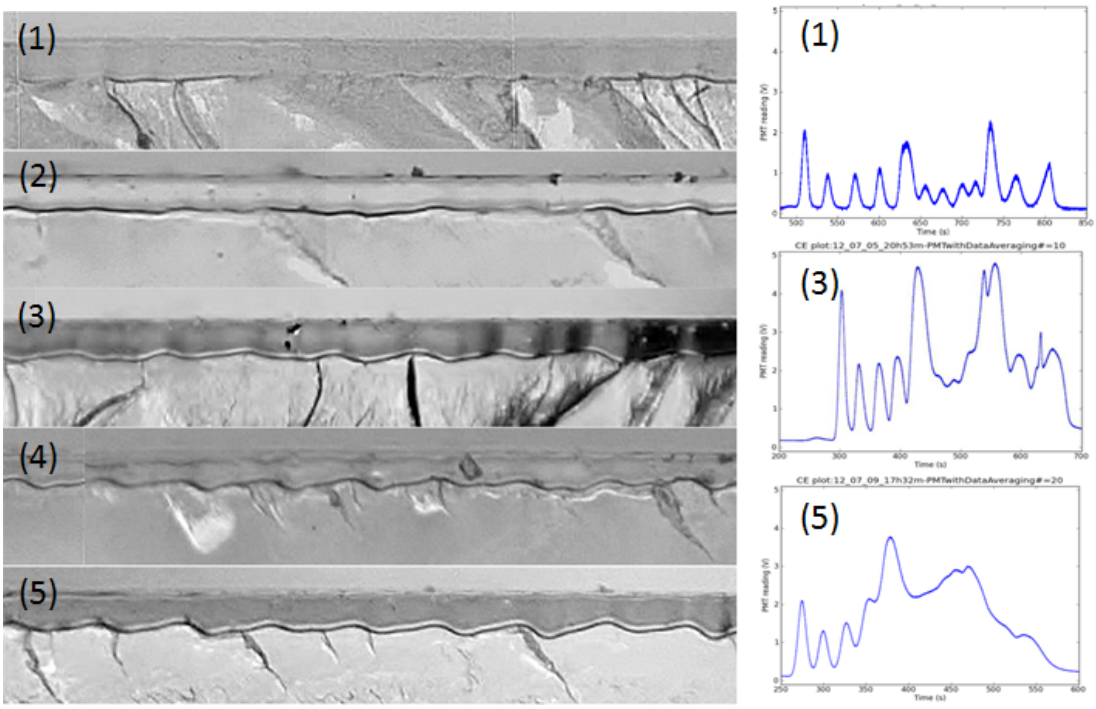

(a) (b)

Figure 2.14: Channel roughness vs chip performance: a) Collage showing depths of each channel, the channel roughness increases from the top to bottom; number of peaks resolved using 100 bp ladder for each chip is: 12, 5, 4, 3 and 2 respectively; b) Representative electropherograms for the 1st, 3rd and 5th chips.

Further, the periodic bumps at the bottom of the channel were found to be generated by the VLS laser pulse. Since our laser system operates in pulse mode, which is intended for finer feature size, the channel was ablated by a series of equally spaced dots as determined by the laser control program. The highest pulse rate available is 1000 pulse per inch (or 25.4 μm spacing between dots). From Fig. 2.14, the depth of bumps is inversely

Chip No.(as in Fig.2.14)	Channel Roughness	Resolution	Separation Range	Total Number of Resolved Peaks
1	$10.5 \pm 3\mu$m	50 ± 10 bp	100-1500 bp	12
2	$12.0 \pm 3\mu$m	100 ± 10 bp	100-800 bp	5
3	$15.0 \pm 3\mu$m	130 ± 10 bp	100-400 bp	4
4	$16.5 \pm 3\mu$m	150 ± 20 bp	100-300 bp	3
5	$22.0 \pm 3\mu$m	160 ± 20 bp	100-300 bp	2

Table 2.2: Resolution and separation range vs. channel roughness. The channel roughness is defined as the bump height at the bottom of the channel. Resolutions for all chips are calculated for the 200-300 bp region. The separation range is determined by the maximum DNA species length that could be resolved.

proportional to the quality of CE separation and cut-off number for maximum resolvable DNA strand length. In order to reduce the bump depth, the laser beam was defocused to evenly distribute the laser power as shown in Fig. 2.15. A series of test cuts was made with the laser focused from 2.4 mm above to 0.8 mm into the PMMA substrates, in 0.2 mm steps as described in Section 2.5.1. As shown in Fig. 2.16, the relative channel roughness (bump height to channel depth ratio) decreases as the laser focus moves into the substrates. However, the relative channel roughness stays nearly constant while laser focus moves in the opposite direction. Therefore, the final laser focus is set to 800 μm into the surface. By doing this, the bump depth dropped from 24.5 μm to 12.5 μm as shown.

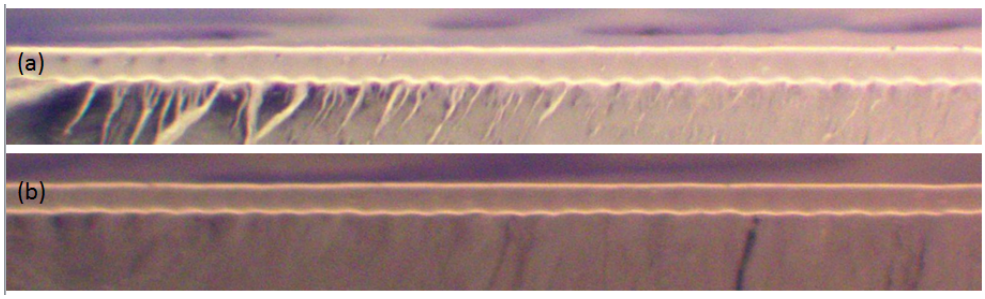

Figure 2.15: Channel roughness vs laser focus: a) Laser beam focused on the top of the PMMA surface and the bump depth is 24.5 ±3 μm. The channel is 106±5 μm wide and 144±25 μm wide. b) Laser beam was out of focus by 800 μm into the substrate, and the bump depth was 12.5 ±3 μm. The channel is 128±5 μm wide and 120±12 μm deep. By defocusing the laser, the channel roughness was reduced by near 50 %.

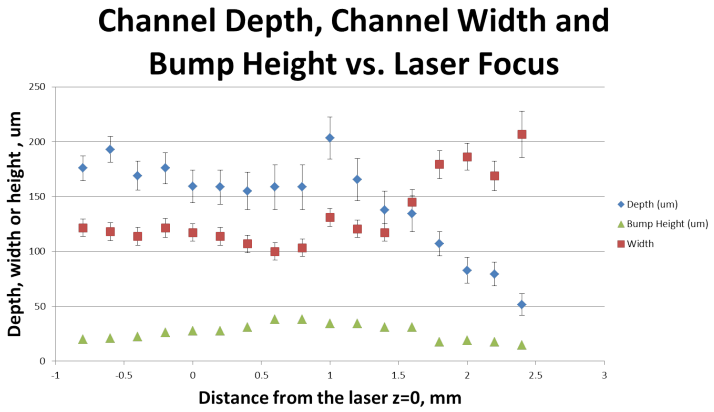

(a)

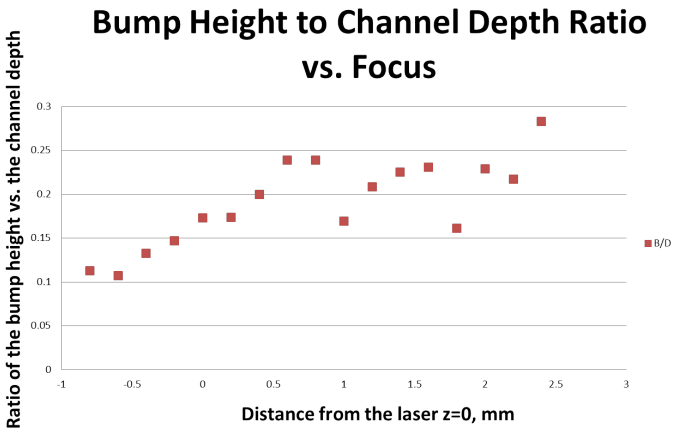

(b)

Figure 2.16: Plot of channel characterization vs. laser focus: a) Plot of channel depth (blue diamond), channel width (red square) and bump height (green triangle) vs. laser focus. b) Plot of the bump height to channel depth ratio vs. laser focus: Laser beam focus was adjusted from 2.4 mm to -0.8 mm relative to the substrate surface in 0.2 mm increments while a test chip was ablated at each setting. The bump height to channel depth ratio is plotted as a function of the focus distance (z-axis). From the plot, the ratio decreases as the laser focal point moves into the substrates. The ratio is relatively constant when laser focal point moves in the other direction.

2.9 Summary

In this chapter, I present the development of the standard operating procedure (SOP) for both chip fabrication and running with HPC sieving matrix. By following this protocol, the HPC has demonstrated sufficient resolution, 20 bp, which meets the requirement for DNA diagnosis determined by Ugaz et al. [42]. To the author's knowledge, this is the first demonstration in which HPC was used on PMMA chips. In addition, agarose has proven to be sufficient for PCR product separation, but the best resolution achieved is about two times less than HPC. By using my snap technique, the lateral examination of the chips showed strong correlation between the channel smoothness and CE resolution. This new finding is published in SPIE Photonic North 2012.

Chapter 3

Integration For Hands-Free Operation

Lack of integration is one of the main reasons for current μTAS not being competitive in the clinical market. After demonstrating reproducible fabrication and operation protocols for a CE chip, I continued to work on the fluid handling module, which is intended to be an easily fabricated and integrated valving and pumping system. In this chapter, a novel laser rapid-prototyping mono-layer valve design is demonstrated. In contrast with the normal construction of the diaphragm valve, the presented design utilized a detachable membrane, mono-layer valve structure and reusable external pneumatics. The detachable membrane does not require any bonding process. It is held down by a reusable manifold with standard footprint. Channels and vias are laser ablated into one single layer of PMMA substrate and a tape layer is laminated to the bottom to form a closed channel. The CNC machined manifold is connected to external pneumatic control lines, which consist of air/vacuum source, solenoid valves and a computer control unit. Each part of the valve is aligned within a 50 μm tolerance through 2 alignment pins and held together by 4 screws. This design is fully scalable for further miniaturization, to a portable handhold system and also flexible, for rapid design changes due to rapid laser machining. In addition, we combined this valve design with the CE chip that I previously demonstrated and performed a RFLP analysis for the HFE C282Y mutation. This is a complete demonstration of the system for potential CE diagnosis. This system had been described and demonstrated at IEEE Nano 2014. This valve is one of the major components of a paper about to be submitted to Journal of Micromechanics and Microengineering.

3.1 Introduction

As mentioned in the introduction, the lack of integration and automation are the main reasons that the μTASs are not gaining traction in commercialization or getting used outside the research laboratories. [6, 7] In order to move forward, it requires valving and pumping to control and transfer the solutions and reagents. Since pumping could be simply achieved by arranging the valves in series and operating in peristaltic motion, the limiting factor is the microvalves. In the past, various on-chip microvalves have been developed such as pneumatic valves, magnetic valves, phase-change valves and burst valves as reviewed by Oh and Ahn [47]. However, there seem to be few new developments in this area. In the most recent review by Au et al. [48], the author presented a thorough overview of the field and focused on valve and pump designs that are available for Bio-MEMS applications particularly. However, the majority of references are dated before the end of the year 2008 (13 out of 117 total reference were published after 2008). Within those new publications after 2008, phase-change valves and burst valves are the new focus. In terms of pneumatic valves, Au et al. [48] used the same reference as Oh and Ahn [47] and indicated little new development. This lack of development of pneumatic microvalves is most likely as the result of the excellent work done by Dr. Mathies's group [49] and Dr. Quake's group [50]. They have demonstrated each of their valve designs in various applications and publications. As stated by Huang et al. [51], the pneumatic valve has been the most widely used valve design. However, it is clear that almost all of the pneumatic valve designs are realized by micro-fabrication, which requires a clean-room and high cost equipment (e.g., lithography and plasma bonding) as in Quake's valve, or labor intensive and reiterative assembly as required by the Mathies's membrane valve. In order to solve this problem, Huang et al. [51] replaced the irreversibly bonded pneumatic control channels with double-sided adhesive. This allows the reuse of the pneumatic control layers and reduces the times of disconnecting and connecting the external pneumatic infrastructure. In earlier work from our group, we had demonstrated on-hip valves on glass-based chips with phase-change actuation. [52] The system requires no external pneumatic control, but the slow phase-change actuation did not allow pumping operation. Mohammed et al. [53] targeted the same goal by using laser rapid prototyping, but their focus is the capillary passive valve design. The closest example of a laser ablated pneumatic valve was demonstrated by Lounsbury et al. [54], which utilizes laser ablated vias as valve ports. However, the valve actuation was done by tightening screws (which provides the force to keep the valve closed), thus it is not capable of pumping operation. Further, the infrastructure of hosting the screws requires complex assembly and is time consuming. Combining all these inspirations, I developed a novel on-chip microvalve (and micropump) using rapid laser prototyping without the

need of complex fabrication and assembly. The novelty lies in the ease of fabrication and reconfiguration of this valve design to realize a hands-free fluidic handling platform for μTASs.

In this chapter, I present the details of my novel on-chip valve design by laser rapid prototyping for complete microfluidic manipulation: valving and pumping. By using a laser ablated polypropylene film and a CNC machined manifold with o-rings, the external pneumatic control is applied through the manifold by in-house air/vacuum supply. Four screws were used only to keep the manifold pressed against the membrane. Unlike other diaphragm valves, the membrane is simply aligned by a couple of alignment pins and seals to the valve structure by pushing the o-ring against the surface. No bonding of any sort is required. The reusable manifold eliminates the need to disconnect the external pneumatic lines. In addition, the single layer design of the valve allows fast rerouting of the microfluidics in several minutes. By utilizing these advanced features, an automated restriction fragment length polymorphism (RFLP) analysis has been demonstrated for HFE mutation detection. The microvalves allow the user to simply load and run with no other human input for a complete genetic diagnostic.

3.2 Laser Rapid Prototyping Valve Module

3.2.1 Novel Mono-layer Valve Design

As shown in Fig. 3.1, this novel mono-layer on-chip valve design consists of laser patterned 1.5 mm PMMA, a PP membrane, a bottom layer and a manifold. In addition, the pneumatic control module is connected to the manifold by Tygon tubes. Similar to our previous work [55], the pneumatic control is enclosed into a single module controlled by computer scripts. Other than the manifold, which is fabricated by a CNC machine, the rest of the valve is laser ablated by the Universal Laser System used in the previous chapter.

The mono-layer definition refers to the laser ablated PMMA layer. Even though the valve technically consist of four parts (manifold, membrane, PMMA layer and tape layer), the microfluidic structure is all laser ablated on the single layer. The manifold and membrane are both reusable, and the tape layer is only there to close the channel structure.

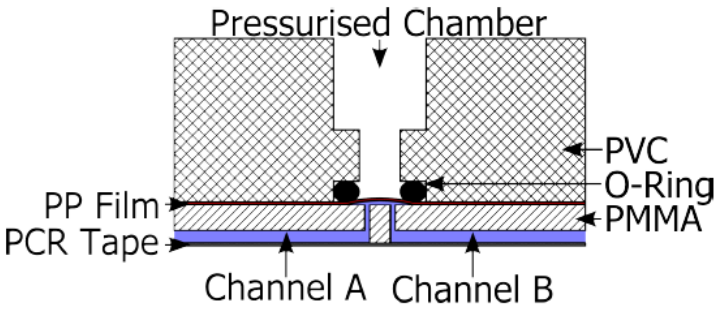

Figure 3.1: A schematic for the vertical membrane valve: Laser engraved trenches and applied tape form the channels at the bottom. Two channels are connected through laser drilled vias when the membrane is pulled up by vacuum. The valve is closed when positive air pressure is applied.

3.2.2 Standard Manifold Footprint

By using the standard footprint of the manifold, which is the only part requiring CNC machining, the estimated design-build time ranges from 2 hours for minor changes to 2 days for a complete redesign including the manifold. Since laser ablation is the only fabrication process for the chip, one can easily redesign the channel route and fabricate a new batch. This is significantly shorter than our glass based systems which in general require weeks to finish. Further, unlike the manually glued latex disc by [49] or the lithography patterned channel by [50], there is no manual alignment required for the assembly. By laser engraving alignment holes on the chip and PP membrane, they are aligned with $\pm$ 50 μm through alignment pin on the system. In addition, since the PP membrane is a non-sticky film different from Lounsbury et al. [54], a series of valves could be employed for peristaltic pumping operation. Therefore, this simple mono-layer valve module is a simple load-and-go system that has full fluid handling capability.

3.2.3 Valve Deflection

Membrane Deformation

As shown in Fig. 3.1, the membrane deflection, $w(r)$, could be calculated using the model of a circular, clamped diaphragm under uniform pressure give by [56, 57]:

$$w(r) = \frac{3P(r_v)^4(1-\nu^2)}{16Y_M t^3}(1-(\frac{r}{r_v})^2)^2 \tag{3.1}$$

where r is a radius of the membrane, ν is the Poisson ratio of the material, P is the applied pressure (Pa), r_v is the valve membrane radius (m), Y_M is the Young's Modulus (Pa) and t is the thickness (m).

The maximum stress experienced by the membrane is also given by Blake [56] as shown in Eq. 3.2. This value must be kept under the tear strength of the material in order to prevent the valve membrane from bursting. By rearranging the equation, one can find the maximum allowed pressure for a membrane as shown in Eq. 3.3.

$$\sigma_{max} = \frac{3P{r_v}^2}{4t^2} \tag{3.2}$$

$$P_{max} = \frac{4t^2\sigma_{max}}{3{r_v}^2} \tag{3.3}$$

By integrating the volume under the membrane, the volume displacement, $V_{membrane}$, in the valve caused by the membrane deflection can be easily estimated by Eq. 3.5.

$$V_{membrane} = \int_0^{r_0}\int_0^{2\pi} \frac{3P(r_v)^4(1-\nu^2)}{16Y_M t^3}(1-(\frac{r}{r_v})^2)^2 d\theta r dr \tag{3.4}$$

$$V_{membrane} = \frac{\pi P(r_v)^6(1-\nu^2)}{16Y_M t^3} \tag{3.5}$$

For these above calculations, the property values of polypropylene (PP) used are listed in Table 3.1. The valve radius, r_v, is defined by the size of the small o-ring as 1.25×10^{-3} m. In order to the keep the stress below the tear strength, the maximum pressure, P_{max}, is calculated to be 54.6 KPa. Thus, the maximum membrane deflection, $w_{r=0}$, is calculated to be 164 μm. The volume change, $V_{membrane}$, is 0.269 μL.

Material	Thickness (μm)	Young's Modulus (GPa)	Poisson Ratio	Tear Strength (MPa)
PP	40	2	0.4	40

Table 3.1: Polypropylene materials properties [58, 59]

Material	Type	Power (%)	Speed (%)	PPI	Z-axis (mm)	# of Passes
PMMA	vector cut	20	5	1000	1.5	1
PMMA	channel engrave	18	25	1000	1.5	2
PMMA	vias	18	25	1000	1.5	10
PCR tape	vector cut	5	10	1000	0.1	1
PP	membrane cut	5.1	25	300	0.1	1

Table 3.2: Laser ablation setting for microfluidic chips with integrated valves. The low power multiple passes cutting parameter is the key for generating small vias through 1.5 mm PMMA sheet. These cutting parameters have been optimized for best valving performance and reproducibility.

3.2.4 Materials And Fabrication

Materials

The PCR tape (part# AB-1170) is ordered through Fisher Sci. It is designed for qPCR application and has great optical transparency. The 40 μm thickness PP membrane is from Staples Canada (Part #10524). The pressure chambers in the manifold are made with 1.5 mm radius o-rings (McMaster Carr, 9263K545). The PVC manifold is a custom part machined by a CNC milling machine.

Fabrication

Similar to CE laser engraving, the PMMA, PCR tape and PP sheet are laser patterned in the laser with the parameters listed in Table 3.2. After laser ablation, PMMA chips are annealed for 1 hour at 80 °C and then optically inspected for closed vias and channels. Prior to the chip assembly, all substrates are cleaned with a deionized water dampened Clean-room wipe. Then, the PCR tape layer is laminated to the bottom of the chip. The pneumatic control pressures are down-regulated to -11/+20 psi from the in-house air/vacuum supply.

3.2.5 Results

Preliminary Test With The Early Tape-based Design

In an early attempt towards an integrated PCR-CE chip as in Chapter 5, the microfluidic channels and PCR chambers were fabricated by stacking layers of PCR tapes. However,

there are a few problems with this design. First, the PCR tape cannot be ablated as well as the PMMA. The laser cannot cut the adhesive and leaves sticky residues along the channel. Thus, the channel had to be at least 400 μm wide in order to manually remove the adhesive residue by a pair of sharp-tip tweezers. Second, the adhesive and the tape surface are hydrophobic. Thus, the chip has to be primed with deionized water before use. Third, vapor lock, a combined result of the wide channel and the hydrophobic surface, in the channel caused erratic behavior. Even with the priming process, there was still a high pumping failure rate. Therefore, this design was replaced with the current PMMA based design.

Despite the high failure rate, this chip design had proved that the valve is capable of retaining water at PCR temperatures. Three test chips filled with water were placed on a hotplate with the valve closed and held at 94 °C for 1 hour. All of the three chips were able to keep the water content. Therefore, there is no leak at either the valve or the chip during the PCR process.

Pump Rate

From the experiment results, the pump rate was approximately 0.1 ± 0.01 $\mu L/cycle$. More than 30 runs were performed during the pumping and the RFLP experiments described in later section. All of these runs demonstrated successful fluid pumping. Therefore it is clear that this valving module is capable of automatic reagent transportation. In order to measure the actual pumping rate, a red food coloring solution was used. During each test, 3 μL of solution was loaded in each of the three bottom wells on a test chip as shown in Fig. 3.2. In order to empty each well, 30 pump cycles were required with an on/off switch time of 0.2 s, which was controlled by a computer script. Therefore, the pumping rate is calculated to be 0.1 ± 0.01 $\mu L/cycle$. By using the in-house air/vac supply, the pneumatic control pressure is down regulated to -11/+20 psi for on/off state. Even though the P_{max} was estimated to be 54.6 KPa in previous section, the membrane experienced no change after being applied with 80 KPa (-11 psi) pressure. Thus, the applied vacuum is regulated to the maximum available negative pressure, -80 KPa. The estimated volume per pump circle became, $V_{membrane} = 0.394$ μL. The estimated pump rate was four times higher than the actual rate. This is likely due to the lack of accurate mechanical properties for the PP film used and these actual mechanical properties could change dramatically based on the actual composition and molecular weight.

3.3 SP-CE Integration For Auto-RFLP

After demonstrating working pumping with this valve module, the valve design was used on a RFLP analysis chip for HFE exon 4 (C282Y) mutation detection. [60] In a RFLP process, the DNA sample is digested by restriction enzymes into restriction fragments. These fragments are then separated according to their length by CE. By examining the electropherogram, clinicians could easily diagnosis the presence of the targeted mutation. A lab-on-a-chip implementation of an RFLP system had been demonstrated previously in our lab by Footz et al. [60]. However, the system was not fully automated. The enzyme was manually loaded between the 1st and 2nd run. Thus the system still faces the problems of the conventional RFLP approach, being labor intensive and at higher risk for cross contamination.

By utilizing the valve presented in this chapter, a fully automated chip based RFLP analysis has been realized. In this new system, the operator only needs to load the sample, CE buffer and enzyme buffer into each designated well. Then, the sample loading and enzyme loading processes will be automatically performed by a computer program. The complete choreography of the RFLP process on the auto RFLP chips is shown in Fig. 3.2. For demonstration purpose, the injection and separation was performed on a commercial confocal electrophoresis system (Micralyne Microfluidic Toolkit or μTK).

Fig. 3.3 shows the electropherogram of testing our auto-RFLP system with the uTK. As clearly shown in the curves, a new peak appeared between the primer and product peak. This is consistent with the prediction. The digested 158 bp fragment, in the presence of SnaBI, would appear before the longer 436 bp C282Y PCR product.

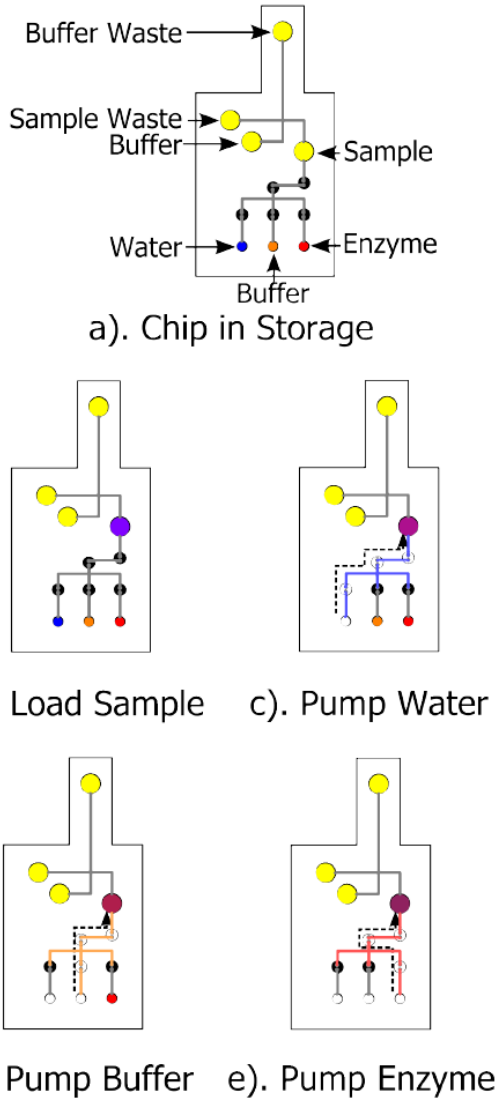

Figure 3.2: Choreography for the auto-RFLP process: the implementation of pumping realizes the complete hand-free operation of RFLP. a) A sample chip is first stored with buffer in the buffer waste (BW), sample waste (SW), buffer (B) and sample (S) wells. b) The S well buffer is then replaced with sample. The system automatically pumps water c) and buffer d) in to the sample well through peristaltic action using three valves. After mixing an inject-separate is done. e) The enzyme is mixed with the sample. After 10 minutes of digestion a second run is done.

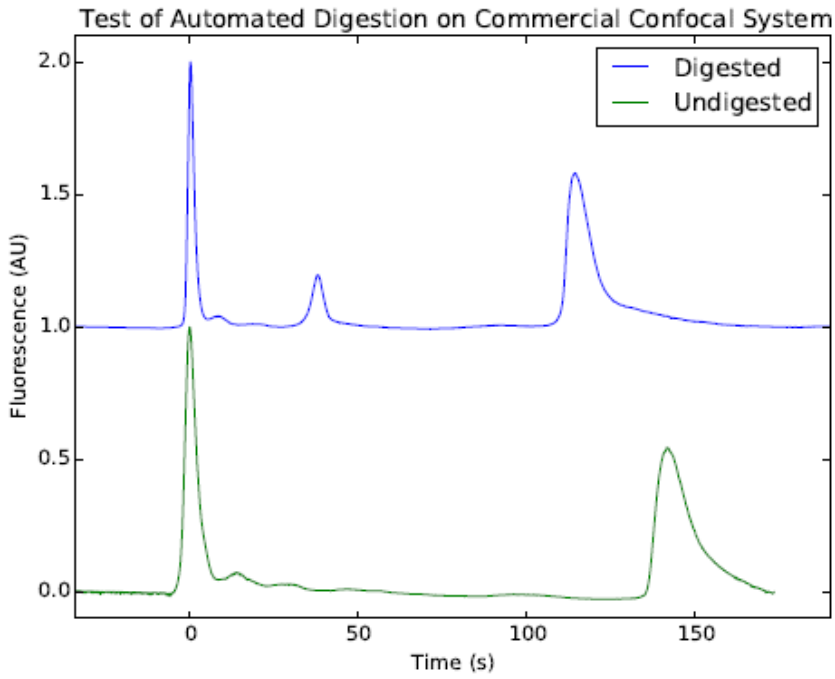

Figure 3.3: Demonstration of auto-RFLP on a commercial confocal system: The bottom is the electropherogram of the undigested PCR product; The top is the product after 10 minutes on-chip enzyme digestion at room temperature. An injection field of 43 V/cm and a separation field of 40 V/cm were applied. The detection point was 11 mm away from the intersection. After one inject and separation, the enzyme was pumped to the sample well and waited for 10 minutes at room temperature before the next injection and separation. It is clear to conclude that the micro valves and pumps have successfully mixed the enzyme with the sample.

3.4 Summary

In this chapter, a novel on-chip mono-layer valve design has been presented and fabrication protocol by laser ablation was developed. This design is capable of valving and pumping. By utilizing this valve, an automated electrophoresis diagnosis was successfully demonstrated in conjunction with a commercial confocal system. It had shown that a complete, well-established molecular biology protocol can be fully integrated using this valve design. It also enabled the continuing development towards a fully integrated PCR-CE rapid prototyping platform.

Chapter 4

CMOS Compatible Thermal PCR Module

All that is missing in order to implement PCR-CE on a single chip is a compatible temperature control module. A key challenge with such modules is to know the true temperature in the PCR chamber and this often leads to device-level calibration at the time of manufacture - a major impediment to manufacture. This makes the system not suitable for mass-production and less cost effective. Working with our collaborators at the University of Alberta (UofA), a novel silicon-based heater was developed and fabricated by them. The heater device was then integrated here into a PMMA helper-chip for testing of its performance. Although the heater did not meet the expected specifications and was not able to attain the temperatures needed for PCR, the design was shown to be insensitive to run-time variations and capable of being operated without device-level calibration at the time of manufacture. This work has led to a manuscript that is about to be submitted.

4.1 Introduction

Portable PCR based genetic diagnosis systems have been demonstrated in various places. There are commercially available portable systems such as the Miniopticon from Bio-Rad and the R.A.P.I.D system from BioFire. However, in general they are relatively large in size and similar or more expensive relative to current desktop qPCR systems. Various research groups have demonstrated compact on-chip systems such as the work by Lounsbury and Landers [61] and our previous TTK system [55]. However, both of these compact systems require device level calibration at or after the time of manufacture, a key challenge for future implementation. Thus after successfully demonstrating CE separation and integration on polymer chips, the next missing piece of this puzzle is a compatible PCR module. The review by Ahmad and Hashsham [10] of thermal systems for genetic analysis gives a good survey of past development. As noted by Ahmad and Hashsham [10], the verification of the real chamber temperature is a challenge, often calling for calibration runs or the use of sensors that perturb the temperature distribution. In 2008, our group had demonstrated a integrated PCR desktop system. [55] However, the extensive calibration required for precise temperature limited the system from further application. In 2013, I had an great opportunity to be involved in a CMOS based heater project, which was aiming at solving the problems and moving further.

In order to reduce the perturbation of the sensor on temperature uniformity, the heater is both the heating element and the sensing element. There are two major potential advancements: 1) no device level calibration; 2) uniform temperature distribution in the chamber. The sensing is relying on the temperature coefficient of electrical resistance (TCR) of the heater film, which is an easily calibrated parameter through the fabrication process. Due to the advanced quality control developed by the CMOS industry, sample device calibrations are expected at batch level only. Since no dedicated sensor is placed in the heater region, the temperature uniformity in the chamber is affected only by the heater design and boundary conditions.

For this work the heater chips were designed and fabricated by our collaborators. After receiving the fabricated chips, I developed a helper chip system to interface with the tiny Si chip which includes electrical, pneumatic and fluidic connections. However, due to fabrication defects, I had to change my plan from using the helper chip to a simple PCR tape solution. From these chips, I proved the concept of the dual purpose heater design for CMOS and demonstrated heater uniformity at 43 °C. However, without the helper chip system, I could not demonstrate the full PCR process due to air bubble formation at targeted temperatures (e.g., 55, 72 and 94 $^{\circ}C$). In addition, during the test I found the heater Al traces showed evidence of corrosion after testing, which led to electrical failure.

This is different from the previous work from our group by Martinez-Quijada et al. [62].

4.2 Why CMOS?

After learning the lesson from previous glass-based systems [55], which required extensive calibration, thin Al film on Silicon (CMOS-compatible) designs were selected as an alternative. The CMOS industry has developed a great level of process control for high precision and high quality. Thus, the batch level calibration can be expected for a CMOS based system. Further, a CMOS-compatible process also means an easy transition to mass production. Both of these are essential to the realization of a true integrated, low-cost and portable μTAS. The review by Saha and Chaudhuri [63] provides a good overview of the state of the art about CMOS/MEMS integration. However, due to the high non-recurring engineering cost, for the near term it is critical to develop and use these technologies in an intelligent packaging fashion, or "helper chip", which could in future be used for a complete CMOS-based PCR-CE system.

4.3 PCR-CE Integrated CMOS Plan: A Helper Chip System

Although micro-channels [29], micro-heaters [62], and all electronics can be integrated (including HV, detection and interface) [64, 65], the key challenge for CMOS is that there is not yet an available valve technology, which does not perturb the temperature uniformity of current heater design. Hence in this work, the design is tested along with PMMA-based valving system. Based on the skills and experience that I developed with the laser fabrication of CE and valve modules, I developed a helper chip which is constructed of multiple layers of laser patterned PMMA and double-sided tapes. As shown in Fig. 4.1, the helper chip is an integrated system consisting of electrical connection, pneumatic controlled valve, fluid connection and optical illumination/detection and is directly coupled to the CMOS chip in order to form a fully functional devices.

4.4 CMOS PCR Module Design

The CMOS PCR module consists of a Si heater die with a helper chip with polymer microfluidic layers and a polymer membrane. The polymer microfluidic layers are made

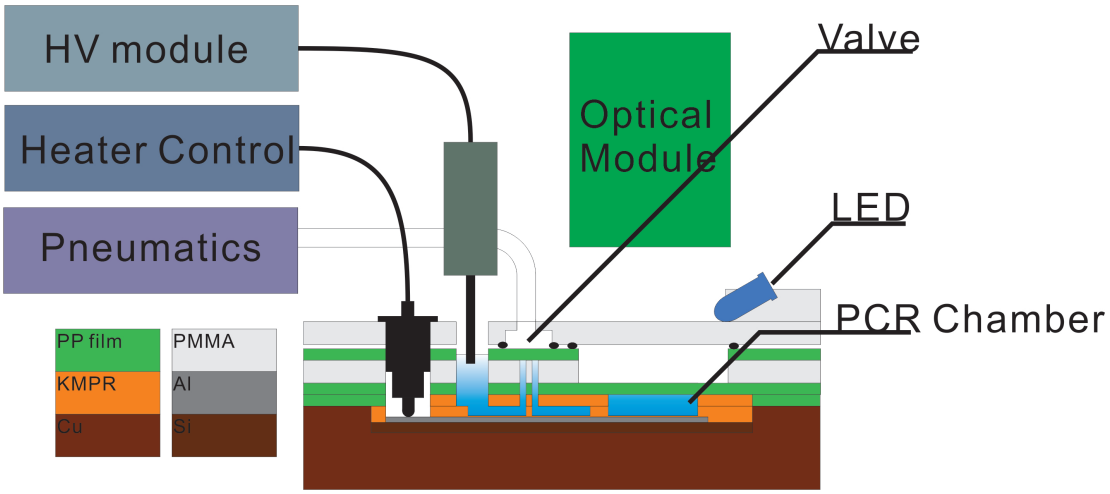

Figure 4.1: A schematic diagram of the intelligent packaging showing functions of: valving, thermal control and interface. Valving is done by deforming a membrane through external pneumatic control modules. The thermal circuit is connected through pogo-pins on exposed Al pad. The HV module is connected by inserting Ni electrodes into the open reservoirs, which is connected to the CE parts of the UofA chip. The Cu plate at the bottom is a heat-sink for rapid cooling of the chamber.

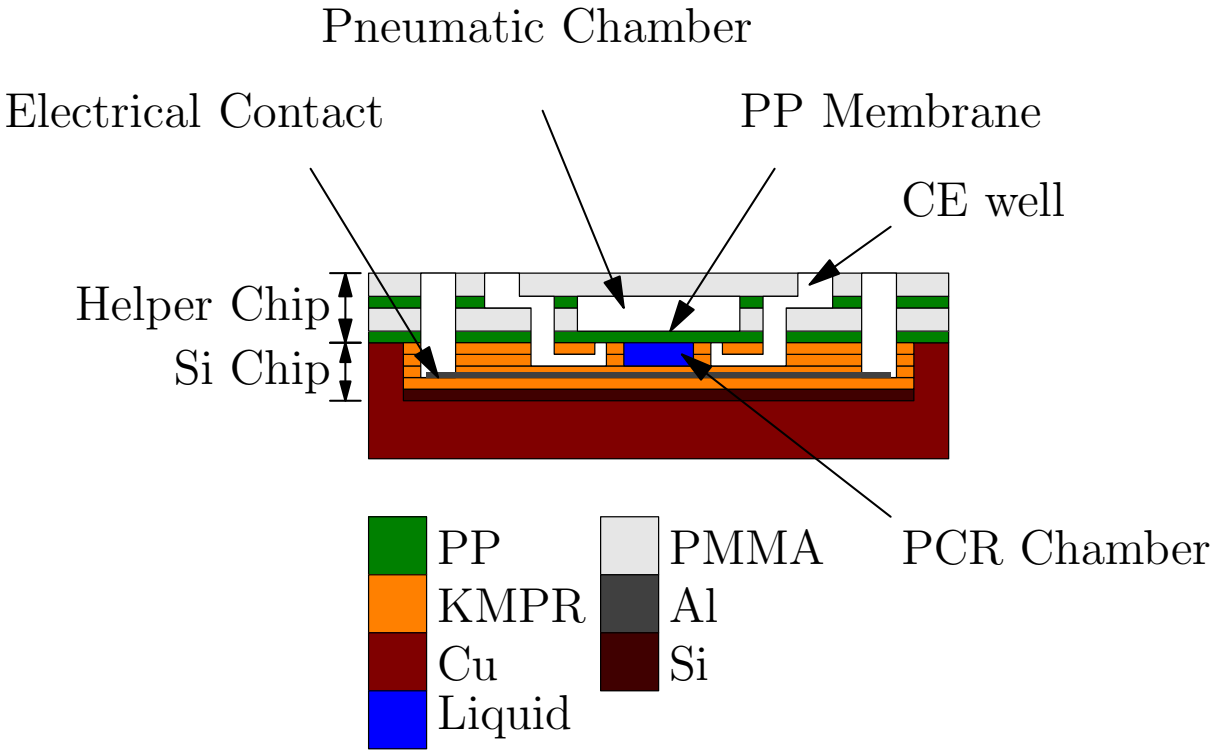

Figure 4.2: A zoom in cross-section view of the PMMA-Si helper chip design above the heater chip region. (The drawing is not to scale.)

of KMPR, which is a photo-resist material readily available for microfluidic application. KMPR is similar to SU-8, and its thermal and mechanical properties has explored previous by our group. [66] Fig. 4.3 shows the cross-section and top view of the chip. In this module, the heater structure consists of a Si base, an aluminum film heater deposited on KMPR and three layers of KMPR fluidic structure atop. The aluminum heater was built upon the base KMPR layer through lithography and etching as described in reference [62]. The top three KMPR layers support a variety of microfluidics functions and are transfer bonded to the heater layer as demonstrated previously. [15]. The thickness of each layer is from the top to bottom as shown in Fig.4.3a, 40 μm (PP), 25 μm, 20 μm, 20 μm, 20 μm and 500 μm (Si). The thickness of the Al film is designed to be 100 nm.

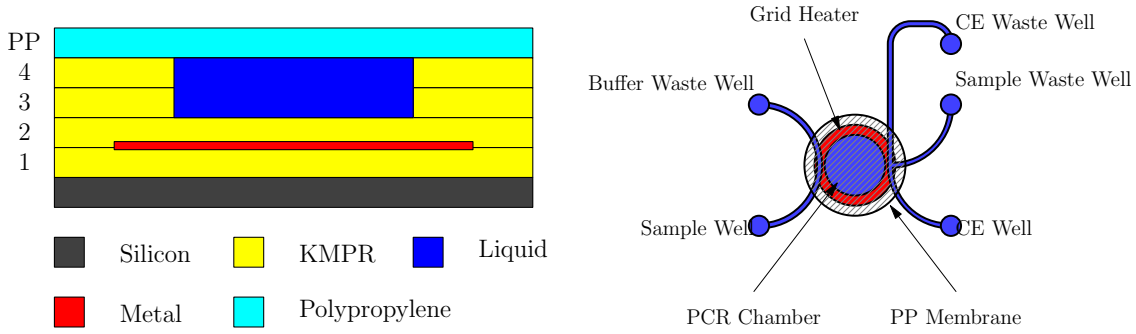

(a) A: Cross-section view

(b) B:Topview

Figure 4.3: Drawing for the UofA Si heater chip: A. Cross-section drawing for the heater stack of CMOS heater atop the Si substrate; B. Top-view drawing of the proposed CMOS stack heater design showing the PCR chamber (center well). The wells, channels and vias are parts of the fluidic system that is intended to fill the chamber and to perform capillary electrophoresis. The fluidic parts are the same ones covered in Chapter 3

As shown in Fig. 4.3b, the heater is only extended enough beyond the chamber to ensure uniformity inside the chamber region in order to conserve power. Since thermal transport is a diffusive process, we estimate that this distance should be at least twice the thickness of the polymer stack (which is 125 μm in total). We would expect that edge effect can be neglected as long as the heater extends beyond the chamber by 250 μm or more. Most of the temperature change will occur within a range of about 125 μm at the outermost edge of the heater. However, this is a rather crude approximation. Since the design of this heater chip was developed by my colleagues at the UofA, the detailed verification can be found in Dr. Martinez-Quijada's thesis [67]. In the heater design, the chamber radius is set to be 1200 μm. The heater grid is thus 350 μm further from the edge of the chamber.

4.5 Thermal Robustness

As mentioned in the introduction, the device level calibration and uniformity are the two biggest concerns for any PCR heating system. By properly designing the heater, the chamber temperature uniformity could be achieved. However, the first concern has only got a partial solution. By utilizing CMOS, we get a trustworthy set of specifications from the manufacturer by fine process control. In addition, we need a system that is not dependent on varying external environments. This is what we refer to as the thermal robustness of a thermal system. In this section, the robustness of the Si based heater design is discussed with a simple 1D resistive divider model.

Rather than deal with the bulk structure of the thermal system, it is common to describe such a system in terms of electrical equivalent network circuits. There is an analogy to be drawn between the voltage difference, current, electrical resistance and capacitance and the temperature difference, heat flow, thermal resistance and thermal capacitance. [68, 69] Eq. 4.1 are used to calculate the approximate value for each components in the resistive divider network as shown in Fig. 4.4. In the lateral direction, a very thin, low-conductivity structure can dramatically increase the lateral resistance and reducing the horizontal heat flow. So, the heat flow is constrained to flow vertically, which results in a one-dimensional system. Therefore, we can make a 1D approximate of our PCR module.

$$R_V = \frac{d}{kA} \tag{4.1a}$$

$$R_L = \frac{1}{2\pi kd} \ln \frac{r_2}{r_1} \tag{4.1b}$$

$$R_H = \frac{1}{h_c \cdot A} \tag{4.1c}$$

Where thickness d (m), thermal conductivity k ($\frac{W}{m \cdot K}$), area A (m^2), outer radius r_2 (m), inner radius r_1 (m), natural convective heater transfer coefficient $h_c = 5.6\ \frac{W}{m^2 \cdot K}$.

By applying the proper thermal properties of each material, one can find the thermal resistance of each layer as listed in Table 4.1. The total vertical resistance above the heater is $\approx 23.7 \times 10^3\ \frac{K}{W}$. The resistance below the heater is 14.3 $\frac{K}{W}$. So, the heat flow through the top is about 0.006 % of the heater flow to the bottom. Therefore, the heater is insensitive to the external environment atop the PCR module; the loss by conduction is dominant such that even a large change in the h_c value does not affect the result significantly. In addition, by applying a voltage divider equation to the circuit above the heater, the temperature

difference between chamber bottom and heater, $Th - Tc_b$, is proportional to product of the resistance ratio, $\frac{R_2}{R_{top-total}} \approx 0.0006$, and the temperature difference between heater and the room temperature, 73 °C. Similarly, the temperature at the top of the heater is also very close to the heater. Therefore, we can approximate the chamber temperature by the heater temperature, which is easier to measure.

Material	Conductivity $k(\frac{W}{m \cdot K})$	Thickness d (μm)	Resistance $R_V(\frac{K}{W})$
KMPR 1,2,3	0.2	20	13.9
KMPR 3	0.2	25	16.5
PP membrane	0.22	40	26.5
Water	0.67	45	8.9
Si	163	500	0.40
Al	237	0.1	≈ 0
Convection			23628
Lateral			387

Table 4.1: Thermal resistances for a 1550 um heater operating at 95 °C. [58]

4.6 Initial Specification Of The Si Heater

In order to realize this PCR system, I developed a list of design requirements by working together with our partner at the UofA. Each of the design requirements is carefully determined. (e.g., fabrication tolerance, resistance, circuit design). However, there were a few unexpected changes when the chips were received. This section describes the specification agreed upon by both groups. Later, in the result section I will discuss the actual values for these parameters.

The key design requirements are listed below:

- Reliable electrical connection. Each connection should last for 2 hours or more.
- The silicon die outer dimensions are 11.91 mm x 8.93 mm as specified. The chip bottom is 1.28 mm away from the nearest electrical pad. The left and right edges are 20 μm away from the nearest electrical pads. All dimensions are specified with a tolerance of ± 40 μm.

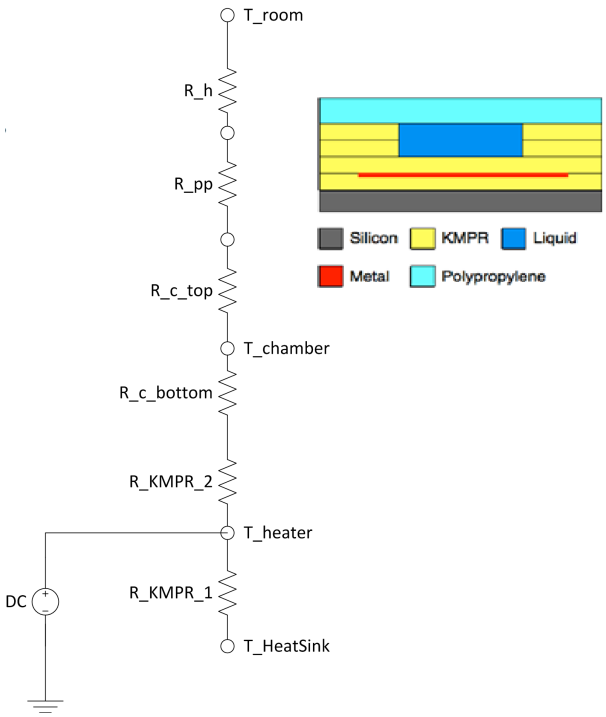

Figure 4.4: A thermally resistive divider presentation of the stack heater: the heater flow is dominant in the vertical direction

- Ideally the heater resistance should be above 50 Ω at 95 °C, but it cannot be lower than 25 Ω at 95 °C.
- Open channels and vias.

First of all, a reliable electrical connection is the key to operating the heater through the helper chip design. The 2 hours requirement is based on the time it takes for a regular PCR to finish. As shown in Fig. 4.1, the original design has a push-down pogo-pin on the Al pad to form the electrical connection to the heater. However, the electrical connection failed quickly upon applying electrical power as tested by the UofA. As an alternative solution, the UofA suggested using a heat-cured conductive epoxy (part #8331-14G, MG Chemicals) to permanently bond a wire to the contact pads. From their test, the epoxy significantly increased the lifetime of the connection up to several hours.

Secondly, in order to align the KMPR microfluidic structure to the fluidic ports of the heater chip, a recess is precision-milled into the Cu heater sink for tight alignment. By

having a close fit between the recess and the chip, we can expect an easily aligned system. As specified by the UofA, the dicing saw would cut the chip to a size of 11.91 mm x 8.93 mm (L x W) with a tolerance of ± 20 μm per cut. Based on this, my colleague, Nemanja Kliska, had developed a machining protocol to make a recess that was milled to be 11.92 mm x 8.94 mm ±25 μm.

Thirdly, the maximum voltage supply is 10 V or less, and current should be ideally below 200 mA but no more than 400 mA. The 10 V is the maximum vlotage that a LabJack U6 could handle. The 200 mA is the maximum current output for a single LT3092 current source. However, according the application note provided, two of them could be connected in parallel for more power. Thus, the power maximum density is 2 W/7.55 mm^2 (171 W/in^2) or 4 W/7.55 mm^2 (342 W/in^2) for single or double current sources. Thus, by using Ohm's law the heater resistance should be at least above 25 Ω in order to keep the current under 400 mA.

Finally, in order to transport fluid, the microfluidic structures such as channels and vias need to be open and not leaking. Proper bonding of the KMPR layers is essential to the success of this system.

4.7 Methods And Material

4.7.1 Determination Of Chamber Temperature From TCR

Heater temperatures can be estimated from the resistance change of the heater. Following Eq. 4.2 where α is the TCR, R_{h0} and R_h are heater resistance at room temperature and sampling temperature respectively, the heater temperature can be found during the heating process. Since one can easily prove the chamber temperature, T_C, is approximately equal to T_h due to close proximity, the chamber temperature can be estimated from the TCR and heater resistance.

$$T_h = \frac{R_h - R_{h0}}{\alpha R_{h0}} + T_{room} \tag{4.2}$$

However, since the heater is larger than the chamber area as required for a uniform chamber temperature, there needs to be a small correction factor. From the design work done by my colleague, Dr. Jose Martinez-Quijada, a small correction factor is applied to the original equation as shown in Eq. 4.3. The ϵ is accounting for the fact that a small portion of the heater (mostly outside the chamber edge) is not at uniform temperature due

to edge effects. We refer to $\epsilon\alpha$ as being the effective TCR of the heater in the system. As described in previous section, the polymer stack between the heater edge and the chamber edge is more susceptible to the edge effect. For a rough approximation, one can take the heater radius minus half the polymer stack thickness, 65 μm, to be the boundary for the uniform temperature region. So, one can estimate $\epsilon_{estimated}$ would be 0.92; a more accurate estimate is found from a 3D simulation by Dr. Jose Martinez-Quijada. The simulated $\epsilon_{simulated}$ valve is found to be 0.96.

In summary, Jose and I have analyzed the Si heater system based on a 1D resistive divider model and the 3D simulation. Since, the correction factor, ϵ, is small and close to 1 and can be determined quite accurately, we conclude that the chamber temperature can be found from the heater resistance change based on the TCR as in Eq. 4.3.

$$T_h = \frac{R_h - R_{h0}}{\epsilon\alpha R_{h0}} + T_{room} \tag{4.3}$$

4.7.2 TCR Measurements

From the earlier testing results, the heater had a time varying resistance which seemed to be due to electromigration, especially near the contact pads. Therefore, the TCR measurements were made in two different ways: a standard 4-point method and a non-four-point method.

The standard four-point method eliminates the uncertainty caused by the resistance in series with the load (ie. the contact resistance at the contact pad). Since the contact resistance could change during the test as suggested by the early tests, a non-four-point method was used at the University of Waterloo (UofW). The second approach can determine the heater resistance without constantly apply any current.

Four-point measurement of TCR

After fabrication, the TCR of the heater film were measured at the UofA. The chips were placed atop an aluminum heat-sink which was in good contact to a hotplate (Echotherm TM HS40, Torrey Pines Scientific). Spring loaded pogo-pins were placed on a PMMA holder and were used to contact the heater without scratching the contact pads on the chip. The Al heat-sink and the chip were heated by the hotplate with a temperature accuracy of less than 1 °C. A multimeter (HP-34401A, Hewlett Packard) were used to measure the resistance in 4-point mode as described by Martinez-Quijada et al. [62]

Non-four point measurement of TCR

The TCR of the heater film was also measured on a chip from the same fabrication batch at the UofW. The resistance between each possible pair of contact pads was measured at each of set temperatures while the whole assembly was heated inside a convection oven(model #6916, Fisher Scientific). By solving the resulting system of equations, the heater and the contact resistances at each pad were calculated. In order to minimize thermal variation due to air flow, the heater chip was placed in a metal box with the lid closed. A thermometer was used to monitor the temperature inside the box within 0.5 °C. The 4 wires were attached to the chip using a low-melting-point solder (ROTO 144F, RotoMetal Inc). A digital multimeter (U1252A, Agilent) was used to measure each resistance with a repeatability of 0.01 Ω. The oven temperature ramped from 30 to 90 degrees with 10 degree increments. While taking the measurement, the oven was brought to equilibrium by waiting for 1 hour after reaching the target temperature.

4.7.3 Heater Control

A custom designed linear voltage-current convertor was used to drive the heater. A USB-based data acquisition device (U6, LabJack) was used to drive the convertor and collect data. A Python script running from a windows computer was used to control the U6. The current gradually increased to a preset level and was held there for 200 s. The LabJack U6 collected the current and voltage readings during the entire run. The resistance could be determined within 0.004 Ω.

4.7.4 Determination of Temperature From Temperature-dependent Fluorescence

The fluorescence of Rhodamine-B (RhB) is temperature dependent and can be used as a non-invasive temperature measurement as in Ross et al. [70]. However, since the fluorescence is protocol-dependent, RhB was first calibrated in our lab. My colleague, Gordon Hall, performed the calibration in this section.

The RhB powder (part # 83689, laser grade, Sigma Aldrich) was dissolved to make 1 mM concentration solution with MilliQ water through a series dilution and stored in the Al foil covered 10 mL conical tube. 20 μL of 1 mM RhB solution and 40 μL of 5x TBE buffer was diluted together with 140 uL MilliQ water to 100 μM RhB working concentration in 1x TBE buffer. An optical spectrometer (USB-4000, OceanOptics) was used with a cuvette

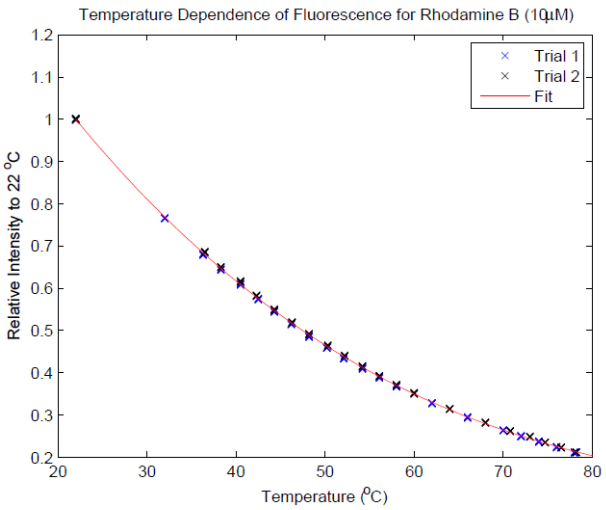

Figure 4.5: Rhodamine-B (RhB) calibration curve: relative fluorescence vs temperature. By fitting a third order polynomial as by Ross et al. [70], the characteristic equation was found to be $T = 132 - 250I + 220I^2 - 79I^3$. This calibration was performed by Gordon Hall in October 2012.

holder, which was placed inside a Styrofoam box and heated with a circulating water bath (Model S-1, MGW Lauda). A thermometer was placed against the holder and immersed in thermal paste (part #10004, Cortec Spray Technology) for good thermal contact. 1 mL of the 100 μm RhB solution was loaded into an acrylic cuvette, and then placed in the holder inside the box. The water temperature was increased from 30 °C to 78 °C with 2 °C steps. In order to fully equilibration the system, it was held at each temperature for 2 hours before taking each measurement. In order to minimize photobleaching effects, the LED illumination was only turned on before taking the measurements.

By fitting the data with a third order polynomial as described by Ross et al. [70], the equation was found to be:

$$T = 132 - 250I + 220I^2 - 79I^3 \tag{4.4}$$

where T is the temperature and I is the fluorescence intensity normalized to the value at 22 °C. Therefore, the temperature could be found by comparing the RhB fluorescence intensity to the intensity at room temperature (22 °C).

4.7.5 Optical Determination Of Chamber Temperature

In order to optically determine the chamber temperature, the 100 μM RhB solution was loaded into the chamber to represent the PCR brew. A microscope (Micromaster by Fisher Sci.) was modified to be used as a fluorescent microscope. A proprietary absorbing color filter (cutoff wavelength$\approx$ 560 nm) from Teledyne-DALSA was placed in the center column after the objective lens. A CCD camera (part # MU900, Amscope) with a C-mount relay lens was held by the eyepiece holder to capture the real-time image of the chamber during heating. A Kingbright LED (part# WP710A10QCB/G, Digikey) was used as the excitation light source. It was attached to a PMMA plate with 60 degree angle for alignment and better illumination. By using provided software (Toupview), a steady stream (1 frame each 2 s) of jpeg images was acquired under a fixed set of conditions. (Please see appendix for detailed setting.) For synchronization, the image acquisition started 30 s (15 frames) before turning on the heater current program. The collected images were then processed by ImageJ. [71]. In order to determine the chamber temperature, a average intensity of each image were measured using the ImageJ measurement tool. A center circle of 200 μm radius was selected for the averaging. The relative intensity to the room temperature was then calculated. By fitting the relative intensity to Eq. 4.4, the average chamber temperature was found and plotted as in Fig. 4.8.

The LED was turned on for the entire duration of the heating program and kept running for another 60 s (30 frames) after turning off the heater. The long duration was used to capture the cooling rate of the heater. However, this leads to a large impact on the signal due to photobleaching. To correct for photobleaching, a chip loaded with fresh RhB was placed under the microscope with the LED turn on for 30 minutes. The same image acquisition was performed, but no electrical connection was made. By processing the images, the photobleaching-caused fluorescence decay rate was obtained, which was 0.9 % per 100 seconds.

In addition, two other CCD sensors, the EMCCD senor and the Meade DeepSkyImager, were tested for the signal detection. Both of the CCD sensors are designed for low-light-condition applications. The EMCCD sensor amplifies the signal by providing a higher gain. The Meade camera allows longer integration time for signal amplification. Since the EMCCD sensor was not supported by the manufacturer, a third-party frame capture hardware and software had to be used. Despite the difficulty of setting up the EMCCD sensor, its imaging performance was found similar to the Amscope camera. For the Meade sensor, the integration time required for get a image of similar intensity was about 1000 ms, which is 10 times longer than the Amscope camera. Therefore, the Amscope camera was used.

4.8 Results

4.8.1 Heater TCR Verification

As provided by the UofA, the Al thickness was measured to be 150 ±10 nm. Using the standard 4-point measurement method, my colleagues at the UofA took two chips from the same fabrication batch and measured the TCR: $2.07 \pm 0.019 \times 10^{-3}$ 1/K. Chips from the same batch were measured at the UofW with the non-4-point method. The TCR measurements were consistent with the ones obtained from 4-point method and showed a TCR of $2.06 \pm 0.05 \times 10^{-3}$ 1/K.

4.8.2 Si Heater Specification Verification

Electrical Contact On Al Layer

As described in Section 4.6, the conductive epoxy seemed to be a promising alternative to the pogo-pin design, however the connections were not reliable and difficult to work with. First, the provided epoxy protocol did not consider the presence of the polymer helper chip atop the Al contact pad. Since the original design was intended for the small pogo-pin, there was very limited space for electrical contacts. Even though electrical connection can be made by carefully filling the pogo-pin recess with the epoxy, the suggested heat cure process was the next problem. After curing the epoxy, the electrical connection presented earlier became open circuit. Fortunately, the heater chip turned out undamaged after disassembling the helper chip. Thus, by a couple additional tests, the cause of the electrical failure was the thermal expansion mismatch between the silicon and the helper chip at the curing temperature. As a result, the epoxy was cured at room temperature for 12 hours even though it is not recommended by the manufacturer. However, the electrical connection turned out to be unreliable with applied current. During the preliminary electrical test at the UofW, about 50 % of the chip epoxy connections experienced electrical failure upon applying a current of around 200 mA for 5 minutes. After two of the chips failed, I started to test the connection on Al foil instead. Short wires were glued to a freshly polished Al foil surface. The resistance between wires was measured to verify proper electrical connection. Then a 400 mA current was passed through each pair of wires for 30 minutes or until electrical failure. By calculating the failure rate, my experiments show that one out of every three epoxy connections would fail within 30 minutes. After subsequent meetings with the UofA, they revealed that they had a similar 30 % failure rate. Since both groups

showed a similar failure rate, it seems unwise to run a chip that requires four electrical connects.

The final solution was the use of a low melting point solder, Field's metal, which can provide a stable electrical contact at high current. Since the microfluidics on the Si chip were not functional (see the section below), the helper chip was replaced with a small piece of PCR tape. Thus, the electrical wires were directly soldered to the Al pads using the Field's metal to form the electrical connections.

Si Chip Dimensions

The dimensions of the as-delivered Si heater chip were out of the specified tolerance. The received chip dimensions ranged from 11.95 mm to 12.32 mm in length and from 8.98 mm to 9.40 mm in width. All of them were out of specification, and none of them could fit into the recess. Precision machining of an assembly to fit each (differently-sized) silicon chip was not feasible (weeks per assembly). As a stopgap measure, an oversized recess in Cu was made.

Heater Electrical Resistance And Power

After receiving the heater chip, the resistances were measured and ranged from 25 to 28 Ω which just met the minimum requirement. However, according to the later verified simulation, the heater design required a power density of 4.5 W/7.55 mm^2 to reach 95 °C, which was larger than the maximum power available for two LT3092 current source. In order to achieve 95 °C on these heaters, the current was boosted up to 450 mA and the maximum voltage was changed to 20 V. The consequence was a redesign of the electrical measurement circuit. In order to achieve higher current, three LT3092 units were connected in parallel.

Microfluidic Structure

The most significant problem was the closure of the microfluidic structure. In order to make use of the microfluidics on the multilayer KMPR structure, the fundamental requirement is open channels and vias. Since the channels in KMPR layers are only 100 μm in width, the fiber and particulates in the air could cause the blockage in the channels. From the past experience with glass chips, the fluid drying process tends to draw fiber and dirt into

the channel and causes irreversible blockage. Thus we kept the chips sealed in a clean gel box and only opened the seal before assembling the helper chip system.

Before going into the details, it is important to have a brief idea about the chip conditions for various batches. Table 4.2 summarized the details and comments provided by the UofA. It was clear that the batch #2 was the only batch of chips that had proper heater and microfluidic structures. Batch #4 was requested after the closed channel issue was discovered for the second batch. However, the fourth batch arrived after we decided to use tape instead of the helper chip. Further, the fourth batch experienced the same moisture problem as other batches during the water bath test as described in Section 4.8.5. Therefore, the batch #2 was the only batch tested with the helper chip design.

Batch #	Arrival Time	Number of Chips	Comments
1	Dec 2012	3	There were defects in the metal layer.
2	Dec 2012, March 2013	4, 2	Good chips with proper metal.
3	June 2013	4	Delamination issue with the bonding. Leaking may prove to be an issue with the chips
4	Aug 2013	10	Supposedly good chips with open channel and ok bonding. Minor delamination occurred at the non-critical region (e.g., the chip edge, near the Al contact pad)

Table 4.2: Summary of different Si heater batches. The number of chips is only for the U1550 type chips, since other heater design were not used for this project. Batch #2 was shipped to us in two shipments. The first three batches were not useable due to malfunctioning microfluidics and delamination. The 4th batch was the only good batch, but it still has the moisture problem of the 2nd batch and did not meet the sizing requirements.

Before the helper chip system assembly, all Si heater chips were inspected under the stereo microscope as shown in Fig. 4.6. From the images, it was clear that all the microfluidic features were present in the KMPR layers. The higher magnification Micromaster microscope was used in an attempt of achieving better details. However, the opaque silicon prevents the use of the bottom illumination, and the short focus distance of the objective

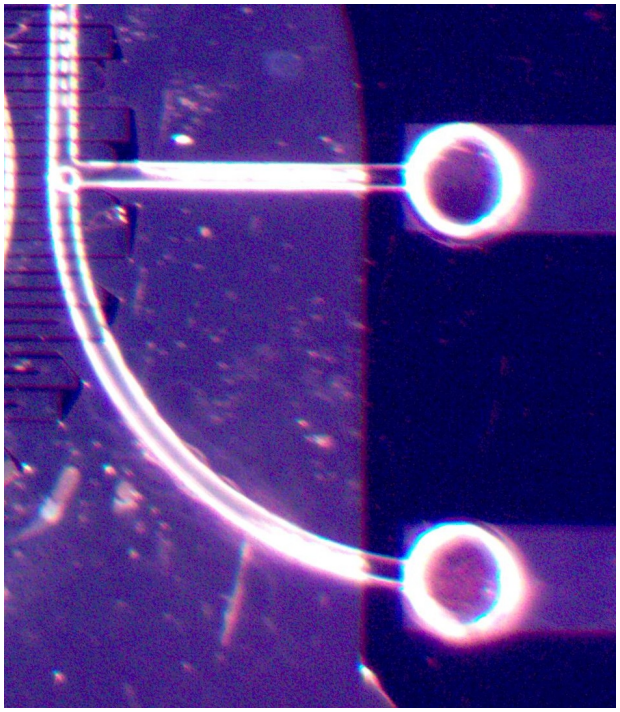

Figure 4.6: Amscope Camera Image of the Si heater chip during the chip inspection. The channel, via and wells are clearly shown in the picture. The light colored area has Al layer under the KMPR. In order to take this image, a 2X magnification lens was attached.

lens projects a shadow on the chip. Since all the features were presented and properly aligned, we proceeded with the helper chip assembly.

However, during this initial test, one of the two channels on the tested chip did not fill with water. Even using a syringe to fill the chip with pressurized deionized water, there was no water filled into the channel. Instead, the pressured water went through the space between the PP membrane and KMPR layer and leaked into the chamber and outside.

At first glance, the problem was thought to be a clogged channel caused by fibers since the test was not performed in a cleanroom. After carefully dissembling the system, there was no clogging present on the Si chip and the microfluidics in the polymer helper chip tested open by flowing through deionized water. Then, the alignment issue due to out of specification chips was thought to be the problem. However, it was impossible to optically inspect the vias through 3 layers of different polymers of the helper chip. Thus, the only alternative, if microfluidics on the Si chip were functional, is that the alignment was suspect.

In order to verify the functionality of the KMPR microfluidics, a small drop of deionized water was loaded on to the wells. The water did not fill in the channel which was different from our previous work. [62] The contact angle of the KMPR was about 90 degree with deionized water. Then 2 μL of ethanol was loaded at the vias and inspected under microscope. The ethanol quickly vaporized and did not fill into the channel. Same tests were performed at the loading wells. One of the channels did not fill with ethanol. A total of 3 chips were tested similarly, and all of the chips had at least one of the two channels that was not filled with ethanol. (4 out of 6 tested channels were failed.) After several weeks of conversations with our partners at the UofA, it was revealed that the KMPR layers of the second batch were over dosed with UV light during the fabrication. This could explain why the contact angle changed from 60 degrees to 90 degrees. The chips from the same batch were inspected with SEM at the UofA (Fig. 4.7) and it is clear from the SEM images that some of the channels and vias were closed right after fabrication.

Since the 3rd batch had shown signs of poor bonding during fabrication, the possibility of having functional KMPR fluidics was very small. Since another batch of fabrication had not been planned for this project yet, the arrival time of a new batch was unclear. In addition, the whole fabrication process, from laser ablation to the final assembly, took about 10 days. It was not feasible to continue with this approach and a fallback plan was developed. Since the KMPR microfluidics was not functional, the helper chip was replaced with a single layer of PCR tape in order to cover the channel.

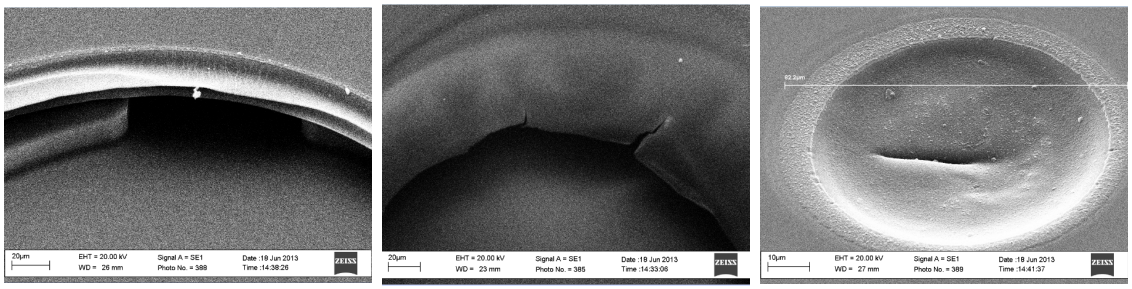

(a) Channel Open (b) Channel Closed (c) Via Closed

Figure 4.7: SEM images of the UofA heater chip: a) the channel is open; b) The top KMPR layer collapsed and bonded in front of the channel; c)The edge of the via collapsed and bonded to the channel bottom layer. From the UofW testing, the statistics shows a rough 60 % failure rate for each channel. Thus, due to the limited number of the available chips, it was not feasible to continue with the helper chip approach unless this problem is fixed by the UofA. The SEM image was provided by Matthew Reynolds on 18 June 2013.

4.8.3 Optical And Electrical Temperature Measurements

Repeatable runs at temperatures less than 45 °C had shown excellent temperature agreement between optical and electrical measurements. Fig. 4.8 shows an example run at 43 °C. The two traces, blue and green, showed the chamber temperature determined by TCR and fluorescence respectively. The blue trace was calculated using the resistance measurements collected during the experiment. The resistance change was converted to temperature change using the TCR value. Then the absolute temperature was obtained by adding the temperature change to the room temperature measured by a thermometer. The green trace was calculated by using the optical method described in Section 4.7.5. In order to synchronize the two traces, the optical data collection was started 30 seconds earlier with a frame rate of 2 seconds/frame. The two traces thus differed no more than 2 seconds in time after removing the first 15 frames from the optical detection.

The two traces agree with each other within 0.3 °C, which is well below the 1 °C requirement. Although the current was held constant after reaching the target setting (250 mA), the heater temperature increased gradually with time. I noticed the heat-sink was slowly warming up during the testing process and reached approximately 35 °C. This explains the continuing increase in chamber and heater temperature during the test process. This phenomenon is unexpected from the 3D simulation at the UofA, which assumes that the heat-sink was a perfect heat absorber at room temperature. However, this gradual increase is not a problem once we incorporate a temperature controller. It will decrease the current based on the resistance change as the heat-sink warms up.

Unfortunately, the runs at higher chamber temperatures (from 45-70 °C) did not provide useful information. At higher temperatures, bubbles appeared in the chamber and expanded during heating process. This distorted the fluorescent intensity by varying the optical depth of the RhB solution film in the chamber. In addition, the air bubbles formed hotspots due to the low thermal conductivity of air. This perturbed the spatial temperature distribution for the chamber. More details are presented in Section 4.8.5.

Since the main goal is to demonstrate the agreement between optical and electrical methods, we can certainly say that the TCR-based temperature determination is good for the Si heater system.

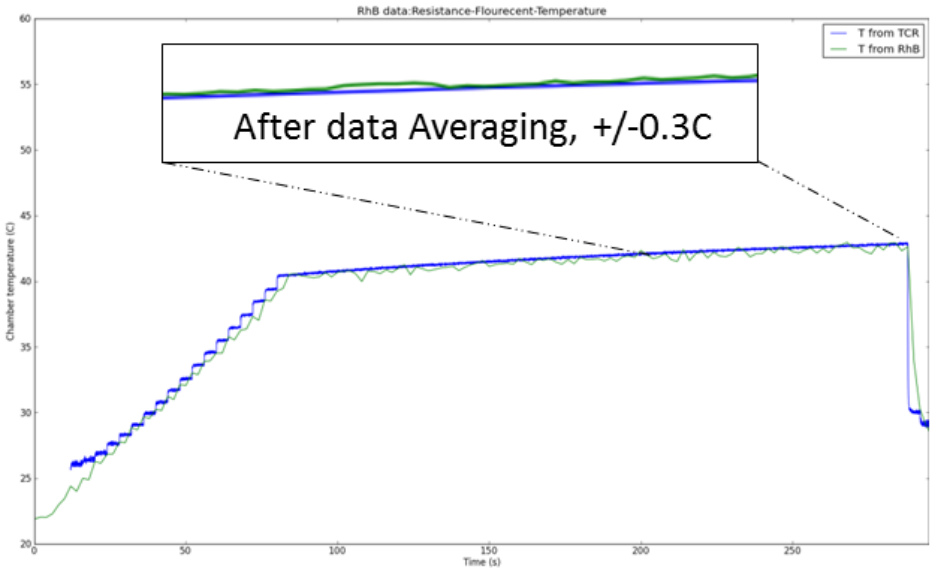

Figure 4.8: Heater temperature measurement at constant input power. For t < 80 s, the control program increased the input current in steps to reach 250 mA. While for 80 s<t<280 s, the heater input current was held at 250 mA as programed. The slope of the lines in the latter period is attributed to the heat sink warming up by an estimated 3 °C. The divergence between the two traces for t<25 s is due to the electrical noise introduced by the current source at low current region and that for t>280 s is due to the difference of the cooling rates. Optical (green line) and electrical (blue line) temperatures compared as heat sink warms up showing that even as external parameter change (primarily the heat sink temperature), the two temperatures tracked each other within 0.3 °C.

4.8.4 Determination Of Temperature Uniformity From Optical Temperature Measurement

For such a compact system it is difficult to uniformly illuminate the chamber. In order to remove this non-uniform background, fluorescent images of the chamber were taken at room temperature with illumination. Fig. 4.9a shows the illumination profile of the fluorescence in the chamber. Since the illuminating LED was placed close to the top edge, it is clear that the top of the chamber had more illumination than bottom. Since the fluorescent of the dye is a relatively attenuated at elevated temperature, the darker region (e.g., the bottom part) may have a low signal that could not be counted by the CCD element. This could lead to a distortion of the plot as shown in the right end of Fig. 4.9d. So, if the scaled down value is less than 1 count, the region needs to be excluded. In addition, the random noise is another factor that could be correlated to the distortion. Thus, any readings less than 5 counts at room temperature were excluded as shown in the shaded region. Therefore, the top half of the chamber excluding the first 100 μm was chosen as the sample area for the uniformity measurement as indicated by the yellow dotted line in Fig. 4.9c. A value of 0.57 was found to give an approximate match. It was applied to the room temperature image, which corresponds to a temperature of approximately 40 °C. Then the chamber image at 43 °C was subtracted from the scaled room temperature image. This produced a flat, relatively uniform field, which has a slightly darker (cooler) center shown in Fig. 4.9c. By performing a running average of 20 pixels along the yellow line, we extracted the temperature profile and found the temperature variation is ±0.65 °C, which was better than the 1 °C specification.

4.8.5 Limitation Of The Current Taped Chamber Si Heater Chip

During the test process, we ran into two main issues for the Si based heater: air bubbles and moisture-related heater failure.

Air Bubbles

During our testing process, the expansion of air bubbles in the chamber prevented us from measuring the chamber temperature at higher target temperatures as shown in Fig. 4.10. First, the expansion of air bubbles caused the tape layer to deform outward. This increased the optical depth for the fluorescence measurement, which led to a higher optical signal and would result in a lower temperature reading. As a result, the optical measurement showed

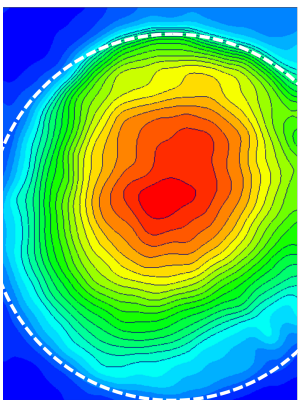

(a) Contour plot of the room temperature fluorescence image of the chamber

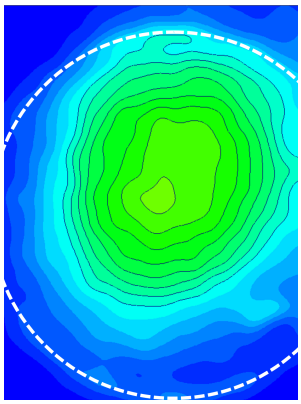

(b) Contour plot of the chamber fluorescence image at 43°C.

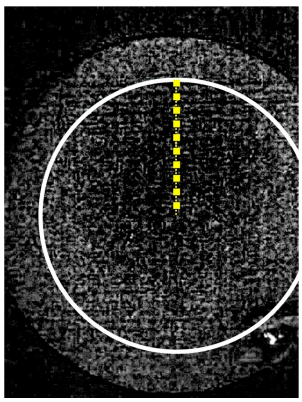

(c) Chamber fluorescence image at 43°C after correction for non-uniform illumination

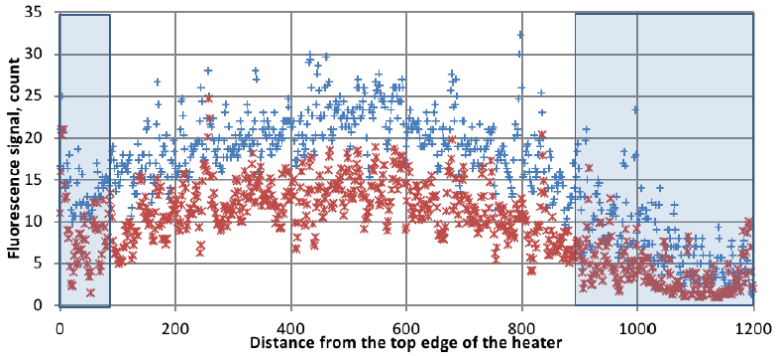

(d) Fluorescence counts across the chamber.

Figure 4.9: Optical demonstration of the chamber temperature uniformity: a) A fluorescence image of the chamber at room temperature to show the nonuniform illumination profile; b) A fluorescence image of the chamber at 43 °C; c) The result of subtracting the 43 °C chamber fluorescence from the scaled room temperature with markup of the central undistorted region. d) Counts vs distance (μm) from the chamber top edge plot for the room temperature (blue +) and the 43 °C (red ×) chamber images. Both sets of data follow the same general behavior due to the illumination. The shaded regions indicate excluded data where signal distortion occurred due to the low signal intensity.

a decreasing temperature while the TRC measurement indicated the opposite. This agreed with the results show in Fig. 4.11. Second, the air bubbles also caused a localized hot spot on the heater due the different thermal properties between air and water. This prevented us from measuring the heater uniformity and affects the accuracy of the TCR-based heater temperature.

There are two ways for air bubbles to be introduced to the chamber. First, air bubbles are trapped in the chamber during loading. Since the fluid channels are not functional, the taped chip approach is used. As a result, the loading process is done manually by pipette, a small drop of solution to the chamber and cover it with tape. During this process, air bubbles are likely to be trapped in the chamber since the KMPR surface is slightly hydrophobic. Second, dissolved air reappears from the solution at high temperature. The solubility of air in water decreases as the temperature increases. So, at higher temperature, air bubbles will appear even if no air was trapped during the loading process. However, if the chamber were pressurized to 20 psi, there would be not air bubbles appearing, since there is little change in terms of air solubility from room temperature to 100 °C at that pressure. [72]

Through practicing, the trapped air bubbles could be eliminated. However, air bubbles will always appear in the chamber at elevated temperature. Unless we move away from the taped chamber approach, this will always be a problem.

Al Heater Failure: KMPR In Moisture

The other major problem was unexpected heater failure after several hours of testing. In our group's earlier work[62], the Al traces on KMPR successfully passed the water bath TCR calibration, which required the heater to be exposed to water for a couple of hours at elevated temperature. However, unexpected heater failures were observed with these heater chips. Fig. 4.12a shows the image of one of the chip used for the RhB test. From the image, corrosion-like heater damage appears on most traces. In an attempt to reproduce this failure, a heater chip from the same batch (Batch #2) was placed in a water filled conical tube and heated in a hot water bath at 95 °C for 30 minutes. The images of the chamber before and after are showing substantial damage as in Fig. 4.12. Similar heater damage appeared on the after image. Similar results were confirmed by the UofA group on the batch #4 chips. In addition, they found that without moisture, the tested heater lasted longer.

However, through subsequent work by David Sloan at the UofA, he found that the KMPR Si heater chips fabricated by Teledyne DALSA do not have such a problem.

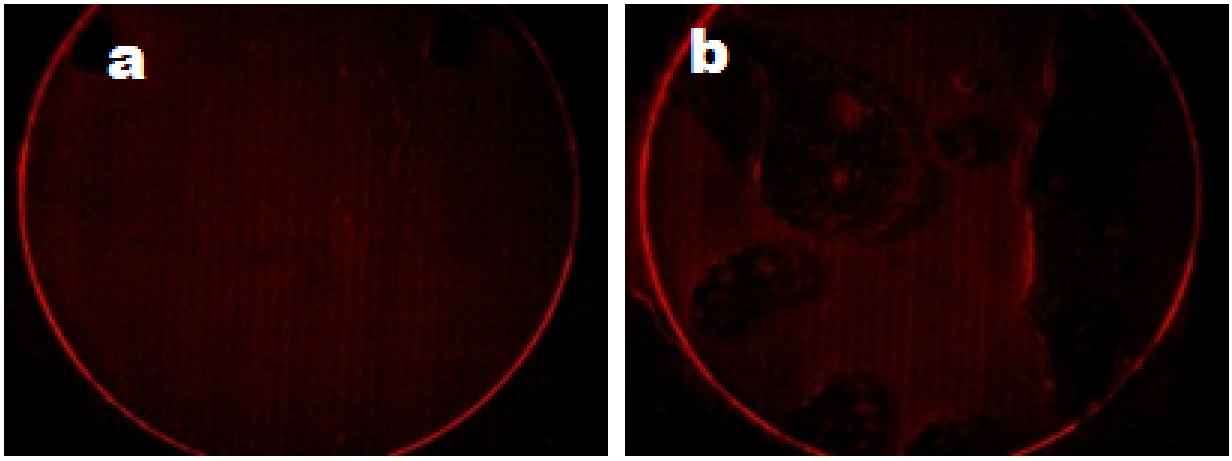

Figure 4.10: Image of bubble expanding: a) fluorescent image at room temperature; b) Image of the chamber at 350 mA input current (or 55 °C equivalent). At higher current, the air bubble area was significant in the chamber. This caused the chamber to deform outward in order to compensate for volume increase, which in turn increased the optical depth.

Therefore, it is clear that the combined effects of moisture and heating cause corrosion-like heater failure. However, this is most likely a fabrication issue since both the earlier work by Martinez-Quijada et al. [62] and the chips by Teledyne DALSA do not have such a problem.

4.9 Conclusion

In summary, we have demonstrated a CMOS-compatible heater system for integrated PCR. This system does not require device level calibration and capable of mass production via current CMOS technology. By comparing the electrical and optical methods for temperature determination, we found the results agree with each other. Thus, we have proved the concept of a robust thermal design. In addition, we have developed a helper chip for the UofA Si heater and related supporting structure. However, due to out-of-specification chips and other issues, the helper chip system could not be tested.

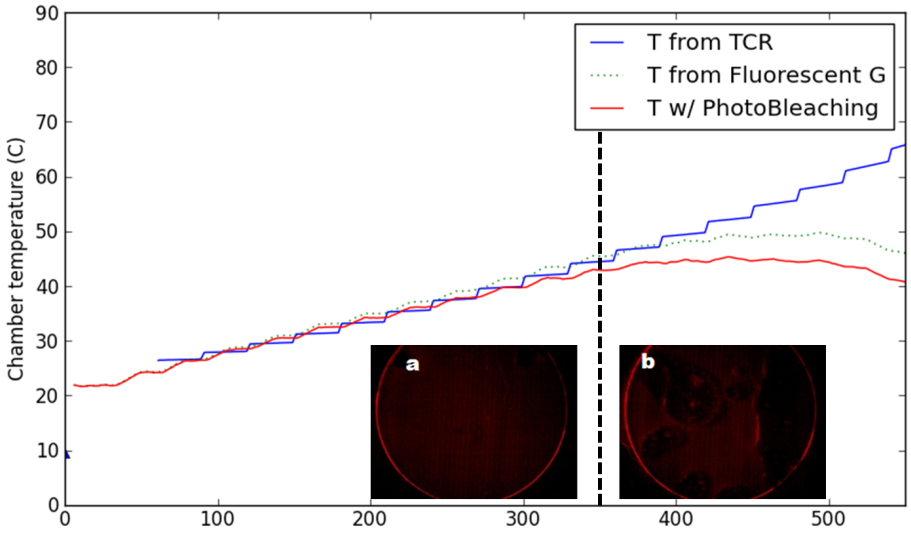

Figure 4.11: Measured chamber temperature vs time plot with the input current steps up to 350 mA: TCR measurement agrees with optical measurement at low input current; As chamber temperature increases with the input, the agreement was interrupted. By tracing the collected images, which have time stamps, the interruption occurred during the formation of air bubbles. After 350 s, significant air bubble formation appeared as shown in the right half of Fig. 4.10.

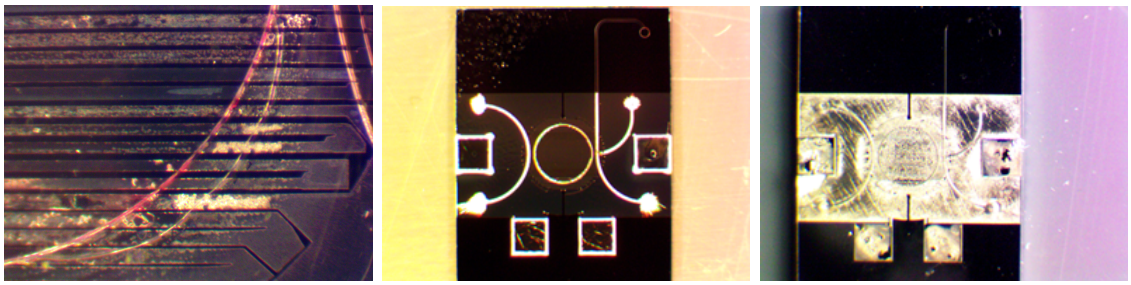

(a) (b) (c)

Figure 4.12: Heater failure after heating under water: a) Image of a chip after optical temperature detection. From the image, corrosion appeared on most traces. b) Image of a Si heater chip from the same fabrication batch before water test. c) Image of chip shown in b) after water bath heating. The chip was immersed in water and heated at 95 °C for 30 minutes. There is a significant amount of delamination and corrosion-like damage to the Al trace. Both chips were selected from the batch #2. The stereo microscope with the Amscope camera was used to take the images. Similar results were observed at the UofA with on chips selected from the batch # 4 under similar conditions.

Chapter 5

PCR-CE Platform With Discrete PCR Heater Module Plan: Tape Based Thin Chips

With the failure of the silicon chip, a fallback plan was developed using a discrete heater, with the temperature determined from either the TCR of the heater or a thermocouple. Simulations were done to investigate the relationship between the chamber and heater temperature, while initial back-of-the-envelope (BOE) calculations were made of this relationship. The chamber temperature was monitored via the TCR, the thermocouple and via fluorescence. The run-to-run variation of these indicated that the TCR was not a reliable method of measuring the temperature and the thermocouple had an offset introduced by the assembly process. These issues called for a redesign that was performed in the next chapter.

5.1 Introduction

As learned from the previous chapter, the CMOS heater may behave differently with moisture. Thus, I decided to move on with commercially available heater while waiting for a stable CMOS heater from the UofA. The essence of the CMOS thermal design of Chapter 4 was that a sufficiently small and thin chip can be very closely coupled to the heater and temperature sensor. In the absence of a viable heater from the UofA, I sought to build a suitable temperature control module from a discrete thin film heater and a very thin microfluidic chip. The initial design was done analytically with further simulation via an open-source computational fluid dynamics program, OpenFOAM, performed by a colleague (Nemanja Kliska). The heater system was experimentally tested while waiting for the simulation results. In addition, a pressurized chamber was added above the chip in order to prevent the formation of air bubbles.

In order to keep our heater scalable and compatible with our CMOS heater, a thin film heater from Omega Canada was used as an alternative heating element. The dual-purpose heater design was kept and a new control system was built for the new heater specifications. By laser patterning qPCR tape and lamination, a multilayer microfluidic structure was created to imitate the KMPR on Si substrates. Due to the lack of simulation and customization, we cannot use the same power based control algorithm used for the silicon chips. As a result, a software PID controller was programmed in Python script for temperature control. The chamber temperature was monitored via the heater TCR, the embedded thermocouple and via fluorescence. However, the run-to-run temperature variation experienced by the chip indicated that the heater TCR was not a reliable determination of the chamber temperature. Further, the thermocouple temperature had an offset introduced by the assembly process which could vary for each assembly. An even larger run-to-run temperature fluctuation was observed based on optical temperature measurements. This was strongly related to the warping of the thin tape layer under pressure. Further, from the 3D numerical simulation obtained after the preliminary test, the oversized heater (compared to the chamber area) senses not only the temperature of the chamber but also the surrounding PMMA. This leads to a temperature variation between the heater sensing temperature and the chamber temperature. A potential solution is a thin copper spreading layer above the heater as verified by simulation. However, I decided to move on with a rigid chip approach in the next chapter due to the hard-to-solve warping problem.

5.2 Discrete Heater System Design

This section gives design details for the PCR system with a discrete heating element. The main point of this approach is to build a system to demonstrate on chip PCR in a timely fashion by utilizing the known-to-be-good CE and valve modules and the knowledge learned from the Si heater system. The material and the final drawings are presented first. However, the iterative process of achieving the final design was based on simplified 1D analysis. Then, 3D numerical simulation was used to further valid this system. The system has been built and tested based on the 1D analysis while waiting for the simulation results.

In order to proceed quickly, a rectangular heater element was chosen from the Omega Canada available inventory. Even though there are circular heaters, their designed operating voltage is 115 V. Thus, a 2 inch by 0.5 inch rectangular heater was selected from the 28 V heater series, which was in stock.

Thin tape material was used to construct the chamber. In order to keep the viability of the Si heater model, a thin chip is the key design requirement. By using the robust Si heater system design from previous chapter, the tape based thin chip design was developed as an integrated PCR-CE system. The PCR tape material was used to construct the PCR chamber because the tape thickness is only 100 μm which is much less than 1.5 mm PMMA, our other readily available material.

Previously demonstrated CE and valve modules were implemented. A standard 4-port-mini chip was laminated on the tape-chip to form a standard tape-bottom CE chip for use with the μTK. The PMMA CE chip was connected to the PCR tape chip by a via located in the sample well. A PMMA support chip was laminated to the chip for the PCR region. This allowed us to build the PMMA valve in Chapter 3. Since the main focus of this chapter is the thermal behavior, only the PCR related region is presented in this section.

5.2.1 Materials And Equipments

As shown in Fig. 5.2b, the manifold was milled from 1/2 inch thick PMMA block as described in Chapter 3. The vias and supporting structure for the chip was built out of 1.5 mm PMMA substrates. The PCR chamber and microfluidic channels were built from qPCR tape (AB1170, Fisher Sci). The thin film heater was ordered from Omega Canada (KHLV-0502/(10), Omega Canada). The heater is constructed by sandwiching 0.0001 inch etched Al between 0.002 inch Polyimide Film and 0.001 inch FEP adhesive as provided by

the manufacture. The total thickness is 0.006 inch (150 μm). The insulation layers atop the Cu plate and the chips were made of the qPCR tape. A Labjack U6 micro controller was used to operate the system. A dual-channel bench-top power supply was used to power the system. Two channels of the power supply were operated in series mode to output 32 V for the heater circuits. For valving and pumping, we used the in-house built pneumatic module described in Chapter 3. The 5 V fixed voltage output port on the power supply was used to power the pneumatic module.

5.2.2 Discrete Heater System: Cross-section And Top-view

The figures presented in this section are the detailed drawing for this discrete heater system. The figures are not drawn to scale (except Fig. 5.2a). The heater system consists of three components: 1. pneumatic control structure; 2. chip and membrane; 3. heater, insulation and heat-sink. Not shown in these figures, all parts are aligned through 6 alignment pins in the Cu heat-sink. Four machine-screws (size #4-40) are used to screw down the top layers to the base.

A top-down view of the discrete heater system is shown in Fig. 5.1. The heater and the manifold do not cover the entire heat-sink. The relative location and size is shown. The actual size of the heater is about a quarter of the heat-sink area. The manifold has the same length but double the width. Two slice points are labeled to indicate the slice direction for the cross-section pictures.

Two cross-section views of the heater system are shown for more detail. In order to show the scale of the system, the cross-section view of the system along the slice point A is shown in Fig. 5.2a. The pneumatic control structure is directly atop the membrane and consists of two parts: 0.5 inch pneumatic manifold and 0.25 inch cap for applying 20 psi to the chamber. The chip and membrane layers are sandwiched between the manifold and the insulation atop the Cu plate. Along the slice point B, a zoomed-in view of the chamber section is presented in Fig. 5.2b, and a detailed description of each layer is listed in Table 5.1. As described in the previous chapter, the membrane is a single layer of 40 μm thick PP film and pressed against the top of the chip. The chip is laser ablated and closed with PCR tape to form a closed fluidic structure. Both the two movable components are aligned to the heat-sink base through six alignment pins which are not shown in these figures. Three layers of the same PCR tape are laminated on the heat-sink in order to reduce the overall power consumption.

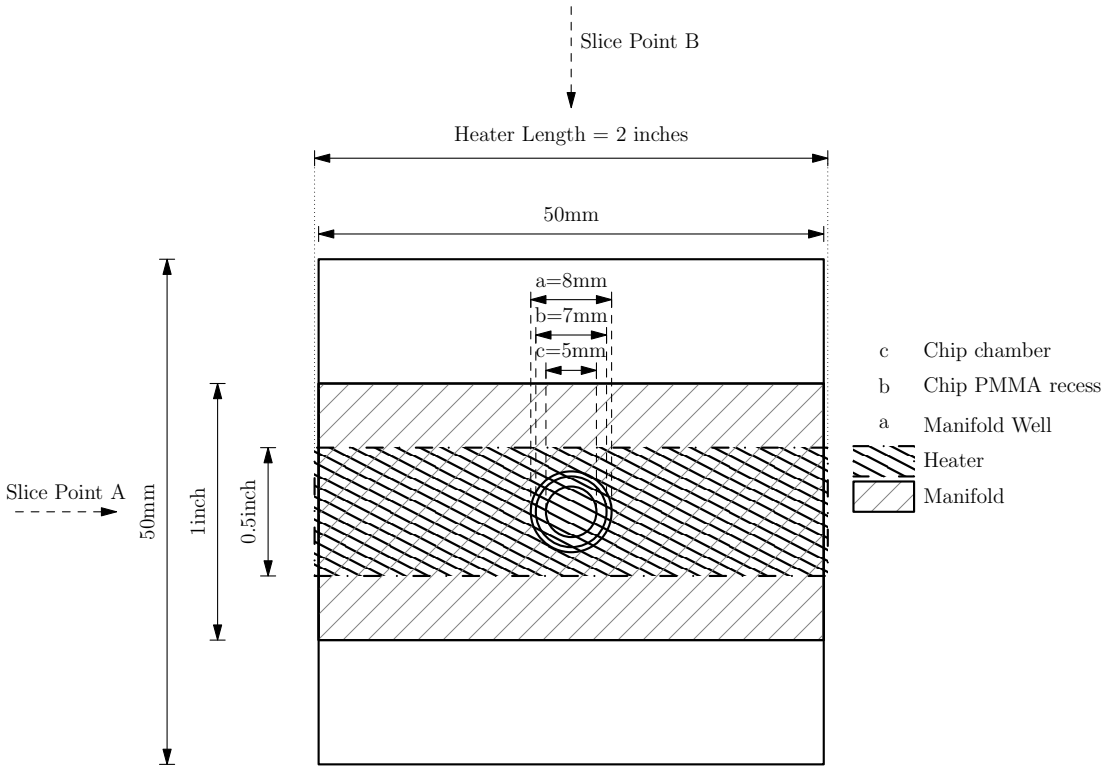

Figure 5.1: A top-down view of the discrete heater system is presented. A PMMA manifold is directly atop the membrane. The heater layer and the insulation layers are laminated to a 0.25 inch Cu plate. The chip layer is sandwiched between the membrane and the heater. As stated in Section 5.2, a rectangular heater is used due to availability. Two slice points are labeled which indicate the direction of the cross-section views which are shown in Fig. 5.2a and 5.2b.

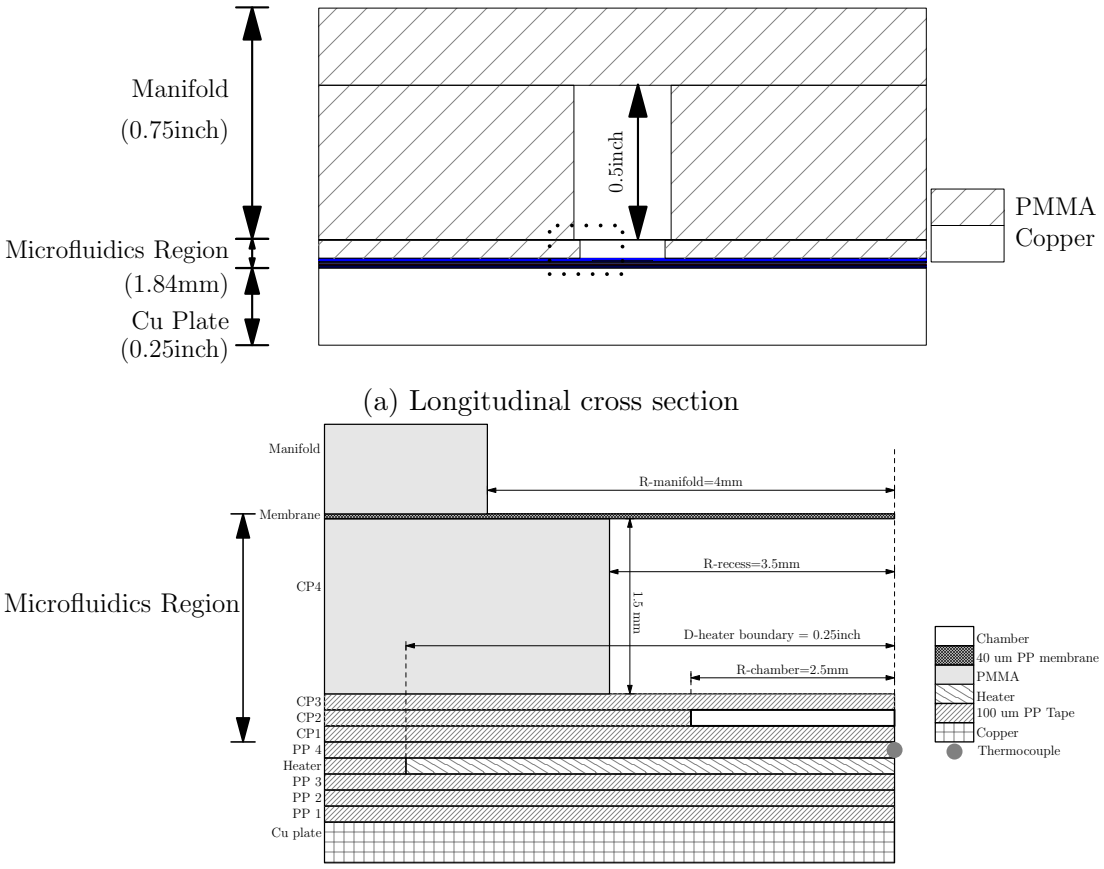

(a) Longitudinal cross section

(b) Lateral cross section

Figure 5.2: Cross-section views of the discrete heater system: a)Longitudinal cross section: a drawn to scale view along the slice point A; b)Lateral cross section: A zoomed-in view of the dotted section along slice point B with detailed labeling. The lateral view is not to scale in order to provide more details on the microfluidic region.

Name	Description
Manifold	PMMA pneumatic manifold
Membrane	40 μm PP film
CP4	1.5 mm PMMA as chip support layer
CP1,CP2 and C3	100 μm PP tape forms the channel and chamber
PP4	100 μm PP tape used to tape heater down to the heat-sink
heater	A Omega Heater (2 inch by 0.5 inch)
PP1, PP2, PP3	100 μm PP tape as insulation layers
Cu plate	Heat-sink

Table 5.1: List of all the layers in Fig. 5.2b

5.2.3 Basic Design Requirements

The requirements for this discrete heater system are listed here.

- Chamber temperature variation: less than 1 °C. Since the Omega heater is much larger than the similar chamber for the UofA Si heater and the lateral thermal resistance is high due to the thin tape structure, we focus more on the vertical gradient than the horizontal one.
- Maximum power density: 10 W/in^2. This is limited by the Omega heater specification.

5.2.4 An Analytic Model

In order to finalize the design, a simplified 1D model is used in an iterative process of finding the proper design values. Similar to the UA Si heater in Chapter 4, a thermally resistive divider network is used to represent the discrete heater system.

Concept Of A Simple 1D Model

A 1D model is representative of the near-chamber region (which is circular symmetric.) as long as it is sufficiently far from the edge. Since the circumstances dictated the use of a rectangular heater, as explained in Section 5.2, the region of validity is expected to be the smaller of the distance in the two directions.

Similarly to the Si heater design, a thin isolation region formed between the edge of the chamber and the edge of the PMMA recess allows us to construct an even simpler 1D model as in chapter 4. A simple 1D representation of the heater system could be constructed if the lateral heat flow is much less than the vertical. In order to reduce the system to 1D, the chamber region needs to be isolated from the surrounding environment (or structure). A very thin, low-conductivity structure can lead to a high thermal resistance in the lateral direction. Hence, the lateral heat flow is reduced. If this flow/loss is small enough to be neglected, the resistive network structure can be reduced to only vertical flow, which turns the device into a 1D system.

Therefore, if the taped chip were thin enough, the device will be insensitive to the lateral boundary conditions. A uniform chamber temperature will be achieved.

A Thermally Resistive Divider Design

The analogy of electrical parameters is used to represent thermal flow of the system. [68, 69] Temperature difference, heat flow and thermal resistance can be treated similarly to voltage difference, current and electrical resistance.

Vertical Thermal Resistance

By applying the electrical resistance analogy, the thermal resistance could be calculated by the area, A (m^2), thickness, d (m), and the vertical thermal conductivity, k ($\frac{W}{m \cdot k}$):

$$R_{layer} = \frac{d}{kA} \tag{5.1}$$

The heat flow, H (W), is similar to current as it crosses each layer:

$$H = \frac{\Delta T}{R_{layer}} \tag{5.2}$$

where ΔT is the temperature difference.

Lateral Thermal Resistance

As shown in the heater cross-section view, the chamber area is less than the heater area. The circular recess in the 1.5 mm PMMA layer (which is used to reduce the thermal mass) is also away from the edge of the chamber. The lateral resistance, R_L, caused by edge effect of the PMMA surrounding, can be approximated by the cylindrical section formed by the region between the edge of the chamber and the edge of the recess.

$$R_L = \frac{1}{2\pi kd} \ln(\frac{r_2}{r_1}) \tag{5.3}$$

where r_1 is the inner radius; r_2 is the outer radius, and $d$is the thickness of the cylinder. For the purpose of estimating RL, we use r_1= 2.5 mm, r_2=3.5 mm and d= 400 μm. By substituting in the values for the tape chip, R_L = 669.4 $\frac{K}{W}$. I will reference back to this value in a later section.

Thermally Resistive Divider Network

As shown in Fig. 5.3a, an electrical resistor-network representation is drawn to illustrate each layer of the heater structure, which was replaced as a resistor. So, the temperature at any node in the structure could be calculated. The symbol for each layer resistance and node are listed in Table 5.2. Table 5.3 has listed the material properties and the vertical resistance for 2.5 mm radius chamber of each layer.

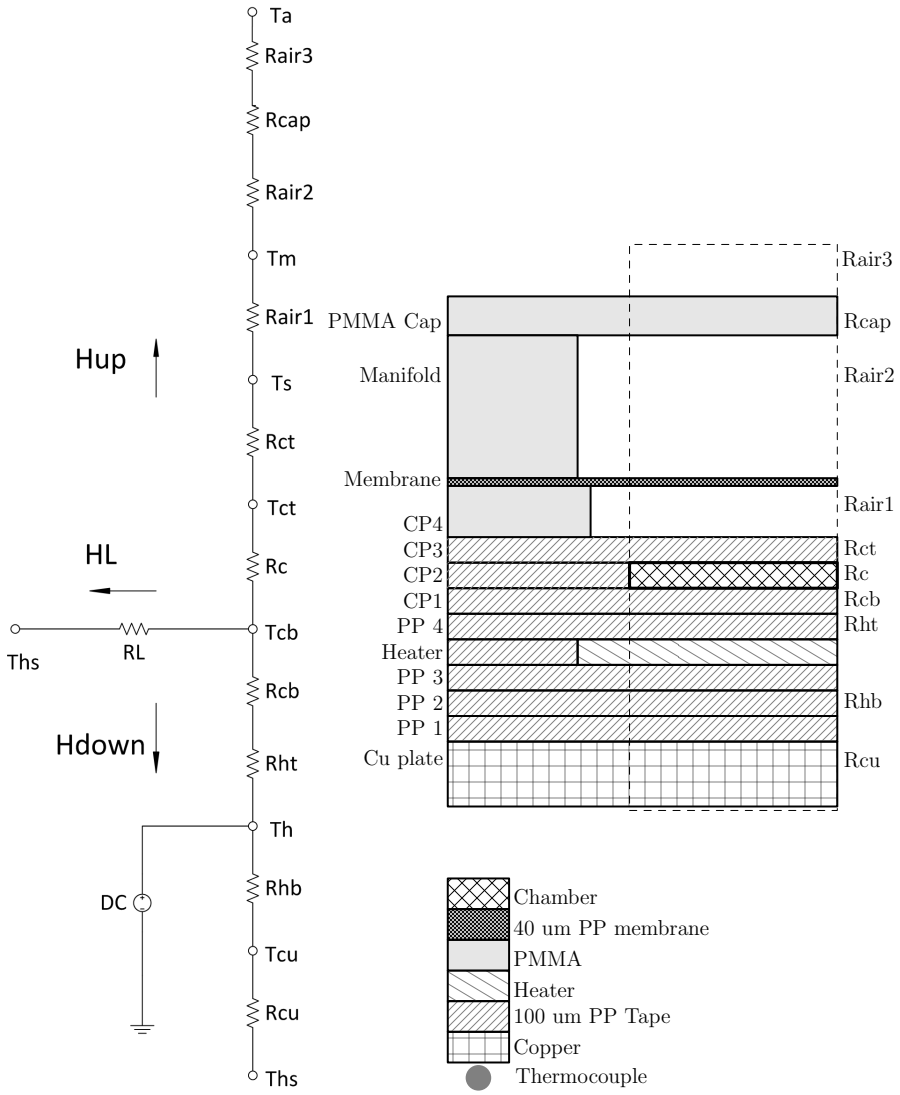

Figure 5.3: Resistive divider network of the thin chip and the Omega Heater system: a) Circuit representation of the heater analytic model; b) Heater cross-section with thermal resistance labeled.

Symbol	Description	Corresponding Layer
T_a	Room Temperature	-
R_{air3}	Convection above the cap layer	
R_{cap}	1/4 inch PMMA cap layer above the manifold	PMMA Cap
R_{air2}	1/2 inch air above the membrane layer	Manifold
T_m	bottom temperature of the pp membrane	-
R_{air1}	1.5 mm air above the chip	CP4
T_s	chip surface temperature	-
R_{ct}	top tape layer of the chip	CP3
T_{ct}	chamber top surface	-
R_c	water-filled chamber	CP2
T_{cb}	chamber bottom surface	-
R_{cb}	bottom tape layer of the chip	CP1
R_{ht}	tape layer above heater	PP4
T_h	heater temperature	-
R_{hb}	tape layer/layers below heater	PP1, PP2 and PP3
T_{cu}	Cu surface temperature	-
R_{cu}	Cu heat-sink	Cu plate
T_{hs}	heat-sink temperature	-

Table 5.2: List of temperatures and thermal resistances labeled in Fig. 5.3a, and the corresponding layers in Fig. 5.3b.

Heat Losses: Convection vs Conduction

Heat loss through air could occur by either conduction or convection, which could result in significantly different thermal behavior. In general, convection loses heat faster, but it is more sensitive to the air conditions (i.e. flow rate, air volume). Conduction is simpler and more stable. The Rayleigh number, RA, could be used to determine which of the two is dominating the thermal flow in a closed volume of air or fluid. [73]

$$RA = \frac{g\beta\Delta T L^3}{\nu\kappa} \tag{5.4}$$

where g is acceleration due to gravity, β is coefficient of thermal expansion, ΔT is temperature difference, L is the characteristic length, ν is kinematic viscosity and κ is thermal diffusivity.

Material	Conductivity $k(\frac{W}{m \cdot K})$	Thickness d(mm)	Resistance R($\frac{K}{W}$)
PMMA	0.2	5 mm	1273
$air_{conductive}$	0.02	1.5 mm	3820
pp-tape	0.22	0.1 mm	23.15
water	0.67	0.1 mm	7.60
cu	400	5 mm	0.64
$air_{convective}$ (Rair2 and Rair3)			9095
Lateral (R_L)			669.4

Table 5.3: Thermal conductivity and resistivity for a 5 mm diameter chamber

In order to find the critical distance, L, where the convection becomes dominant, an air layer between two parallel surfaces was used as a simple model. One surface is kept at 20 °C, and the other is at 95 °. For estimation, I take $g = 9.8\ m/s^2$, $\beta = 3.44 \times 10^{-3}$ 1/K, ΔT=75 °C, $\nu = 15.11 \times 10^{-6}\ m^2/s$ and $\kappa = 1.9 \times 10^{-5}\ m^2/s$. For a fluid layer between two rigid boundaries, the critical Rayleigh number is 1708. [73] By applying all of these parameters into Eq. 5.5, the critical distance is found to be:

$$L \leq \sqrt[3]{\frac{RA \cdot \nu\kappa}{g\beta\Delta T}} = 0.00579m = 5.79mm \tag{5.5}$$

Therefore, at a distance larger than 5.79 mm between two surfaces which are 75 °C apart the convection heat loss dominates the air thermal flow.

However, from Eq. 5.4 the critical distance is inversely proportional to the temperature difference. For the 0.5 inch air chamber, in order to keep the chamber in convective heat loss, the minimum critical temperature difference is estimated to be $\Delta T_{minimum}$= 4.36 °C. As a result, if the temperature difference is less than 4.36 °C between the membrane and the bottom of the PMMA cap, the 0.5 inch air chamber will be in the conductive region. This will be verified in later section after introducing the boundary conditions for the system.

As shown in Fig. 5.2a, R_{air2} is convection and R_{air1} is conduction heat loss. We can find $R_{air1} = 3827\ \frac{K}{W}$. With a heat transfer coefficient, htc, of 5.6 $\frac{W}{m^2 \cdot K}$, the effective thermal resistance of the R_{air2} is:

$$R_{air2} = R_h = \frac{1}{htc \cdot A} = 9095\frac{K}{W} \tag{5.6}$$

Based on the above critical lengths, the 1.5 mm thick air pocket is in the conductive region, while the 0.5 inch air chamber is convective. However, as the manifold temperature increases with time, the air chamber might be dominated by conduction if the temperature difference is less than 4.36 °C.

5.2.5 Time Constant

In contrast to the Si heater system in the previous chapter, the taped chip is about 4 times the thickness of the silicon chip. A slow time response of the system is expected, which we can estimate from the resistance and capacitance of the chip, using Eq. 5.7. In order to estimate the time constant, we lumped the chamber bottom tape layer (R_{cb}) and the chamber (R_c) together as the thermal resistance. The heat capacitance includes all the layers in charmer region above the heater, which are the chamber bottom tape layer, the water-filled chamber and the chamber top tap layer. By substituting the value, thermal resistance is $R_{thermal} = 34.2\ \frac{K}{W}$; heater capacitance (C) is $C = 0.013\ \frac{J}{K}$. The time constant is $\tau = 0.45$ s for the heating process for the chamber region only.

$$\tau = R_{thermal}C \tag{5.7}$$

$$C = \rho c A d \tag{5.8}$$

where ρ is the density of the material.

In order to estimate the time constant of the bulk material, Eq. 5.7 could be simplified to the following equation:

$$\tau = R_{thermal}C = \frac{d}{kA}(\rho c A d) = \frac{d^2 \rho c}{k} \tag{5.9}$$

Thus, the time constants for the bulky PMMA structures above the chamber layer are estimated and listed in Table 5.4. If the steady state is defined as reaching 98 % of the final value, the heating time for the bulky PMMA structure (the chip, the manifold and the cap) is about 4.5 hours. Since a PCR process in general takes about 2 hours to finish, it is clear that the overall system is far from reaching the steady state.

Material	Thickness cm	Density $\frac{g}{cm^3}$	Heat Capacity) $\frac{J}{gK}$	Conductivity $\frac{W}{cmK}$	Time constant s
Air pocket	0.15	1.2×10^{-3}	1.0	2.57×10^{-4}	0.1
Air chamber	1.25	1.2×10^{-3}	1.0	2.57×10^{-4}	7.30
PMMA chip	0.15	1.2	1.5	0.002	20.25
PMMA manifold	1.25	1.2	1.5	0.002	1406.25
PMMA cap	0.5	1.2	1.5	0.002	225
Total PMMA structure	1.9	1.2	1.5	0.002	3249

Table 5.4: List of the thermal time constants

5.2.6 Boundary Conditions

In order to analyze this thermal resistive divider network, the boundary conditions are presented in this section. For all the boundaries, the room temperature is kept at 20 °C.

In the vertical direction, both the top and bottom boundaries are kept at constant temperature. Based on the results in Section 5.2.4, the air above the PMMA cap, R_{air3}, is in the convection region. At infinity, R_{air3} is connected to the room temperature, T_a. The bottom of the Cu heat-sink is kept at room temperature with a Dirichlet condition by assuming a perfect heat-sink is attached. Within the heater system, the heater layer is kept at 95 °C in order to represent a feedback controller.

In the lateral direction, an insulating boundary condition is to the the edge of the chamber in order to simplify the system to 1 dimensional space. For the chamber region, the total vertical resistance, which is the vertical resistance of the chamber area above the heater layer, is $R_{v-chamber} = R_{ht} + R_{cb} + R_c + R_{ct} = 77\ \frac{K}{W}$. The lateral resistance is estimated to be $R_L = 669.4\frac{K}{W}$ as calculated in earlier section. So the lateral heat flow is about 10 times less than the vertical flow for the chamber region. Therefore, an insulating boundary condition could be applied. In reality, the lateral heat flowed the opposite the direction and increases with time as the PMMA structure heats up during the process. So, the insulating condition may not be valid after hundreds of seconds. However, this is too

complicated for a simple model. As a result, a 2D numerical simulation was requested for further validation.

5.2.7 Maximum Chamber Depth

From the 1D model, one can estimate the temperature drop from the bottom to the top of the chamber. The heat flow to the top, H_{up}, could be estimated as:

$$H_{up} = \frac{T_h - T_a}{R_{ht} + R_{cb} + R_c + R_{ct} + R_{air1} + R_{air2} + R_{cap} + R_{air3}} \tag{5.10}$$

where the lateral heat flow is neglected as described earlier. The chamber temperature difference (or vertical temperature variation), $T_{cb} - T_{ct}$, is the product of H_{up} and chamber thermal resistance, R_c. By setting the maximum $T_{cb} - T_{ct}$ to be 1 °C, one can estimate the maximum chamber thickness by using the 1D model. From R_c, we can find the maximum thickness of the chamber. R_{ht}, R_{cb} and R_{ct} are one layer of PP-PCR tape with a thermal resistance of 23.15 $\frac{K}{W}$ for 5 mm diameter chamber.

$$T_{cb} - T_{ct} = H_{up} R_c \tag{5.11}$$

The worst case scenario is at the beginning of the heating process. Since the air chamber is still at room temperature, the heat flow is much higher than the steady state due to the larger temperature difference. A much higher temperature drop should be expected for this initial state. As estimated in the previous section, the time constants for both the chamber layers and the 1.5 mm air pocket are within the same order of magnitude. Therefore, I can assume the chamber layers and the air pocket reach the same time state during the heater process.

Let us assume room temperature is applied at the membrane layer at the initial state. The top of R_{air1} will be at 20 °C. In other words, R_{air2}, R_{cap} and R_{air3} are all neglected. Other parameters are: $T_h = 95$ °C, $R_{ht} = R_{cb} = R_{ct} = 23.15$ $\frac{K}{W}$, $R_{air1} = 3820$ $\frac{K}{W}$ and $T_{cb} - T_{ct} = 1$ °C. By substituting the numbers, R_c is found to be 52.6 $\frac{K}{W}$, which corresponds to a thickness, $d_{chamber} = 0.69$ mm ≈ 700 μm. Therefore, when the chamber thickness is less than 700 μm, vertical temperature variation is less than 1 °C for the worst case scenario.

For the 100 μm deep chamber, the temperature difference is estimated to be 0.15 °C. In addition, the maximum offset between heater and PCR chamber bottom could be estimated

for 100 μm chamber in the above worst case scenario:

$$T_h - T_{cb} = H_{up}(R_{ht} + R_{cb}) = 0.89°C \tag{5.12}$$

Therefore, for a 100 μm deep PCR chamber, the temperature difference is much less than the 1°C requirement, and the temperature offset between the heater and the chamber is only 0.89 °C in this worst case scenario.

5.3 Requested 3D Simulation For Discrete Heater System

As stated at the beginning of this chapter, the 3D simulation was required to validate the discrete heater system. The 1D analytic model is a simplified model that neglects the lateral heat flow of the system. However, this is true only at the beginning state of the heating process. As the PMMA structure around the chamber region heats up with time, the lateral flow may increase and break the assumption for the 1D system. Therefore, after proving the viability through the simple 1D analytical model, 3D simulation was expected to provide further validation of the discrete heater system. This 3D simulation work was carried out by my colleague, Nemanja Kliska. In this section, the detailed requirements for requested simulation work are presented.

5.3.1 Boundary Conditions And Assumptions

Boundary conditions and assumptions are listed below to setup the simulation model. The surrounding room temperature is set to be 20 $°C$. The Robin condition (or convective boundary condition) is applied to the top surface of the PMMA cap and the outside of the manifold (right edge) with a constant convective heat transfer. Similar to the 1D model, the bottom of the heat-sink is modeled by a Dirichlet condition (the boundary is kept at a constant value), which is kept at room temperature. By assuming cylindrical symmetry, a Neumann boundary condition (the flux at the boundary is kept constant) is applied in the center as shown in Fig. 5.4.

Inside the heater region, a Dirichlet condition is assumed at the heater surface to represent a PID controlled heater. The heater target temperature should be set to 55 $°C$, 72 $°C$ and 95 $°C$ for each step of the PCR process.

From the spatial and time-domain variation, we should be able to verify the chamber temperature uniformity and temperature offset between the heater and the chamber.

1. Room temperature is set to be 20 $^{\circ}C$.

2. Robin condition: Constant convection heat loss on all surfaces exposed to the surrounding air, unless specified otherwise.

3. Dirichlet condition: $T_{Cu} = 20\ ^{\circ}C$. The Cu plate is in contact with a perfect heat-sink, which is assumed to be at 20 $^{\circ}C$.

4. Neumann boundary condition: There is no heat flux across the boundary.

5. Heater has spatially uniform temperature at the set temperature. This assumes that the heater can cool instantaneously as required - clearly a non-physical situation. Nevertheless, the simulation would provide insight into the heating stages where $T_{chamber}$ can vary (upwards) almost instantaneously.

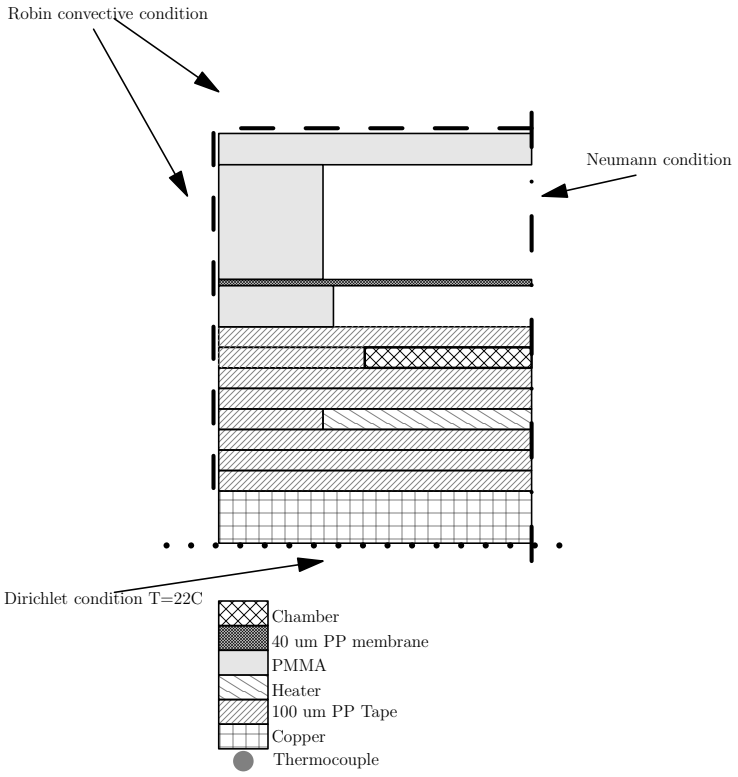

Figure 5.4: Cross-section view of the heater system with boundary conditions labeled.

5.4 Experiments

While waiting for the 3D simulation result, the discrete heater system was built based on the result of the 1D model. The fabrication process and control circuitry were based on the design used in Chapter 4 with minor modifications. A software PID controller was used to control the heater temperature based on TCR similar to the Si heater system in Chapter 4. A thermocouple plugged into a compatible digital multimeter was used to monitor the heater temperature. Rhb filled chips were used to monitor the heater temperature optically during the testing process similar to what has been described in Chapter 4.

Although TCR-based temperature determination was possible in Chapter 4, the lack of symmetry and uniformity in the present design makes that technique challenging to apply. Nevertheless, it was hoped that the technique could be applied here. It was intended that thermocouple-based measurements would be used if needed.

5.5 Results

5.5.1 Time-domain 3D Simulation

This section summarizes the 3D simulation work done by my colleague, Nemanja Kliska. This work provided simulation validation to my analytical model. As stated in the introduction section, an open-source computational fluid dynamics library, OpenFOAM, was used to simulate this heater system. In order to find the dynamic behavior, the standard solver for transient multi-region conjugate heat transfer, chtMultiRegionFoam, was used for this simulation. Finite-volume method and implicit Euler for time-stepping were used for spatial and time-domain analysis.

Modified Boundary Conditions

The boundary conditions used were modified as shown in Fig. 5.5. For simplicity, the heater system was represented by a cylindrical shaped system as shown in Fig. 5.2b.

First, the geometry of the simulated system was smaller than requested. The outer edge of the simulation was the edge of the heater which is a 0.25 inch circle. The manifold and heat-sink structure outside the heater region were ignored. Further, the manifold, the air chamber and the PMMA cap were not considered. The reason for these is that the total allowed computing power was limited. In order to get fine resolution (tighter mesh

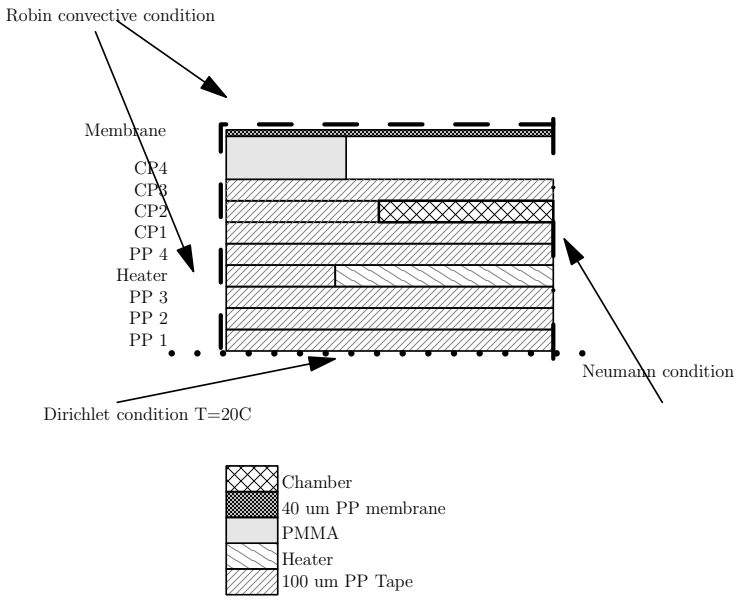

Figure 5.5: Cross-section view of the heater system with modified boundary conditions.

points) in the heater region, the bulky structures further away were ignored. As shown in Fig. 5.2a, the heater region is only a small potion of the manifold.

Second, the Robin condition was applied atop the membrane layer. Since the manifold is removed, the top of the membrane becomes the upper bound of the system. In addition, according to the 1D analysis, the convective heat loss is dominant atop the membrane. Thus, the Robin convection condition is applied.

Third, an insulating condition was applied at the outer boundary in the lateral direction. Since the area outside the heater was removed from the simulation, the convection condition was no longer valid. The heater outer edge is far away from the chamber compare to the edge of manifold recess. Thus, the effect of the heater edge is much less.

Fourth, instead of constant temperature a constant power density condition was applied to the heater. The constant power density condition is a much more realistic condition since the same amount of electrical current goes through the heater trace. In addition, as explained in the 1D analytic model, the lateral heat flow could change dramatically shortly after the heating process due to the different thermal mass over the heater. Thus, a power density approach is in favor. However, in order to verify the use of the TCR based measurement, which is such an interesting method and compatible with the Si heater in the previous chapter, a measurement layer was introduced directly atop the heater layer

to measure the temperature uniformity of atop the heater layer.

Fifth, the top of the Cu heat-sink is fixed at room temperature. Similar to the manifold, the geometry of the heat-sink is neglected for simplicity.

Other boundary conditions were the same as requested. The external boundary conditions approximated the operation of the device ambient temperature (20 °C). All the internal boundaries between layers were assumed in close contact with continuous boundary conditions.

Simulation Results And Analysis

Although the system simulated was quite different from that built, some important lessons were learned - notably that the design was such that the system could not be characterized by a single temperature, whether measured by thermocouple or by TCR. Therefore, a power density based approach was used. By performing a series of stationary simulation with different power densities, my colleague first found the power density corresponding to 95 °C was 0.41 W/mm^2. This uniform power density was then used through all the simulations. Limited by the total computational power, a maximum 10 s transient simulation was performed for the system.

Time Constant: For the chamber region, the characteristic response time of the average chamber temperature, τ, was found to be 2.54 s. This difference is about 6 times slower than the value predicted through the 1D analytic model. This difference can be caused by the radial heater flux which was neglected in 1D model.

Maximum Temperature Difference: The temperature difference within the chamber and the offset temperature between the chamber and the heater are the two most important values. From the analytic model, the maximum chamber temperature difference was estimated to be 0.15 °C in vertical direction. The temperature offset was 0.69 °C. From the simulation results in Fig. 5.6, the maximum temperature variation in the chamber region reached 5 K for in 2 seconds. Then it gradually dropped to 1 K before it increased slowly to a constant value of 2 K at the end. This complex behavior of the blue line is the result of the lateral heat flux which was neglected in 1D. In terms of the average temperature difference, the average heater temperature was 17 K higher than the average chamber temperature at the initial state. Shortly after, the average heater temperature was about 5 K less than the chamber. This is completely different than the 1D analytic model which predicted a constant offset. The main cause is the large heater area under the manifold, which has a much bigger time constant. Thus, even though the chamber heats up quickly, the cold manifold keeps the majority of the heater surface at a lower

temperature. Therefore, there is a radial temperature gradient above the heater surface as shown in Fig. 5.7. This lateral temperature gradient is also the main cause of the larger temperature difference.

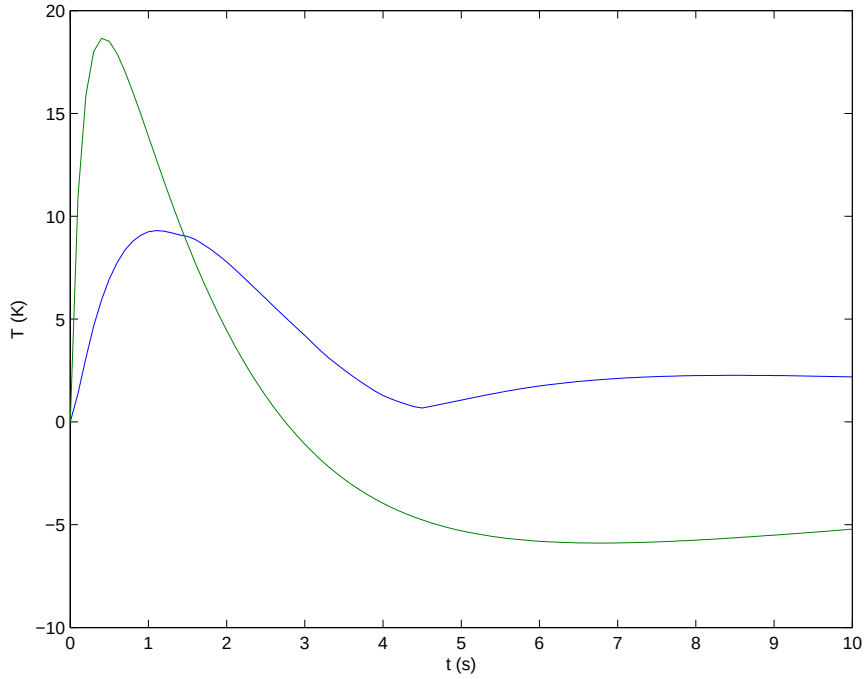

Figure 5.6: Plot of temperature variation of the system versus time. The blue line shows the maximum temperature difference within the PCR chamber. The green line is the result of the average chamber temperature minus the average heater temperature.

TCR Based Temperature Determination: The TCR based temperature determination is no longer valid for this discrete system. The TCR based measurement is a representation of the average temperature of the surface. Since the radial temperature distribution is not uniform as shown in Fig. 5.7, TCR based measurements are no longer indicative of the chamber temperature. Even though the concept is attractive as discussed in previous chapter, the TCR based method is invalid unless the thermal gradient is removed.

Proposed Solutions

Since the main problem is the radial temperature gradient across the heater surface, a thin Cu layer was proposed to fix this problem. In order to minimize the radial gradient, a

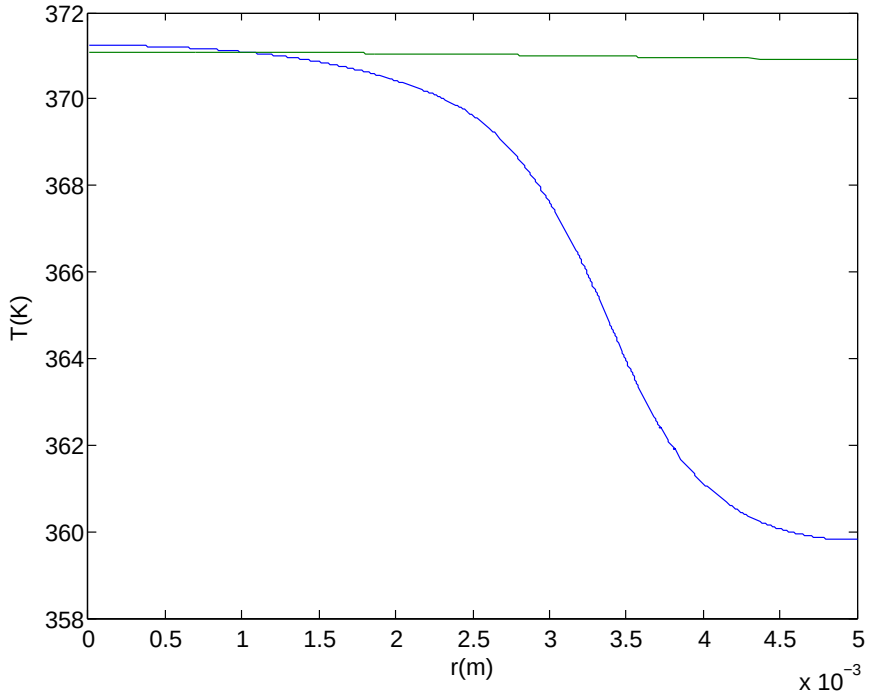

Figure 5.7: Radial temperature distribution of the top heater surface. The blue line is the original design which showed a significant temperature change across the heater surface. The green line (flat line) is the distribution of the modified design.

200 μm copper layer was directly placed above the heater element and covers the entire surface of the heater. Although of questionable usefulness in terms of PCR, it does serve to show that the Cu layer can provide a locally uniform temperature. This highly thermal conductive layer will increase the lateral heat flow and enhance the temperature uniformity. As shown in Fig. 5.7, the temperature difference across the heater decreases from 11 k to 0.4 K. Thus, this new design is improved significantly in terms of temperature uniformity. In addition, the maximum variation within the chamber becomes less than 0.5 K for the new design. Furthermore, the TCR approach becomes valid again thanks to the much reduced temperature variation. However, the drawbacks for this new design are a much higher power requirement and strong coupling of the chamber to the environment.

5.5.2 Preliminary Heater System Test Result

A mockup PCR test with 100 μM RhB solution filled chip was tested on the original heater design (without the copper layer) on two consecutive days. The chamber temperature from optical (dotted lines) and TCR (solid lines) methods were collected and plotted in Fig. 5.8. The run-to-run variation of the TCR results is very small. However, the optical method showed a great variation from run-to-run, which is about 40 K. Even within one test run, the optical-based temperature showed a 10 K increase after each cycle.

The 10 °C temperature increase agrees with the 3D simulation results. From simulation, the average chamber temperature was higher than the average heater temperature due to the lower temperature of the manifold. As the surrounding structure heating up, the average chamber temperature increases with time. Therefore, the optical temperature measurement increases with time.

The 40 °C assembly-to-assembly variation was mainly a result of the warping of the tape chip. Similar to the air bubble problem for the Si chip, the tape chamber deformed randomly during the heating process. The pressurized chamber prevented the expansion of air bubble and out gassing, but the expansion of fluid upon heating pushed the chamber outward. In theory, we should expect a slowly bulging chamber, but the built-in stress of the tape caused the chamber top to deform randomly. The built-in stress was introduced during the lamination process of the taped chip. Due to the flexible nature of the tape, it cannot be controlled with the current recessed thin chip design.

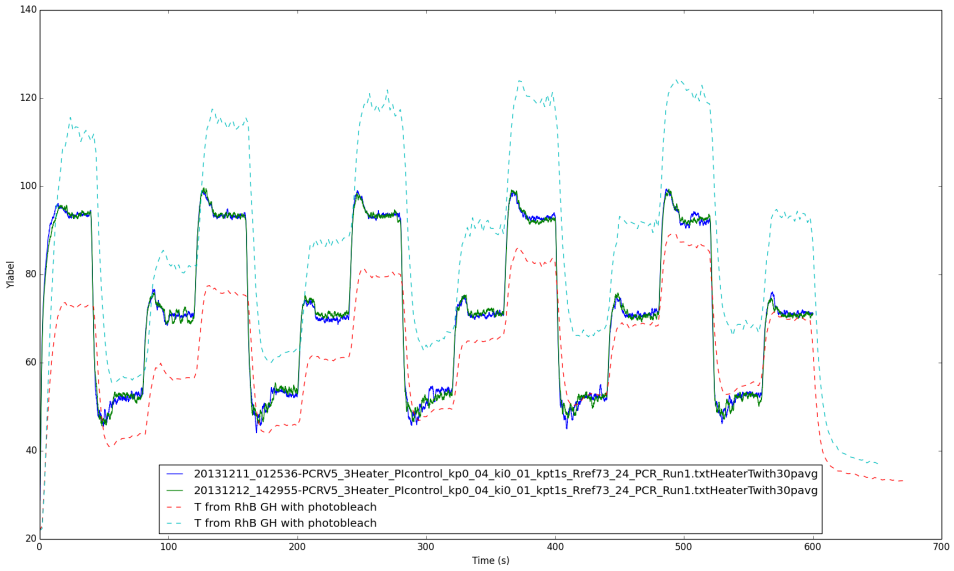

Figure 5.8: Mockup PCR by using one tape-sealed PCR chamber on 2 different days: Solid line is TCR determination of temperature; dashed line is temperature from RhB fluorescence. Significant run-to-run variation and difference between TCR and RhB value have been observed.

5.6 Summary

In summary, a discrete heater system was developed as a fallback plan with the failure of the UofA silicon heater. A simple 1 dimensional analytic model was used to design the system via iterative process with the initial BOE calculations.

For validation, time domain 3D simulations were performed to investigate the relation between the heater and chamber temperature. However, as shown from the simulation, the TCR based temperature control is no longer valid due to the nonuniform temperature distribution at the heater surface. The chamber temperature variation of 5 K was also estimated, which was much higher than the analytic result and did not meet the design requirements. In order to fix these problems, a thin Cu layer was proposed. By inserting a Cu layer atop the heater, a uniform radial temperature distribution was achieved. Thus, the chamber temperature uniformity was enhanced. Further, it enabled the TCR based temperature determination.

The preliminary testing results of the original system agreed with the simulation results and showed the expected problems. However, the thin tape based chamber structure presented a problem that had a larger effect on chamber temperature and was much more difficult to fix. Therefore, instead of rebuilding the system with the proposed Cu layer, a system redesign was performed with a rigid chamber structure in next chapter.

Chapter 6

PCR-CE Platform With Discrete PCR Heater Module Plan: PMMA Based 1.5 mm Chips

Based on the results obtained in Chapter 5, I redesigned the system using a rigid chip design. The chip was constructed from 1.5 mm PMMA substrates by laser ablation. A copper layer of 3.25 mm radius was placed atop the heater and centered to the PRC chamber. A K-type thermocouple was embedded in the copper to determine the temperature. 1D and simple 2D analytical models were developed and simulated using lumped resistance and capacitance models by LTspice software. The results show good agreement between the sensor temperature and the chamber temperature. In addition, an integrated fully automatic PCR-RFLP-CE design is presented utilizing the proven pumping and CE modules.

6.1 Introduction

In the previous chapter, there were two lessons learned: 1) Tape-based chips were too soft to determine the temperature optically; 2) The TCR-based temperature determination method did not show the accurate chamber temperature due to the lateral thermal flow. To solve these problems, a 1.5 mm PMMA based rigid chip design was developed in this chapter. Rigid PMMA substrates do not deform as easily as tape substrates. This prevents the bubble expansion during heating. In addition, the 1.5 mm thick PMMA allows the increase in the chamber volume by increasing chamber depth. The most important advantage of the PMMA design is the capability of integrating Auto-RFLP functions on the chip. Since auto-RFLP had been demonstrated on 1.5 mm PMMA in Chapter 3, a smooth transfer for a PCR-RFLP chip could be expected.

In this chapter, I will first present the heater system design and follow with a 1D analytical discussion for the chamber thickness. I then describe a 2D thermal resistive model which was used to verify the system thermal performance. Further, a 3D simulation was requested for further validation. As a proof of concept, simple PMMA chips were tested for PCR on the heater system. The preliminary result showed successful amplification of the target DNA. After validation, this chapter is concluded by proposing a fully integrated PCR-RFLP chip design for the current system.

6.2 PMMA Based Chip Design

This section describes the PMMA based chip for the discrete heater. The PMMA chip is different from the tape based chip due to the PMMA thickness, which would increase the thermal time constant, τ, for the system.

Name	Length (mm)	Description
$r_{chamber}$	2.5	The PCR chamber radius.
$r_{manifold}$	4.0	The radius of the manifold cavity above the chamber.
r_{heater}	6.5	The width of the heater pad.
r_{outer}	13	The width of the manifold.
r_{Cu}	3.25	The radius of the Cu spreading layer.

Table 6.1: Design dimensions for PMMA based Heater System

The design imitated the tape chip in terms of the dimensions. However, the chamber thickness was increased to 0.5 mm. This has two purposes: 1) The total PCR reagent

volume became 9.8 μL, which is about the same volume as used in a regular PCR tube; 2) The laser engraved channels had the same depth as the chamber, which eases the fabrication process. Even though the manifold is a rectangle and covers more than just the heater, the system was assumed to be cylindrical from the chamber center to the long edge as discussed previously in Section. 5.2.4.

As mentioned from the previous chapter, a thin Cu spreading layer was included with a radius of r_{Cu} =3.25 mm, which is at the middle between the manifold and chamber edge. For the current design, if the Cu is only under the chamber, the chamber will see a greater edge effect. However, if the Cu is extended all the way to the manifold, the Cu will conduct the heat away. Thus the Cu radius is chosen to be at the middle.

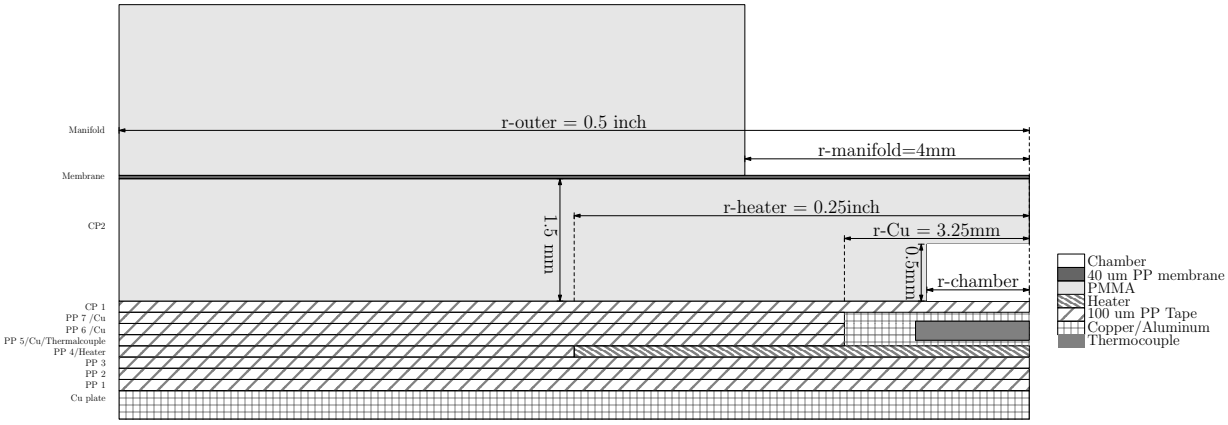

Figure 6.1: PMMA chip cross section: the dimensions are as labeled. The cross-section is perpendicular to the long side and only half is shown due to symmetry.

6.3 1D Resistive Model For PMMA Based Chip

Similar to the previous chapter, the electrical analogy is applied to the heat transfer of this heater system. In this chapter, I will analyze the heater system by drawing an equivalent electrical circuit with values representative of the designed system. Time-domain simulations are performed on the equivalent circuit by using LTspice software.

6.3.1 Vertical Heat Flow For Chamber

Before getting into the more complicated system, I started with the simple vertical heat flow for the system. Table 6.2 shows the related thermal constants. From top to bottom, the heater system consists of: air, PMMA, water, heater-top layer (1 layer PCR tape layer and a 50 μm Polyimide (PI) film), heater, heater-bottom layer (a 50μm PI film and 3 layers PCR tape) and Cu plate. The bottom of the Cu plate is set to room temperature since Cu has such a high thermal conductivity. The vertical thermal resistance of the surface can be calculated by the same equations presented in previous chapters. To calculated results for the chamber region in vertical direction are included in Table 6.2.

By using these numbers, one can draw the schematic in LTspice as shown in Fig. 6.2a, where R_{air} is the convective heat loss at the top, R_{PMMA} is the PMMA layer above the chamber, R_{H2O} is the chamber filled with PCR brew, R_{pp1} represented the material between chamber bottom and the top of heater (CP 1), R_{pp2} is material between the heater and the heat-sink (PP 1, 2 & 3). R_{Cu} is used to represent the heat-sink. A mockup PCR cycle is simulated, and the chamber temperatures at different locations are plotted as shown in Fig. 6.2b. The time constant for the chamber is about 11 s for each step. The chamber temperature difference is less than 0.5 °C at the steady state.

Material	Density $\frac{g}{cm^3}$	Conductivity $\frac{W}{m \cdot K}$	Capacity $\frac{J}{g \cdot K}$	Thickness cm	Resistance $\frac{K}{W}$	Capacitance $\frac{J}{K}$
PMMA-chip	1.2	0.2	1.5	0.1	254.78	3.53×10^{-2}
PMMA-manifold	-	-	-	1.3	-	-
PMMA	-	-	-	0.15	-	-
pp-tape	1	0.22	1.5	0.01	23.15	2.94×10^{-3}
Heater (50 μm PI)	1	0.22	1.5	0.005	11.58	1.47×10^{-3}
water	1.0	0.67	4.2	0.05	38.03	4.12×10^{-2}
Thin Cu	9.0	400	0.4	0.03	0.038	0.02
Cu Heat-sink	-	400	0.4	0.5	0.64	0.35
$air_{convective}$-Section A, R_{air2}	-	5.6 W/m^2K	-	-	9095	-

Table 6.2: Thermal conductivity and resistivity for a 5 mm diameter chamber in vertical direction

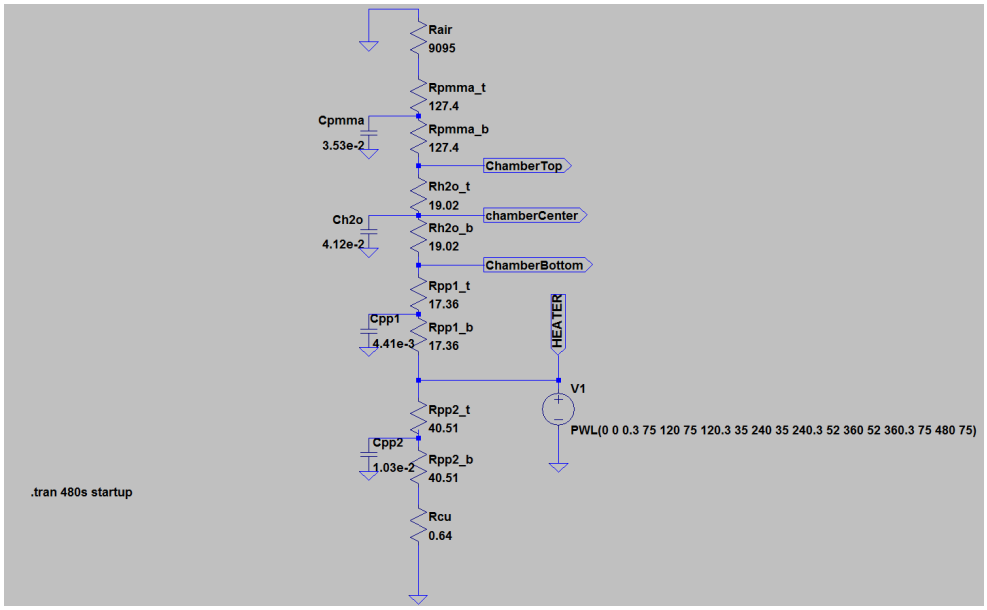

(a) LT Schematics

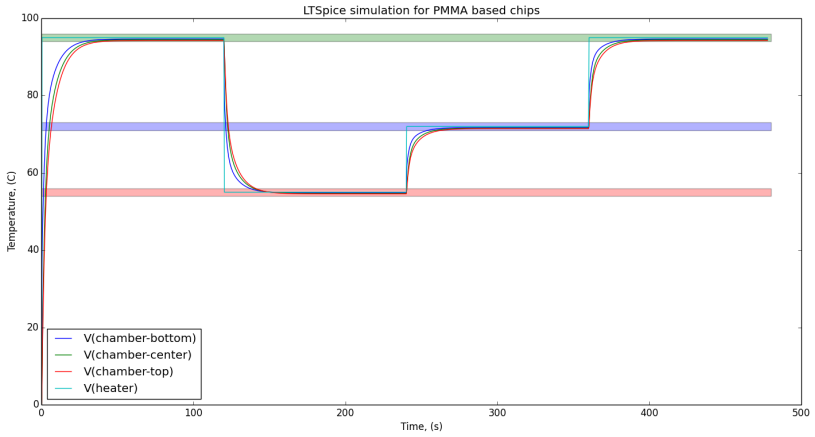

(b) LT Simulation results

Figure 6.2: LTspice simulation of vertical heat flow for section A. This demonstrates that the chamber takes 40 s to reach the linear region (or steady state). In addition, the steady state temperature for each step is within ± 1 °C of the target temperature as indicated by the light colored bands.

6.3.2 Vertical Heat Flow For Manifold

Since the manifold is still atop the chip which is in direct contact to the heater, the manifold will be heated up during the PCR process. However, the manifold does not heat as fast as the chamber since its thermal mass is much higher. We can estimate its τ, to the 1st order, by taking the product of thermal resistance and thermal conductivity. For the worst case, I can assume the manifold is a 2 inch x 1 inch x 0.5 inch (LxWxH) solid PMMA block. In the vertical direction, the τ is estimated to be 1451 s (24 minutes). As shown in the simplified equation, the τ is independent of the area. By the definition of τ, after $5\tau \approx 2$ hours the manifold reaches the equilibrium state.

$$R_{manifold} = 49.2\frac{K}{W}; \tag{6.1a}$$

$$C_{manifold} = 29.5\frac{J}{K}; \tag{6.1b}$$

$$\tau_{manifold} = 1451s \tag{6.1c}$$

Since the time constant for the manifold is about 130 times longer, the manifold temperature will be less than the chamber temperature. Also the thermal resistance of the manifold affects the temperature distribution over the chip. For a simple case, one can remove the air recess in the 1D model over the chamber and replace the water with PMMA. Since the water thermal conductivity is 3.35 times higher than PMMA, $R_{Cham} = 162.2\ \frac{K}{W}$. By adding in the $R_{manifold}$, $R_{aboveCham} = 12586\ \frac{K}{W}$. From the voltage divider equation, $T_{chambertop} = 94.0$ °C. This shows that if we wait for 2 hours, the chip under the manifold is 1.0 °C lower than the chamber at the level of the top of chamber. Further, at the top of the chip level, $R_{aboveChip} = 12330\ \frac{K}{W}$, $R_{chip} = 417\ \frac{K}{W}$. $T_{chiptop} = 92.5$ °C. So the worst case is that after 2 hrs the chip temperature under the manifold will be 2.5 °C less than the chip under recess at the top of the PMMA chip.

Since the manifold takes 2 hours to heat up, the manifold would be always at a lower temperature than the chamber during the process of PCR.

6.3.3 Vertical Heat Flow For Insulation Region

The insulation region is defined as the area between the edge of the manifold recess and the edge of the chamber. Since the heater is also under the insulation region, the 1.5

mm PMMA in the insulation region also heats up during the heating process. Due to its small thermal mass, the insulation region heats up at a much faster for the gap region is calculated to be $\tau_{1.5mmPMMA}$=20.3 °C in the vertical direction. If this region is treated as isolated from the chamber and the manifold, the surface temperature at the chip top could be calculated similarly to the chamber region. Since the vertical resistances are all inversely proportional to the surface area (both convective and conductive), we can estimate the temperature from the chamber 1D model by replacing water with PMMA. By doing this, $R_{chip} = 417\ K/W$ and $T_{chiptop} = 91.7$ °C. This means that after 100 s, the surrounding area will reach its steady state. Further, the heating from the bottom will decrease the temperature difference laterally from the chamber edge to the manifold. However, it requires a more complex model for a more realistic description of the system behavior.

6.4 Simple 2D Model

In the 1D model, I have verified the vertical temperature uniformity meets the 1C design requirement for the chamber when the chamber depth is less than 700 μm. In the horizontal direction, since the chip thickness is 1.5 mm which is the same as the gap formed between the chamber edge and the manifold. Thus, the same rule of thumb for the silicon heaters and thin tape chips can no longer be applied. In order to determine the viability in the lateral direction, I have done a series of simple BOE calculations to validate the PMMA chip design.

For simplicity, a 2D model is constructed from the chamber to the edge of the manifold as shown in Fig. 6.3. The heater is set to be a constant voltage source which is reasonable with a proper feedback control for constant temperature. In the vertical direction, we have the same drawing for the 1D model of the chamber region. In the lateral direction, we can calculate the lateral resistance of the insulation gap. Since we know the manifold heats up slowly, the temperature difference reduces with time. For the worst case, it is at the beginning of heating process where the chip and manifold are still at room temperature. So, we can assume the far end of the lateral resistance is connected to ground, which represents the room temperature (T_{room}). In the resistive network, RL_{gap} is the lateral resistance of the gap region. By using Eq. 4.1b, the lateral thermal resistance from the chamber edge to the edge of the manifold is found to be 249 $\frac{K}{W}$ if we consider the total thickness of the chip.

Due to high thermal conductivity of water, we can further simplify the system by replacing the chamber with a node in the system as shown in Fig. 6.4. The thin Cu layer

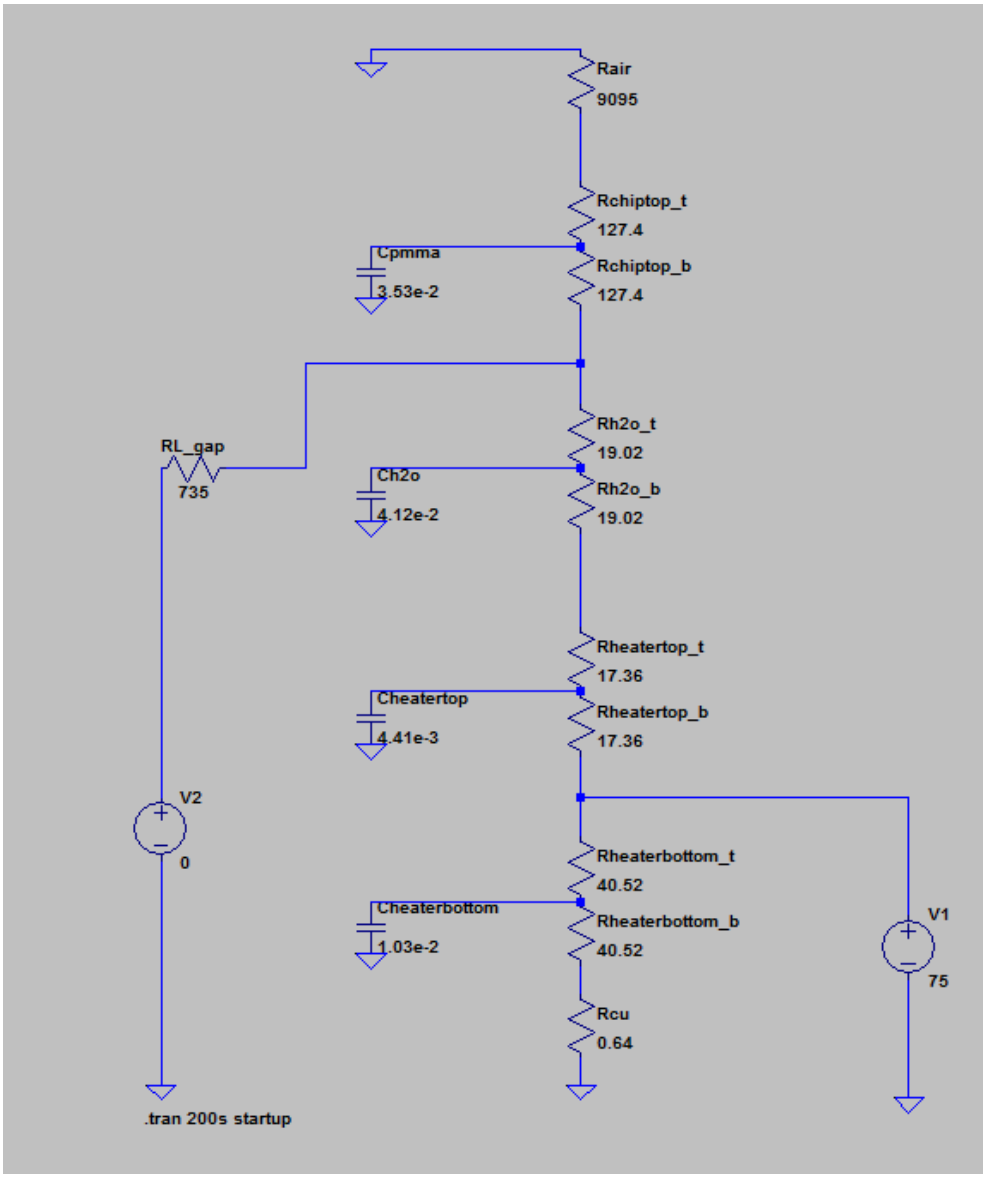

Figure 6.3: Simple 2D LTspice model

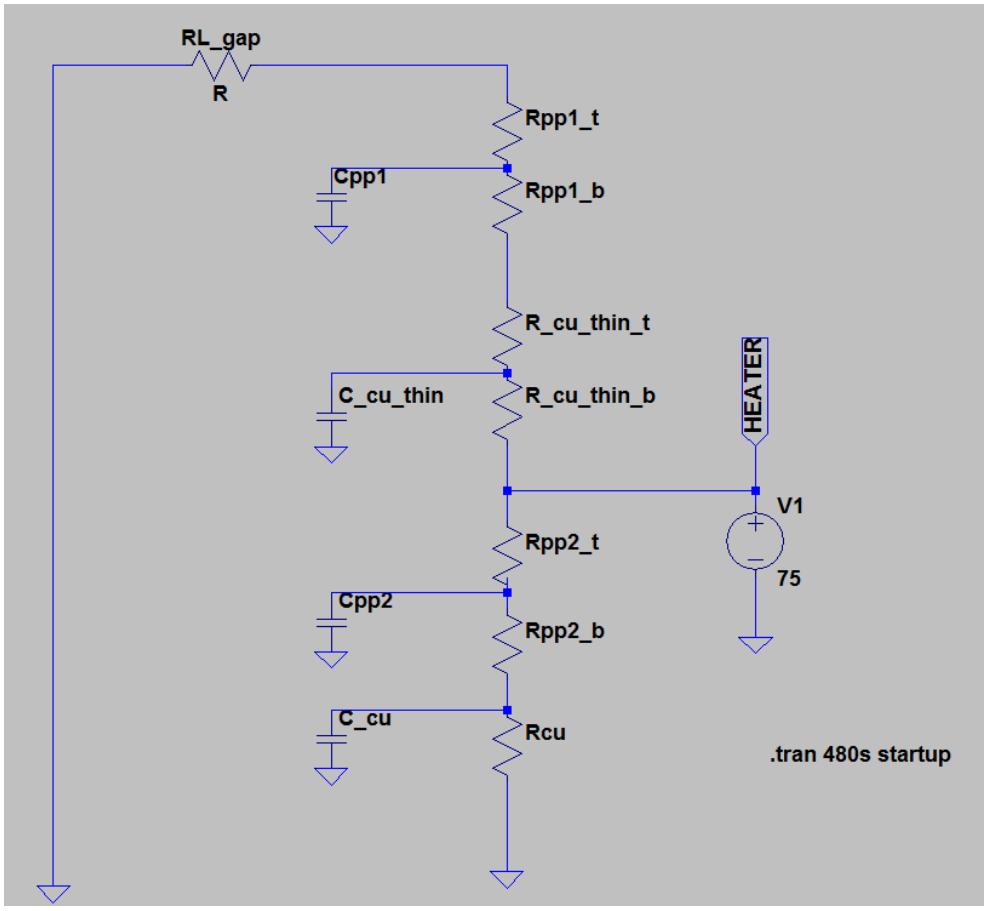

Figure 6.4: Further simplified 2D LTspice schematic

atop the heater could be treated as a uniform temperature region, which is heating the chip above. So, we used the spreading region radius, r_{Cu}=3.25 mm, for calculating the vertical resistance of the interfacing layer, $R_{pp1} = 22.6\ \frac{K}{W}$. From the voltage divider equation, we can find that the temperature at the edge of the chamber is $T_{chamber-edge} = 68.7$ °C above T_{room}, during the denaturing process. This is 6.2 °C less than the bottom of the chamber. It does not meet the target specifications of the system.

$$T_{chamber-edge} = 75\frac{RL_{gap}}{RL_{gap} + R_{pp1}} = 68.7°C \tag{6.2}$$

However, if we reduce the chamber radius to 1 mm, the lateral resistance will increase to 735 K/W. The interface resistance does not change since r_{Cu} is same. As a result,

the temperature at the edge of the chamber changed to $T_{chamber-edge} = 72.8$ °C above T_{room}. The variation reduces by almost 3 times and becomes 2.2 °C less than the chamber bottom. Therefore, if the chamber radius is reduced from 2.5 mm to 1 mm, the chamber edge temperature will only be 2.2 °C lower for the worst case scenario.

However, in reality, the heater is under the chamber, manifold and the insulation region. Therefore the insulation region is not only heated from one heater source, but a series of small heater elements directly under them. The temperature change will never be more than the calculated values. Therefore, it is certain that we have no temperature variation more than 2.2 °C at Th=95 °C. Similarly, the difference is about 1.0 °C at Th=55 °C.

In addition to reducing the chamber radius, I can also reduce the chip thickness in the insulation region. By reducing the thickness by 50 %, the lateral resistance increases by a factor of two. By applying the same calculation earlier, the chamber temperature varies 1.1 °C at Th=95 °C (or 0.5 °C at Th=55 °C).

$$R_L = \frac{1}{2\pi kd} \ln \frac{4}{2.5} = 249 \frac{K}{W}; \tag{6.3a}$$

In summary, from the simple 2D representation for the chamber and surrounding area, the chamber temperature variation is estimated for the PCR process. As mentioned through this section, the estimated results are very crude approximations for the system in its worst possible scenario. From these results, I believe that if we reduce the chamber radius to 1 mm, the chamber temperature variation is less than 1.0 °C during the annealing step (or 2.2 °C during the denature step). In addition, this variation can be further reduced to 0.5 °C by thinning the insulation area to 0.7 mm.

6.5 Requested 3D Time-domain Simulation

In order to further validate the heater system, a 3D time-domain simulation was requested to study the heat transfer of the system. The boundary conditions are specified in detail in this section. Then, I will list the requested measurements in order to study the system.

6.5.1 Boundary Conditions And Assumptions

In terms of boundary conditions, the surrounding room temperature is set to be 20 °C. Similar to the earlier design, the Robin condition is applied to the top surface of the

PMMA manifold and the outside of the manifold (right edge) with a constant convective heat transfer. The heat-sink is modeled by a thin surface with a Dirichlet condition, which is kept at room temperature. By assuming cylindrical symmetry, a Neumann boundary condition is applied to the right boundary. However, since there is no pressurized chamber above the membrane, the membrane and the chamber are exposed to the ambient air. Thus, the Robin condition with convective heat loss is applied to the top of the membrane layer and the inside of the manifold. Fig. 6.5

Inside the heater region, a constant power density is applied to the heater layer. The thermocouple and the Cu insert are treated as a uniform Cu structure. The

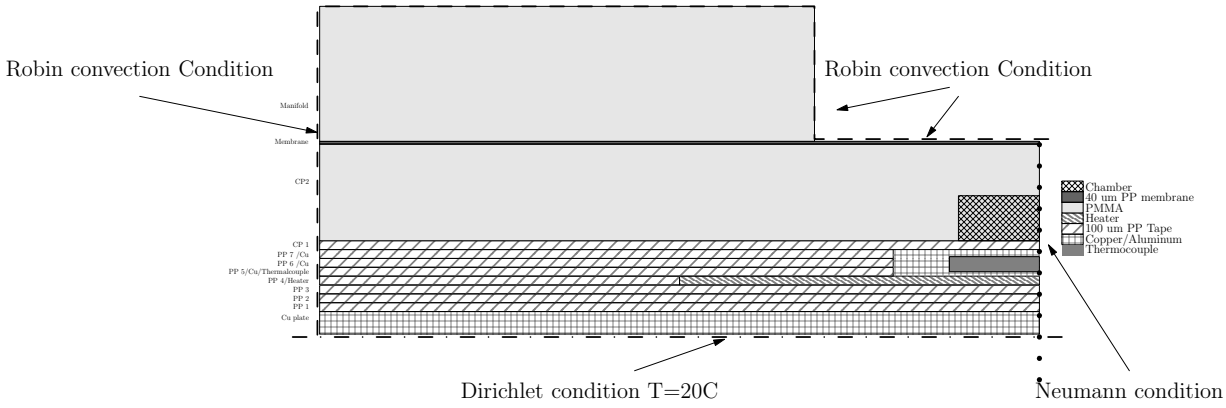

Figure 6.5: The requested boundary conditions of the 3D simulation.

6.5.2 Requested Measurements

In order to study the behavior of the system, several measurements are required from the simulation results.

Firstly, a surface profile measurement is applied to the top surface of the Cu insert. By measuring the temperature profile along the top surface of the Cu, the temperature uniformity can be estimated. Thus, any lateral flow could be visualized as in the previous chapter.

Secondly, the average temperature of the chamber and the Cu are required. Since the feedback control is based on the measurement of the embedded thermocouple, the average temperature of the Cu insert could be used to represent the thermocouple temperature. By

comparing these two average temperatures, the correlation between the chamber temperature and the thermocouple temperature could be verified and estimated for better heat control.

Thirdly, the maximum temperature variation inside the chamber is measured. The maximum variation is determined by subtracting the minimum temperature from the maximum temperature inside the chamber region. This maximum temperature variation is used to determine the temperature uniformity inside the chamber region.

6.6 Experimental Results

Preliminary Experimental results had shown successful PCR amplification on chip with the discrete heater system by my colleagues Gordon Hall and Maddie Couse. PCR chambers of 1.6 mm radius and 0.5 mm deep were tested with the HFE exon 2 PCR protocol. [60] The chamber was either laser ablated or milled by a CNC machine without any channel or wells. The PCR brew was manually loaded into each chamber and capped with a small piece of the PCR tape. The PCR thermal cycling program was modified from the one used on a regular PCR machine as shown in Table 6.3. 30 seconds were added to each step due to the time constant of the fluid in the chamber. After PCR, the product was loaded onto an agarose CE chip and verified with CE on the μTK. Two out of the total three preliminary tests were successful, as shown in Fig. 6.6. The failed test was likely due to the use of the original PCR thermal program without the additional time.

As shown in Fig. 6.6, successful PCR tests were demonstrated on chips with different fabrication processes. The red line represents the 2nd test on a milled chip. For the red line, all peaks shifted to the left compared to the conventional product. This could be caused by the changes in the buffer concentration due to the recovery process from the chamber. However, the distance between the product (3rd) and primer (1st) peaks was the same as for the conventional PCR product. The 2nd peak on the red line is the primer dimer, which likely indicated the chamber temperature was slightly less than 65 °C during annealing. This agrees with the numerical analysis in an earlier section that the chamber temperature is about 2 °C less than the heater. The green line is the PCR product from a laser fabricated chip. During that CE process, the agarose broke into pieces inside the channel. Thus, the arrival time and separation distance were not comparable to other runs. However, it does show that amplification of DNA took place. The 3rd peak after the dimer peak in the green line is likely the result of unpredicted program failure halfway the PCR process, forcing the operator to restart the PCR program in the middle of the run. Even though these runs were not as good as the conventional PCR results, the demonstration

of PCR amplification on this preliminary system is a major step forward towards the fully integrated PCR-CE system.

		Temperature (°C)	Time (s)
	Activation	95	120
35×	Denature	95	40 (20)
	Annealing	65	50 (30)
	Elongation	72	50 (30)

Table 6.3: Modified PCR thermal cycling program for on chip PCR. The program was modified from the original protocol (shown in brackets) used for HFE exon 2.

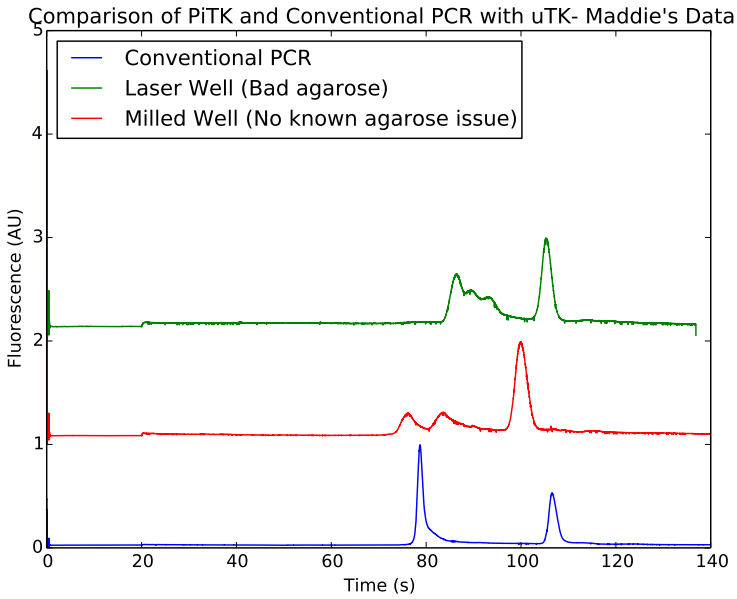

Figure 6.6: Electropherogram of the PCR products in agarose CE chips (Maddie Couse). The CE condition used was the same as the 2 % agarose CE described in Chapter 2. The blue line is the CE results of the conventional PCR; the red line is the 2nd test on milled chip; the green line is the PCR product from a laser fabricated chip. All three products showed successful PCR amplification. For the red line, all peaks shifted to the left comparing to the conventional product. This could be caused by changes in the buffer concentration due to the recovery process. However, the distance between the product and primer peak is the same as the blue line. The 2nd peak on the red line is the primer dimer which likely indicated the chamber temperature was slightly less than 65 °C.The green is comparable although this analysis was complicated by apparent fracture in the loaded agarose and interrupted PCR.

6.7 Future Chip Designs

6.7.1 PCR-RFLP Chip

As mentioned at the beginning of this chapter, one advantage of the PMMA based chip is that the PCR module is built upon the same substrate used for the auto-RFLP system. By combining the PCR chip with the Auto-RFLP chip, we have developed a fully integrated PCR-RFLP design for the PMMA chip as shown in Fig. 6.7.

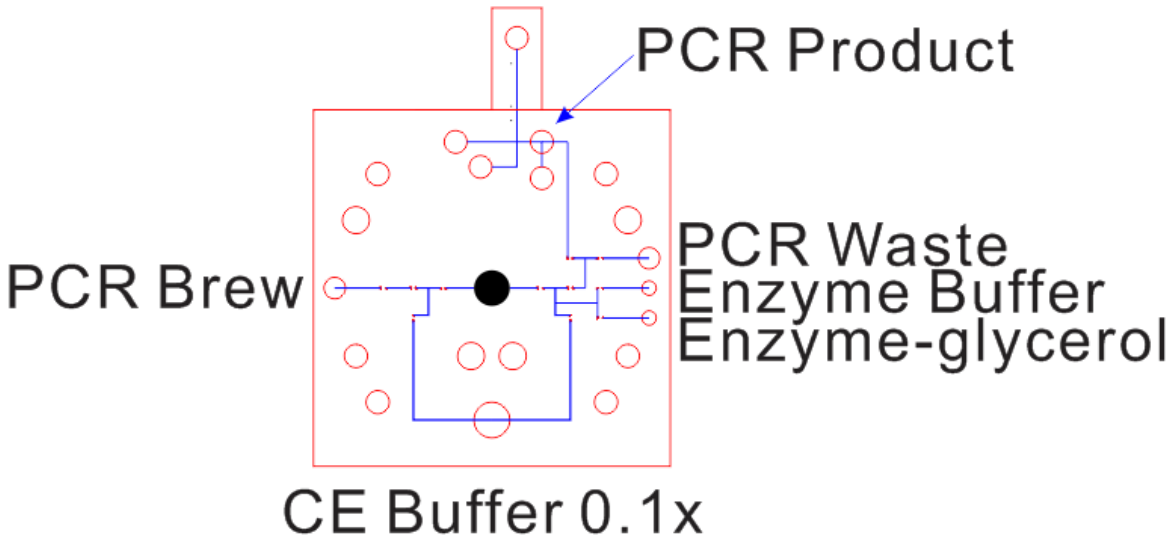

Figure 6.7: Top down of the PCR-RFLP chip

6.8 Conclusion

To conclude, a rigid 1.5 mm PMMA based integrated PCR-CE system design is presented in this chapter. From the 1D and simple 2D analytical analysis, I validated the temperature uniformity and thermal response time for the heater system. The 3D simulation was requested for additional validation. In addition, a PCR protocol for the exon 2 of HFE gene had been verified for a wide range of the annealing temperature. Thus, simple test chips

were tested with this PCR protocol on the discrete heater system by my colleagues. The successful amplification of the target DNA agrees with the analytical results. Furthermore, an integrated PCR-RFLP chip design is presented with proven valving and RFLP modules. However, the successful amplification is based on the high tolerance of the HFE exon 2 PCR protocol. Therefore, the 3D simulation is needed to further understand the system. In the future, a general PCR protocol with 1 degree temperature tolerance should be tested to prove the capability of the heater system.

Chapter 7

Conclusion And Future Directions

7.1 Conclusion And Future Directions

In this thesis, I have developed an improved fabrication protocol for the laser-ablated PMMA-based CE chip. This protocol has been used to fabricate and demonstrate on chip CE performance similar to that reported in the literature and previous work in our group.

Various designs for electrophoresis, fluidic control (e.g., valve, helper chip) and thermal control (e.g., the Si heater, discrete heater systems) have been developed. These were tested individually and in some integration (e.g., the auto-RFLP CE demonstration).

In addition, I have proved the concept of a CMOS-compatible PCR module, which requires no device calibration in the joint-project with the University of Alberta. However, the silicon heater experienced a number of issues that prevent us from further experiments.

For future work, the requested 3D simulation is necessary to further validate the improved discrete heater system. Even though the preliminary PCR results of the discrete system are successful, it is based on a specially chosen PCR protocol for HFE exon 2 that has a high temperature tolerance. Thus, the demonstration of the heater system with a general PCR protocol, such as the HFE exon 4 PCR protocol, is essential for expanding the system application. Furthermore, the experimental demonstration of the heater system with other modules in a fully integrated manner is an easily achievable milestone and necessary for clinical applications (e.g., HFE). For the Si heater, it is critical to find the reason for erratic fabrication results and finalize a reproducible fabrication protocol.

In terms of future improvement, all of these designs were intended to be developed in a manner that could be implemented in a PMMA chip or on a future CMOS chip. At present, the CMOS technology of Teledyne DALSA is capable of incorporating all of this functionality, although valving will require further development. In the interim, the slight modification to the current design can provide either an all-PMMA sample preparation-PCR-CE solution or a 'helper-chip'/intelligent packaging on a CMOS chip.

APPENDICES

Appendix A

The Si Heater

A.1 Amscope Camera Setting For Image Acquisition

The Toupview is the provided image capture software for the Amscope camera. In order to eliminate any auto-correction functions, the following settings were applied for all the RhB fluorescence measurements.

1. Color setting (Default):
   (a) Temperature= 6503;
   (b) Tine = 1000;
   (c) Hue = 1000;
   (d) Saturation = 128;
   (e) Bright = 0;
   (f) Contrast = 0;
   (g) Gamma = 100;
2. Exposure (Default, auto-exposure off):
   (a) Exposure Time = 200ms;
   (b) Gain = 3.0;
   (c) Amount = 0;
   (d) Midpoint = 50;
3. Histogram (Default):
   (a) left = 0;
   (b) right = 255;

A.2 Sample Python Script

A.2.1 Heater Control Program

This heater control program is modified from the current control script by Gordon Hall at the UofW.

```
# This program sets the current from 1 mA to current max mA at
    ti5me2 second intervals while measuring the voltage over a
    resistor. It then steps down by a factor of 2 for time2 second
     interval 3 times
##Filename
#datafilename = 'RhodamineB_Test1.txt'


#Initialising Labjack Variables

#Import the U6 library
import u6
#Import the time library, used for determining the current time
import time
from time import gmtime, strftime
#Import the sys library, used for error reporting
import sys
#Import numpy, math libraries for easier calculations
import numpy as n

#Initialize LabJack
d = u6.U6()

#Filename
datafilename = 'FieldsMetal-250mA200sec'+'Chip4-1_Round2'+
    strftime("-%Y%m%d-%H%M%S", gmtime())+'.txt'

#Define DAC channels

#Heater current source control with DAC0
heater_dac = 5000

#Lock-in offset voltage control with DAC1
li_offset = 5002

#Define DIO channels

#LED control with FIO0 and FIO1
```

```
led_dio = 6000
led_dio1 = 6001

#Relay control with CIO0-CIO3
relay_1 = 6016
relay_2 = 6017
relay_3 = 6018
relay_4 = 6019

#Solenoid Valve control with EIO0-EIO7
sv_1 = 6008
sv_2 = 6009
sv_3 = 6010
sv_4 = 6011
sv_5 = 6012
sv_6 = 6013
sv_7 = 6014
sv_8 = 6015

#Solenoid Valve control with FIO2-FIO6
sv_9 = 6002
sv_10 = 6003
sv_11 = 6004
sv_12 = 6005
sv_13 = 6006

#FIO7 (Register 6007) unassigned but connected on board

#Define AIN channels

#Hamamatsu AIN (AIN12)
ham_v = 24

#Lock-in 1 out
li1_out = 4

#Lock-in 1 1-stage out
li1_1s_out = 6
```

```
#Lock-in 2 out
li2_out = 8

#Lock-in 2 1-stage out
li2_1s_out = 10

#Unassigned: AIN6 (Register 12) and AIN7 (Register 14) but
   connected on board
#Not connected: AIN8, AIN9, AIN10, AIN11 and AIN13. Can be
   accessed by soldering a jumper wire to the appropriate DB37
   pin.

current_plus = 14

#heater voltage drop = AIN0/AIN1 in differential mode
#Condition Ain 0, 3, 5, 7 properly (Single Ended, Max Resolution,
    Minimum Gain)
d.writeRegister(3000, 1)
d.writeRegister(3002,1)
d.writeRegister(3005,199)
d.writeRegister(3007,199)
d.writeRegister(1000,8)
d.writeRegister(1003,8)
d.writeRegister(1005,8)
d.writeRegister(1007,8)
d.writeRegister(1500,0)
d.writeRegister(1501,0)
d.writeRegister(1503,0)
d.writeRegister(1505,0)
d.writeRegister(1507,0)

#Assign heater_v as 0; d.readRegister(heater_v) will read AIN0/
   AIN1 differential voltage
heater_v = 0

#Counter for printing on screen
print_increment = 0
```

```
print_up_increment = 0
print_down_increment = 0
print_frequency = 1

#File I/O
datafile = open(datafilename, 'w')
datafile.write('Time (s)'+'\t'+'Set Current (mA)' + '\t' + '
   Measured Current (A)' + '\t' + 'Voltage (V)'+'\t' + '
   Resistance (Ohm)' + '\n')


#Begin Code
time2=4
time3=200 #the holding time for the heater
#time4=0
timestep=time2
run_time=time.clock()
maxcurrent=250**2 #maximum current setting
currentstep=maxcurrent/20
mAcurrents= range(0,maxcurrent+currentstep,currentstep)
heater_voltage=0
d.writeRegister(6013,1)
# For two current sources find
try:
        while heater_voltage<20:
                run_time = time.clock()
                #d.writeRegister(6013,1)
                if run_time > print_increment+0.99:
                        print 'Time: {time}'.format(time =
                           run_time)
                        print_increment = print_increment+
                           print_frequency

                for w in mAcurrents:
                        while run_time<time2:
                                run_time = time.clock()
                                DACcurrent=(float(w)**0.5)/300
```

```
                        d.writeRegister(heater_dac,
                            DACcurrent)
                        heater_voltage = d.getAIN
                            (0,8,0,9,1)*10
                        measure_current=d.getAIN
                            (2,8,0,9,1)/10
                        R=heater_voltage/measure_current
                        print 'Time: {time3} s, Set
                            Current: {c_dac} mA, Measured
                            Current: {mcur} A, Voltage: {
                            voltage} V, Resistance: {RES}
                            Ohm'.format(time3 = run_time,
                            c_dac = DACcurrent*300, mcur=
                            measure_current, voltage =
                            heater_voltage, RES=R)

                        datafile.write(str(run_time)+'\t
                            '+str(DACcurrent*300) + '\t' +
                             str(measure_current) + '\t' +
                             str(heater_voltage)+ '\t' +
                            str(R)+'\n')
            time2=time2+timestep
#?????
#d.writeRegister(heater_dac,DACcurrent)
#heater_voltage = d.getAIN(0,8,0,9,1)*10
#measure_current=d.getAIN(2,8,0,9,1)/10
#R=heater_voltage/measure_current
#print 'Time: {time3} s, Set Current: {c_dac} mA,
    Measured Current: {mcur} A, Voltage: {voltage
   } V, Restistance: {RES} Ohm'.format(time3 =
   run_time, c_dac = DACcurrent*300, mcur=
   measure_current, voltage = heater_voltage, RES
   =R)
#datafile.write(str(run_time)+'\t'+str(w) + '\t'
   + str(measure_current) + '\t' + str(
   heater_voltage)+ '\t' + str(R) + '\n')
# holding the heater for time3 and do scaning
time4 = time2+time3
```

```
while run_time<time4:
        run_time = time.clock()
        d.writeRegister(heater_dac,DACcurrent)
        heater_voltage = d.getAIN(0,8,0,9,1)*10
        measure_current=d.getAIN(2,8,0,9,1)/10
        R=heater_voltage/measure_current
        print 'Time: {time3} s, Set Current: {
           c_dac} mA, Measured Current: {mcur} A,
            Voltage: {voltage} V, Restistance: {
           RES} Ohm'.format(time3 = run_time,
           c_dac = DACcurrent*300, mcur=
           measure_current, voltage =
           heater_voltage, RES=R)
        datafile.write(str(run_time)+'\t'+str(
           DACcurrent*300) + '\t' + str(
           measure_current) + '\t' + str(
           heater_voltage)+ '\t' + str(R) + '\n')
time2 =time4

for r in range(1,20,1):
        while run_time<time2:
                run_time = time.clock()
                DACcurrent=(float(mAcurrents[-1])
                   **0.5)/(float(r)*300)
                d.writeRegister(heater_dac,
                   DACcurrent)
                heater_voltage =d.getAIN
                   (0,8,0,9,1)*10
                measure_current=d.getAIN
                   (2,8,0,9,1)/10
                R=heater_voltage/measure_current
                print 'Time: {time3} s, Set
                   Current: {c_dac} mA, Measured
                   Current: {mcur} A, Voltage: {
                   voltage} V, Resistance: {RES}
                   Ohm'.format(time3 = run_time,
                   c_dac = DACcurrent*300, mcur=
```

```
                                measure_current, voltage =
                                heater_voltage, RES=R)

                            datafile.write(str(run_time)+'\t
                               '+str(DACcurrent*300) + '\t' +
                                str(measure_current) + '\t' +
                                str(heater_voltage)+ '\t' +
                                str(R)+'\n')
                        time2=time2+timestep



                    d.writeRegister(heater_dac, 0)
                    d.writeRegister(led_dio1, 0)
                    datafile.close()
                    break


#Press ctrl+c to emergency stop the program
#If you stopped the program any other way, copy and paste these
   commands into the command line
except KeyboardInterrupt:
    print 'Keyboard Interrupt. Program Stopped.'
    d.writeRegister(heater_dac, 0)
    d.writeRegister(led_dio1, 0)
    datafile.close()
    #PDdatafile.close()
    #Hdatafile.close()

#In case on unexpected error, the error is reported and the
   program is stopped
except:
    print 'Unexpected Error. Program Stopped.'
    print sys.exc_info()
    d.writeRegister(heater_dac, 0)
    d.writeRegister(led_dio1, 0)
    datafile.close()
    #PDdatafile.close()
```

```
#Hdatafile.close()
```

References

[1] Geert Jannes and Daniel De Vos. A review of current and future molecular diagnostic tests for use in the microbiology laboratory. *Methods in molecular biology (Clifton, N.J.)*, 345:1–21, January 2006. ISSN 1064-3745. doi: 10.1385/1-59745-143-6:1. URL http://www.ncbi.nlm.nih.gov/pubmed/16957343.

[2] Curtis D Chin, Vincent Linder, and Samuel K Sia. Lab-on-a-chip devices for global health: past studies and future opportunities. *Lab on a chip*, 7(1):41–57, January 2007. ISSN 1473-0197. doi: 10.1039/b611455e. URL http://www.ncbi.nlm.nih.gov/pubmed/17180204.

[3] S J Lee and S Y Lee. Micro total analysis system (micro-TAS) in biotechnology. *Applied microbiology and biotechnology*, 64(3):289–99, April 2004. ISSN 0175-7598. doi: 10.1007/s00253-003-1515-0. URL http://www.ncbi.nlm.nih.gov/pubmed/14714150.

[4] A. Manz, N. Graber, and H.M. Widmer. Miniaturized total chemical analysis systems: A novel concept for chemical sensing. *Sensors and Actuators B: Chemical*, 1(1-6): 244–248, January 1990. ISSN 09254005. doi: 10.1016/0925-4005(90)80209-I. URL http://linkinghub.elsevier.com/retrieve/pii/092540059080209I.

[5] Thomas Ming-Hung Lee and I-Ming Hsing. DNA-based bioanalytical microsystems for handheld device applications. *Analytica chimica acta*, 556(1):26–37, January 2006. ISSN 1873-4324. doi: 10.1016/j.aca.2005.05.075. URL http://www.ncbi.nlm.nih.gov/pubmed/17723328.

[6] Michelle L Kovarik, Philip C Gach, Douglas M Ornoff, Yuli Wang, Joseph Balowski, Lila Farrag, and Nancy L Allbritton. Micro total analysis systems for cell biology and biochemical assays. *Analytical chemistry*, 84(2):516–40, January 2012. ISSN 1520-6882. doi: 10.1021/ac202611x. URL http://www.pubmedcentral.nih.gov/articlerender.fcgi?artid=3264799&tool=pmcentrez&rendertype=abstract.

[7] Pamela N Nge, Chad I Rogers, and Adam T Woolley. Advances in microfluidic materials, functions, integration, and applications. *Chemical reviews*, 113(4):2550–83, May 2013. ISSN 1520-6890. doi: 10.1021/cr300337x. URL http://www.ncbi.nlm.nih.gov/pubmed/23410114.

[8] Samuel K Njoroge, Hui-Wen Chen, Magorzata A Witek, and Steven A Soper. Integrated microfluidic systems for DNA analysis. *Topics in current chemistry*, 304: 203–60, January 2011. ISSN 0340-1022. doi: 10.1007/128_2011_153. URL http://www.ncbi.nlm.nih.gov/pubmed/21607848.

[9] Amir M Foudeh, Tohid Fatanat Didar, Teodor Veres, and Maryam Tabrizian. Microfluidic designs and techniques using lab-on-a-chip devices for pathogen detection for point-of-care diagnostics. *Lab on a chip*, 12(18):3249–66, September 2012. ISSN 1473-0189. doi: 10.1039/c2lc40630f. URL http://www.ncbi.nlm.nih.gov/pubmed/22859057.

[10] Farhan Ahmad and Syed A. Hashsham. Miniaturized nucleic acid amplification systems for rapid and point-of-care diagnostics: a review. *Analytica chimica acta*, 733:1–15, July 2012. ISSN 1873-4324. doi: 10.1016/j.aca.2012.04.031. URL http://linkinghub.elsevier.com/retrieve/pii/S0003267012006265http://www.ncbi.nlm.nih.gov/pubmed/22704369.

[11] David R Almassian, Lisa M Cockrell, and William M Nelson. Portable nucleic acid thermocyclers. *Chemical Society reviews*, 42(22):8769–98, October 2013. ISSN 1460-4744. doi: 10.1039/c3cs60144g. URL http://www.ncbi.nlm.nih.gov/pubmed/24030680.

[12] Stephen A Bustin, Vladimir Benes, Jeremy A Garson, Jan Hellemans, Jim Huggett, Mikael Kubista, Reinhold Mueller, Tania Nolan, Michael W Pfaffl, Gregory L Shipley, Jo Vandesompele, and Carl T Wittwer. The MIQE guidelines: minimum information for publication of quantitative real-time PCR experiments. *Clinical chemistry*, 55 (4):611–22, April 2009. ISSN 1530-8561. doi: 10.1373/clinchem.2008.112797. URL http://www.ncbi.nlm.nih.gov/pubmed/19246619.

[13] Sara Huston Katsanis and Nicholas Katsanis. Molecular genetic testing and the future of clinical genomics. *Nature reviews. Genetics*, 14(6):415–26, June 2013. ISSN 1471-0064. doi: 10.1038/nrg3493. URL http://www.ncbi.nlm.nih.gov/pubmed/23681062.

[14] Tianchi Ma, Victoria Northrup, Andrew O. Fung, D. Moira Glerum, and Christopher J. Backhouse. Polymeric rapid prototyping for inexpensive and portable medical diagnostics. In Jean-Claude Kieffer, editor, *SPIE Photonic North 2012*, volume 8412, page 84120B, October 2012. doi: 10.1117/12.2001470. URL http://proceedings.spiedigitallibrary.org/proceeding.aspx?doi=10.1117/12.2001470.

[15] Dammika P Manage, Duncan G Elliott, and Christopher J Backhouse. Millimeter scale separation of DNA with a replaceable polymer matrix. *Electrophoresis*, 33(21): 3213–21, November 2012. ISSN 1522-2683. doi: 10.1002/elps.201200188. URL http://www.ncbi.nlm.nih.gov/pubmed/23027089.

[16] Martin F Jensen, John E McCormack, Bjarne Helbo, Leif H Christensen, Thomas R Christensen, and Oliver Geschke. Rapid prototyping of polymer microsystems via excimer laser ablation of polymeric moulds. *Lab on a chip*, 4(4):391–5, August 2004. ISSN 1473-0197. doi: 10.1039/b403037k. URL http://www.ncbi.nlm.nih.gov/pubmed/15269810.

[17] Wilhelm Pfleging, Robert Kohler, Phillip Schierjott, and Werner Hoffmann. Laser patterning and packaging of CCD-CE-Chips made of PMMA. *Sensors and Actuators B: Chemical*, 138(1):336–343, April 2009. ISSN 09254005. doi: 10.1016/j.snb.2009.01.036. URL http://linkinghub.elsevier.com/retrieve/pii/S0925400509000616.

[18] Kevin D. Dorfman. DNA electrophoresis in microfabricated devices. *Reviews of Modern Physics*, 82(4):2903–2947, October 2010. ISSN 0034-6861. doi: 10.1103/RevModPhys.82.2903. URL http://link.aps.org/doi/10.1103/RevModPhys.82.2903.

[19] A P Lewis, A Cranny, N R Harris, N G Green, J A Wharton, R J K Wood, and K R Stokes. Review on the development of truly portable and in-situ capillary electrophoresis systems. *Measurement Science and Technology*, 24(4):042001, April 2013. ISSN 0957-0233. doi: 10.1088/0957-0233/24/4/042001. URL http://stacks.iop.org/0957-0233/24/i=4/a=042001?key=crossref.993fab7451a5d531cdd7fa544943a462.

[20] Gaozhi Ou, Xiaojun Feng, Wei Du, Xin Liu, and Bi-Feng Liu. Recent advances in microchip electrophoresis for amino acid analysis. *Analytical and bioanalytical chemistry*, 405(25):7907–18, October 2013. ISSN 1618-2650. doi: 10.1007/s00216-013-6830-4. URL http://www.ncbi.nlm.nih.gov/pubmed/23436170.

[21] Henning Klank, Jorg P Kutter, and Oliver Geschke. CO(2)-laser micromachining and back-end processing for rapid production of PMMA-based microfluidic systems. *Lab on a chip*, 2(4):242–6, November 2002. ISSN 1473-0197. doi: 10.1039/b206409j. URL http://www.ncbi.nlm.nih.gov/pubmed/15100818.

[22] Robert S. Dubrow. Method And Compositions For Performing Molecular Separations, 2000.

[23] Heng Qi, Xiansong Wang, Tao Chen, Xuemei Ma, and Tiechuan Zuo. Fabrication and characterization of a polymethyl methacrylate continuous-flow PCR microfluidic chip using CO2 laser ablation. *Microsystem Technologies*, 15(7):1027–1030, April 2009. ISSN 0946-7076. doi: 10.1007/s00542-009-0843-0. URL http://link.springer.com/10.1007/s00542-009-0843-0.

[24] Chunsun Zhang and Da Xing. Miniaturized PCR chips for nucleic acid amplification and analysis: latest advances and future trends. *Nucleic acids research*, 35(13):4223–37, January 2007. ISSN 1362-4962. doi: 10.1093/nar/gkm389. URL http://www.pubmedcentral.nih.gov/articlerender.fcgi?artid=1934988&tool=pmcentrez&rendertype=abstract.

[25] Yi Sun, Yien Chian Kwok, and Nam-Trung Nguyen. Low-pressure, high-temperature thermal bonding of polymeric microfluidic devices and their applications for electrophoretic separation. *Journal of Micromechanics and Microengineering*, 16(8):1681–1688, August 2006. ISSN 0960-1317. doi: 10.1088/0960-1317/16/8/033. URL http://stacks.iop.org/0960-1317/16/i=8/a=033?key=crossref.9fe9e53b133b353274eebdc1a411129a.

[26] D L Pugmire, E A Waddell, R Haasch, M J Tarlov, and L E Locascio. Surface characterization of laser-ablated polymers used for microfluidics. *Analytical chemistry*, 74(4):871–8, February 2002. ISSN 0003-2700. URL http://www.ncbi.nlm.nih.gov/pubmed/11866067.

[27] Ji-Yen Cheng, Cheng-Wey Wei, Kai-Hsiung Hsu, and Tai-Horng Young. Direct-write laser micromachining and universal surface modification of PMMA for device development. *Sensors and Actuators B: Chemical*, 99(1):186–196, April 2004. ISSN 09254005. doi: 10.1016/j.snb.2003.10.022. URL http://linkinghub.elsevier.com/retrieve/pii/S0925400503007871.

[28] C. J. Backhouse, H. J. Crabtree, and D. M. Glerum. Frontal analysis on a microchip. *The Analyst*, 127(9):1169–1175, September 2002. ISSN 00032654. doi: 10.1039/b203515d. URL http://xlink.rsc.org/?DOI=b203515d.

[29] Dammika P. Manage, Yuen C. Morrissey, Alexander J. Stickel, Jana Lauzon, Alexey Atrazhev, Jason P. Acker, and Linda M. Pilarski. On-chip PCR amplification of genomic and viral templates in unprocessed whole blood. *Microfluidics and Nanofluidics*, 10(3):697–702, October 2010. ISSN 1613-4982. doi: 10.1007/s10404-010-0702-4. URL http://link.springer.com/10.1007/s10404-010-0702-4.

[30] JC Bowman and A Hammerlindl. Asymptote: A vector graphics language. *TUGboat: The Communications of the TEX Users ...*, 2008. URL http://scholar.google.com/scholar?hl=en&btnG=Search&q=intitle:Asymptote+:+the+Vector+Graphics+Language#0http://scholar.google.com/scholar?hl=en&btnG=Search&q=intitle:Asymptote:+A+vector+graphics+language#0.

[31] Yun Chen, Luyan Zhang, and Gang Chen. Fabrication, modification, and application of poly(methyl methacrylate) microfluidic chips. *Electrophoresis*, 29(9):1801–14, May 2008. ISSN 0173-0835. doi: 10.1002/elps.200700552. URL http://www.ncbi.nlm.nih.gov/pubmed/18384069.

[32] Chia-Wen Tsao and Don L. DeVoe. Bonding of thermoplastic polymer microfluidics. *Microfluidics and Nanofluidics*, 6(1):1–16, November 2008. ISSN 1613-4982. doi: 10.1007/s10404-008-0361-x. URL http://link.springer.com/10.1007/s10404-008-0361-x.

[33] L Martynova, L E Locascio, M Gaitan, G W Kramer, R G Christensen, and W a MacCrehan. Fabrication of plastic microfluid channels by imprinting methods. *Analytical chemistry*, 69(23):4783–9, December 1997. ISSN 0003-2700. URL http://www.ncbi.nlm.nih.gov/pubmed/9406529.

[34] Michelle Galloway, Wieslaw Stryjewski, Alyssa Henry, Sean M Ford, Shawn Llopis, Robin L McCarley, and Steven a Soper. Contact conductivity detection in poly(methyl methacrylate)-based microfluidic devices for analysis of mono- and polyanionic molecules. *Analytical chemistry*, 74(10):2407–15, May 2002. ISSN 0003-2700. URL http://www.ncbi.nlm.nih.gov/pubmed/12038768.

[35] Xuelin Zhu, Gang Liu, Yuhua Guo, and Yangchao Tian. Study of PMMA thermal bonding. *Microsystem Technologies*, 13(3-4):403–407, June 2006. ISSN 0946-7076. doi: 10.1007/s00542-006-0224-x. URL http://link.springer.com/10.1007/s00542-006-0224-x.

[36] Jayna J Shah, Jon Geist, Laurie E Locascio, Michael Gaitan, Mulpuri V Rao, and Wyatt N Vreeland. Capillarity induced solvent-actuated bonding of polymeric mi-

crofluidic devices. *Analytical chemistry*, 78(10):3348–53, May 2006. ISSN 0003-2700. doi: 10.1021/ac051883l. URL http://www.ncbi.nlm.nih.gov/pubmed/16689536.

[37] Yi-Chu Hsu and Tang-Yuan Chen. Applying Taguchi methods for solvent-assisted PMMA bonding technique for static and dynamic micro-TAS devices. *Biomedical microdevices*, 9(4):513–22, August 2007. ISSN 1387-2176. doi: 10.1007/s10544-007-9059-1. URL http://www.ncbi.nlm.nih.gov/pubmed/17516175.

[38] C Lin, C Chao, and C Lan. Low azeotropic solvent for bonding of PMMA microfluidic devices. *Sensors and Actuators B: Chemical*, 121(2):698–705, February 2007. ISSN 09254005. doi: 10.1016/j.snb.2006.04.086. URL http://linkinghub.elsevier.com/retrieve/pii/S0925400506002462.

[39] Ryan T Kelly, Tao Pan, and Adam T Woolley. Phase-changing sacrificial materials for solvent bonding of high-performance polymeric capillary electrophoresis microchips. *Analytical chemistry*, 77(11):3536–41, June 2005. ISSN 0003-2700. doi: 10.1021/ac0501083. URL http://www.ncbi.nlm.nih.gov/pubmed/15924386.

[40] Y H Chen, W C Wang, K C Young, T T Chang, and S H Chen. Plastic microchip electrophoresis for analysis of PCR products of hepatitis C virus. *Clinical chemistry*, 45(11):1938–43, November 1999. ISSN 0009-9147. URL http://www.ncbi.nlm.nih.gov/pubmed/10545063.

[41] Koichi Ono, Shohei Kaneda, and Teruo Fujii. Single-step CE for miniaturized and easy-to-use system. *Electrophoresis*, 34(6):903–10, March 2013. ISSN 1522-2683. doi: 10.1002/elps.201200365. URL http://www.ncbi.nlm.nih.gov/pubmed/23307534.

[42] Victor M Ugaz, René D Elms, Roger C Lo, Faisal a Shaikh, and Mark a Burns. Microfabricated electrophoresis systems for DNA sequencing and genotyping applications: current technology and future directions. *Philosophical transactions. Series A, Mathematical, physical, and engineering sciences*, 362(1818):1105–29, May 2004. ISSN 1364-503X. doi: 10.1098/rsta.2003.1365. URL http://www.ncbi.nlm.nih.gov/pubmed/15306487.

[43] Joshua C Sanders, Michael C Breadmore, Yien C Kwok, Katie M Horsman, and James P Landers. Hydroxypropyl cellulose as an adsorptive coating sieving matrix for DNA separations: artificial neural network optimization for microchip analysis. *Analytical chemistry*, 75(4):986–94, February 2003. ISSN 0003-2700. URL http://www.ncbi.nlm.nih.gov/pubmed/12622396.

[44] J W Hong, K Hosokawa, T Fujii, M Seki, and I Endo. Microfabricated polymer chip for capillary gel electrophoresis. *Biotechnology progress*, 17(5):958–62, 2001. ISSN 8756-7938. doi: 10.1021/bp010075m. URL http://www.ncbi.nlm.nih.gov/pubmed/11587590.

[45] Victor M Ugaz, Rongsheng Lin, Nimisha Srivastava, David T Burke, and Mark a Burns. A versatile microfabricated platform for electrophoresis of double- and single-stranded DNA. *Electrophoresis*, 24(1-2):151–7, January 2003. ISSN 0173-0835. doi: 10.1002/elps.200390007. URL http://www.ncbi.nlm.nih.gov/pubmed/12652585.

[46] Dong S Zhao, Binayak Roy, Matthew T McCormick, Werner G Kuhr, and Sara a Brazill. Rapid fabrication of a poly(dimethylsiloxane) microfluidic capillary gel electrophoresis system utilizing high precision machining. *Lab on a chip*, 3(2):93–9, May 2003. ISSN 1473-0197. doi: 10.1039/b300577a. URL http://www.ncbi.nlm.nih.gov/pubmed/15100789.

[47] Kwang W Oh and Chong H Ahn. A review of microvalves. *Journal of Micromechanics and Microengineering*, 16(5):R13–R39, May 2006. ISSN 0960-1317. doi: 10.1088/0960-1317/16/5/R01. URL http://stacks.iop.org/0960-1317/16/i=5/a=R01?key=crossref.c5cf9020613ed3137ffb01175e1871b7.

[48] Anthony K. Au, Hoyin Lai, Ben R. Utela, and Albert Folch. Microvalves and Micropumps for BioMEMS. *Micromachines*, 2(4):179–220, May 2011. ISSN 2072-666X. doi: 10.3390/mi2020179. URL http://www.mdpi.com/2072-666X/2/2/179/.

[49] Eric T Lagally, Peter C Simpson, and Richard a Mathies. Monolithic integrated microfluidic DNA amplification and capillary electrophoresis analysis system. *Sensors and Actuators B: Chemical*, 63(3):138–146, May 2000. ISSN 09254005. doi: 10.1016/S0925-4005(00)00350-6. URL http://linkinghub.elsevier.com/retrieve/pii/S0925400500003506.

[50] M. A. Unger. Monolithic Microfabricated Valves and Pumps by Multilayer Soft Lithography. *Science*, 288(5463):113–116, April 2000. ISSN 00368075. doi: 10.1126/science.288.5463.113. URL http://www.sciencemag.org/cgi/doi/10.1126/science.288.5463.113.

[51] Shanshi Huang, Qiaohong He, Xianqiao Hu, and Hengwu Chen. Fabrication of micro pneumatic valves with double-layer elastic poly(dimethylsiloxane) membranes in rigid poly(methyl methacrylate) microfluidic chips. *Journal of Micromechanics and Microengineering*, 22(8):085008, August 2012. ISSN 0960-1317. doi:

10.1088/0960-1317/22/8/085008. URL http://stacks.iop.org/0960-1317/22/i=8/a=085008?key=crossref.f1344436e283163ff7d5277989d9c977.

[52] Govind V Kaigala, Viet N Hoang, and Christopher J Backhouse. Electrically controlled microvalves to integrate microchip polymerase chain reaction and capillary electrophoresis. *Lab on a chip*, 8(7):1071–8, July 2008. ISSN 1473-0197. doi: 10.1039/b802853b. URL http://www.ncbi.nlm.nih.gov/pubmed/18584081.

[53] M I Mohammed, E Abraham, and M P Y Desmulliez. Rapid laser prototyping of valves for microfluidic autonomous systems. *Journal of Micromechanics and Microengineering*, 23(3):035034, March 2013. ISSN 0960-1317. doi: 10.1088/0960-1317/23/3/035034. URL http://stacks.iop.org/0960-1317/23/i=3/a=035034?key=crossref.aaeb52a600bb1c4b12a97d405cd1e4d9.

[54] Jenny A Lounsbury, Anne Karlsson, Daniel C Miranian, Stephen M Cronk, Daniel A Nelson, Jingyi Li, Doris M Haverstick, Paul Kinnon, David J Saul, and James P Landers. From sample to PCR product in under 45 minutes: a polymeric integrated microdevice for clinical and forensic DNA analysis. *Lab on a chip*, 13(7):1384–93, April 2013. ISSN 1473-0189. doi: 10.1039/c3lc41326h. URL http://www.ncbi.nlm.nih.gov/pubmed/23389252.

[55] G. V. Kaigala, M. Behnam, A. C. E. Bidulock, C. Bargen, R. W. Johnstone, D. G. Elliott, and C. J. Backhouse. A scalable and modular lab-on-a-chip genetic analysis instrument. *The Analyst*, 135(7):1606–17, July 2010. ISSN 1364-5528. doi: 10.1039/b925111a. URL http://www.ncbi.nlm.nih.gov/pubmed/20369214.

[56] A Blake. *Practical Stress Analysis in Engineering Design, Second Edition,*. Dekker Mechanical Engineering. Taylor & Francis, 1989. ISBN 9780824781521. URL http://books.google.ca/books?id=uCkALMht9kkC.

[57] P. G. Lowe. *Basic Principles of Plate Theory*. Springer Netherlands, Dordrecht, 1982. ISBN 978-0-9033-8425-4. doi: 10.1007/978-94-011-6384-2. URL http://link.springer.com/book/10.1007/978-94-011-6384-2http://link.springer.com/10.1007/978-94-011-6384-2.

[58] Christopher Hall. *Polymer materials: an introduction for technologists and scientists*. A Halsted Press Book. John Wiley & Sons, Incorporated, 1989. ISBN 9780470210925. URL http://books.google.ca/books?id=PaAQAQAAMAAJ.

[59] George Wypych. {PP} polypropylene. In George Wypych, editor, *Handbook of Polymers*, pages 479–486. Elsevier, Oxford, 2012. ISBN 978-1-895198-47-8. doi: http://

dx.doi.org/10.1016/B978-1-895198-47-8.50144-2. URL http://www.sciencedirect.com/science/article/pii/B9781895198478501442.

[60] Tim Footz, Martin J Somerville, Robert Tomaszewski, Basil Elyas, and Christopher J Backhouse. Integration of combined heteroduplex/restriction fragment length polymorphism analysis on an electrophoresis microchip for the detection of hereditary haemochromatosis. *The Analyst*, 129(1):25–31, January 2004. ISSN 0003-2654. doi: 10.1039/b309931h. URL http://www.ncbi.nlm.nih.gov/pubmed/14737579.

[61] Jenny A. Lounsbury and James P. Landers. Ultrafast amplification of DNA on plastic microdevices for forensic short tandem repeat analysis. *Journal of forensic sciences*, 58(4):866–74, July 2013. ISSN 1556-4029. doi: 10.1111/1556-4029.12162. URL http://www.ncbi.nlm.nih.gov/pubmed/23692541.

[62] J. Martinez-Quijada, S. Caverhill-Godkewitsch, M. Reynolds, L. Gutierrez-Rivera, R.W. Johnstone, D.G. Elliott, D. Sameoto, and C.J. Backhouse. Fabrication and characterization of aluminum thin film heaters and temperature sensors on a photopolymer for lab-on-chip systems. *Sensors and Actuators A: Physical*, 193(2013): 170–181, April 2013. ISSN 09244247. doi: 10.1016/j.sna.2013.01.035. URL http://linkinghub.elsevier.com/retrieve/pii/S0924424713000484.

[63] H. Saha and C. Chaudhuri. Complementary Metal Oxide Semiconductors Microelectromechanical Systems Integration. *Defence Science Journal*, 59(6):557–567, November 2009. ISSN 0011748X. doi: 10.14429/dsj.59.1560. URL http://publications.drdo.gov.in/ojs/index.php/dsj/article/view/1560.

[64] M Khorasani, M Behnam, L van den Berg, C J Backhouse, and D G Elliott. High-Voltage CMOS Controller for Microfluidics. *IEEE transactions on biomedical circuits and systems*, 3(2):89–96, April 2009. ISSN 1932-4545. doi: 10.1109/TBCAS.2009.2012868. URL http://www.ncbi.nlm.nih.gov/pubmed/23853200.

[65] M Behnam, G V Kaigala, M Khorasani, S Martel, D G Elliott, and C J Backhouse. Integrated circuit-based instrumentation for microchip capillary electrophoresis. *IET nanobiotechnology / IET*, 4(3):91–101, September 2010. ISSN 1751-8741. doi: 10.1049/iet-nbt.2009.0018. URL http://www.ncbi.nlm.nih.gov/pubmed/20726675.

[66] Matthew Reynolds, Anastasia Elias, Duncan G Elliott, Christopher Backhouse, and Dan Sameoto. Variation of thermal and mechanical properties of KMPR due to processing parameters. *Journal of Micromechanics and Microengineering*, 22(12):125023, December 2012. ISSN 0960-1317. doi: 10.1088/0960-1317/

22/12/125023. URL http://stacks.iop.org/0960-1317/22/i=12/a=125023?key=crossref.638e389c5f7ab9a21172c3037650f45c.

[67] J Martinez-Quijada. Bio-mechanically driven MEMS power generator for implantable medical devices. *Masters Abstracts International*, 2007. URL http://scholar.google.com/scholar?hl=en&btnG=Search&q=intitle:Bio-mechanically+driven+mems+power+generator+for+implantable+medical+devices#0http://scholar.google.com/scholar?hl=en&btnG=Search&q=intitle:Bio-mechanically+driven+MEMS+power+generator+for+implantable+medical+devices#0.

[68] A Bejan. *Heat transfer*. John Wiley & Sons, Inc., 1993. ISBN 9780471502906. URL http://books.google.ca/books?id=TgtRAAAAMAAJ.

[69] M Kaviany. *Principles of Heat Transfer*. Wiley-Interscience publication. Wiley, 2002. ISBN 9780471434634. URL http://books.google.ca/books?id=dKI4k-9jK88C.

[70] David Ross, Micheal Gaitan, and Laurie E. Locascio. Temperature measurement in microfluidic systems using a temperature-dependent fluorescent dye. *Analytical chemistry*, 73(17):4117–23, September 2001. ISSN 0003-2700. URL http://www.ncbi.nlm.nih.gov/pubmed/11569800.

[71] Michael D. Abràmoff, Paulo J. Magalhaes, and Sunanda J. Ram. Image processing with ImageJ. *Biophotonics International*, 11(7):36–42, 2004. URL http://webeye.ophth.uiowa.edu/dept/biograph/abramoff/imagej.pdf.

[72] Rubin Battino, Timothy R. Rettich, and Toshihiro Tominaga. The Solubility of Nitrogen and Air in Liquids. *Journal of Physical and Chemical Reference Data*, 13(2):563, 1984. ISSN 00472689. doi: 10.1063/1.555713. URL http://scitation.aip.org/content/aip/journal/jpcrd/13/2/10.1063/1.555713.

[73] A. Getling. Rayleigh-Benard convection. *Scholarpedia*, 7(7):7702, 2012. ISSN 1941-6016. doi: 10.4249/scholarpedia.7702. URL http://www.scholarpedia.org/article/Rayleigh-B\unhbox\voidb@x\bgroup\let\unhbox\voidb@x\setbox\@tempboxa\hbox{e\global\mathchardef\accent@spacefactor\spacefactor}\accent19e\egroup\spacefactor\accent@spacefactornard_convection.